University of Stavanger

FACULTY OF SCIENCE AND TECHNOLOGY

MASTER'S THESIS

Study programme/specialization : Engineering Structures and Materials with Specialization in Mechanical Engineering	Spring semester, 2021. Open

Author : Ankit Sahu

Faculty Supervisor : Prof. Vidar Folke Hansen (UIS)

External Supervisor : Dr. Karl Gunnar Solheim (Subsea 7, Norway)

Title of master's thesis : Strain Induced Phase Transformation In Austenitic Stainless Steel (316L)

Credits (ECTS) : 30

Keywords : Martensite, Austenite, Stainless steel, Microstructure, Transformation.	Number of pages: ……72…… + supplemental material/other: …15… Stavanger, …15/06/21…….. date/year

Master Thesis

Strain Induced Phase Transformation in Austenitic Stainless Steel (316L)

By

Ankit Sahu

Faculty of Science and Technology
Department of Mechanical and Structural Engineering
and Materials science, University of Stavanger, Norway

Stavanger, June 2021

Master thesis
Strain induced phase transformation
in austenitic stainless steel (316L)

Distributed by :
Department of Mechanical and
Structural Engineering and Materials science
University of Stavanger (UIS), Norway.
https://www.uis.no/nb

Submission date : 15th June, 2021
Faculty Supervisor : Prof. Vidar Folke Hansen (UIS)
External Supervisor : Dr. Karl Gunnar Solheim (Subsea 7, Norway)

This document was prepared using LaTeX

"The finest steel has to go through the hottest fire"

- ***Richard Milhous Nixon***

Abstract

The purpose of the thesis is to investigate the amount of deformation induced martensite in AISI 316L austenitic stainless steel. Deformation condition used for this work are cyclic strain, tensile failure at room temperature with low (0.0005 per second) and high (200 per second) strain rates and tensile failure of material at depressed (-80°C, -40°C) and elevated temperature (100°C). Austenitic stainless steel (ASS) has the tendency to transform from metastable austenite phase to thermodynamically more stable α'-martensite due to plastic deformation. Thesis topic was proposed by Subsea7, Norway and their main area of interest was to see if any martensite is induced at lower strain amplitude under cyclic loading condition because during reeling pipeline operation pipes experiences a cyclic load of up to 2-3% strain amplitude. Apart from cyclically deformed specimen, this work also includes microstructure study of tensile failed specimens at various temperatures.

The material received for experimental work was a section of pipe which had a 3 mm ASS liner inside the pipe made up of carbon steel to prevent it from corrosion. The section of pipe was first cutted and then machined to form a dogbone like shape according to American society for testing and materials (ASTM) standard in order to carry out deformation using 250kN INSTRON uniaxial tensile test machine. After the deformation of material at particular test condition it was examined using various microscopy techniques. First microstructure investigation was done using optical microscope (OM) and further it was analyzed using Transmission electron microscope (TEM). Vickers hardness measurement was also carried for all the deformed specimens. X-ray diffraction (XRD) technique was used to find out if any new phase was observed or not.

The microstructure analysis through optical microscope revealed that there was no martensite induced in cyclically deformed specimen (both at lower and higher strain amplitudes), but the number of mechanical twin's were increased with increasing strain amplitude. Also this finding was supported by TEM, XRD, hardness value and ferritescope analysis. On the other hand, the microstructure of tensile failed specimen revealed that the austenite grain boundary was not stable and their might be induced martensite formation as perceived from the image analysis using optical microscope. Due to limitation of lab facility at the university it was not possible to measure the magnetic parameters of tensile failed specimen which is an important area to be known for this work because austenite steel is non-magnetic in nature but the induced martensite is magnetic in nature. TEM diffraction pattern was investigated but it was difficult to get any diffraction pattern for martensite in tensile failed specimen which may be attributed to low amount of induced martensite and low examined area. The influence of applied stress and the stacking fault energy on the formation of shear bands, acts as the nucleation sites for induced martensite. It was seen that the strain-induced martensite transformation was suppressed with increasing strain rate and temperature in the tensile failed specimen, due to temperature dependence of the stacking fault energy. Under various temperature of examination it was seen that the maximum amount of induced martensite was found to occur at lower temperature (-80°C) and minimum at elevated temperature (100°C) for tensile failed specimen.

Keywords : Martensite, Austenite, Stainless steel, Microstructure, Transformation.

Acknowledgement

This thesis is submitted in partial fulfilment for Master of Science degree in Engineering Structures and Materials with specialization in Mechanical Engineering at University of Stavanger, Norway. The thesis work has been carried out at the department of Mechanical, Structural Engineering and Material Science, Faculty of Science and Technology, University of Stavanger, Norway and in collaboration with Subsea7, Norway. Starting from January 2021 to June 2021.

My deepest gratitude, heartiest appreciation and sincere thanks goes to my esteemed faculty supervisor Professor Vidar Folke Hansen for providing the opportunity to work under his supervision. I appreciate him for his constant support, guidance, time and motivation to carry out the work.

I would also like to express my sincere thanks to external supervisor Dr.Karl Gunnar Solheim from Subsea7 Norway, for proposing the topic and objectives to be achieved by this work. I would also like to thank him for his time and support at crucial stages of thesis and his valuable guidance. I would thank Subsea7, Norway for providing the material (austenitic stainless steel 316L pipe section) to carry out the experimental works. I would also thank Quality Lab AS, Stavanger for providing Ferritescope equipment.

My vote of thanks also goes to lab engineer Wakshum Mekonnen Tucho (for carrying out the TEM work), Emil Surnevik Kristiansen (helping me with machining of material and carrying out CNC work), Jørgen Grønsund (helping me with universal tensile testing machine), Johan Andreas (helping with optical microscope and material preparation lab) and Caroline Rudd (helping with XRD) without them it wouldn't be possible to complete my thesis on time.

I would also like to express my gratitude to my fellow classmates who provided me with their support whenever needed. Last but not least, my unlimited gratitude goes to my sisters and parents for their showers of blessings and continuous encouragement given to me throughout my study period in Norway.

Ankit Sahu
Stavanger, Norway

Contents

List of Figures

List of Tables

List of Abbreviations

AISI	The American Iron and Steel Institute
ASTM	American society for testing and materials
ASS	Austenitic stainless steel
BCT	Body-centered tetragonal
BCC	Body-centered cubic
BF	Bright field
CNC	Computer numerical control
DF	Dark field
EBSD	Electron backscattering diffraction
ECCI	Electron channeling contrast imaging
EDS	Energy dispersive spectroscopy
EBSP	Electronic backscatter pattern
FCC	Face-centered cubic
FS	Ferrite scope
HCP	Hexagonal-closed packed
MFM	Magnetic force microscope
NDT	Non destructive testing
ND	Neutron diffraction
OM	Optical microscope
OPS	Oxide polishing suspensions
PC	Plain carbon
SEM	Scanning electron microscope
SIM	Strain-induced martensite
SFE	Stacking fault energy
SAD	Selected area diffraction
SA	Strain amplitude
SR	Strain rate
TEM	Transmission electron microscope
XRD	X - ray diffraction

List of Symbols

M_s	Temperature at which thermal induced martensite can be seen [°C]
M_d	Temperature above which no strain-induced martensite is formed [°C]
M_{d30}	Temperature at which 50% α'-martensite is formed at 30% true tensile strain [°C]
M_s^{σ}	Temperature above which martensitic transformation can occur only due to plastic deformation [°C]
a, b, c	Lengths of unit cell
α', ε	Deformation induced martensite
γ	Austenitic phase
α, δ	Allotropes of iron bcc
σ_y	Yield stress of austenite
$\Delta G^{\gamma \rightarrow \alpha'}$	Chemical free-energy difference between austenite and α'- martensite phases [J/mol]
$\Delta G^{\gamma \rightarrow \alpha'}_{M_s}$	Chemical free-energy difference between austenite and α'- martensite phases at M_s temperature [J/mol]
$\Delta G^{\gamma \rightarrow \alpha'}_{T_1}$	Chemical free-energy difference between austenite and α'- martensite phases at T_1 temperature [J/mol]

1 Introduction

1.1 Background

Austenitic stainless steel (ASS) is the largest family of stainless steel, accounting up to two-third of all different forms of stainless steel produced globally. They have mainly austenitic microstructure and this microstructure is result of alloying the steel by elements such as nickel, manganese and nitrogen to maintain an austenitic microstructure at all temperatures ranging from the cryogenic region to the melting point. Since they possess the same microstructure at all temperatures they cannot be hardened by heat treatment but they can be strengthened by cold working, this is limited to thin sheets and small diameter bars. Due to austenitic microstructure, it has excellent formability, weldability and are essentially non-magnetic in nature and maintain their ductility even at cryogenic temperature. [1]

Austenitic stainless steel 316L mainly contains chromium-nickel alloys and is widely used in engineering application due to its corrosion resistance, good weldability and mechanical properties. Due to presence of molybdenum 316L shows greater corrosion resistance than steel alloyed with only chromium and nickel. This steel finds its application in food processing, pharmaceutical equipment, medical devices, in potable water, wastewater treatment and in marine applications. Due to its vast application in offshore field this steel is also called as *marine steel*.

1.2 Aim and Objective

This project will focus on how the microstructure of 316L austenitic steel is affected by the strain that is inflicted on the material during pipe installation by reeling for offshore application. During reeling operation pipeline undergoes a number of times reeling and unreeling and due to that cyclic strain is developed. It is important to know if there is any change in the microstructure due to reeling process of pipeline which can further influence the stainless liners resistance to corrosion and hydrogen assisted cracking. Which in turn can further lead to detoriation in mechanical properties of the material.

The main objective of thesis work is to investigate if any martensite is induced in 316L steel after deforming it cyclically at low strain amplitude and high strain amplitude. The work has also been extended to the failure of material at high and low strain rate values at room temperature and also at low (-80°C and -40°C) and high (100°C) temperatures. There is a tendency of martensite formation in austenitic stainless steel under specific deformation condition. The deformed specimen microstructure was examined using optical microscopy (OM), Transmission electron microscopy (TEM), X-ray diffraction (XRD) and hardness measurement. Figure 1.1 below shows the pipe being reeled off and straightened in the lay ramp on the aft of a Subsea7 vessel.

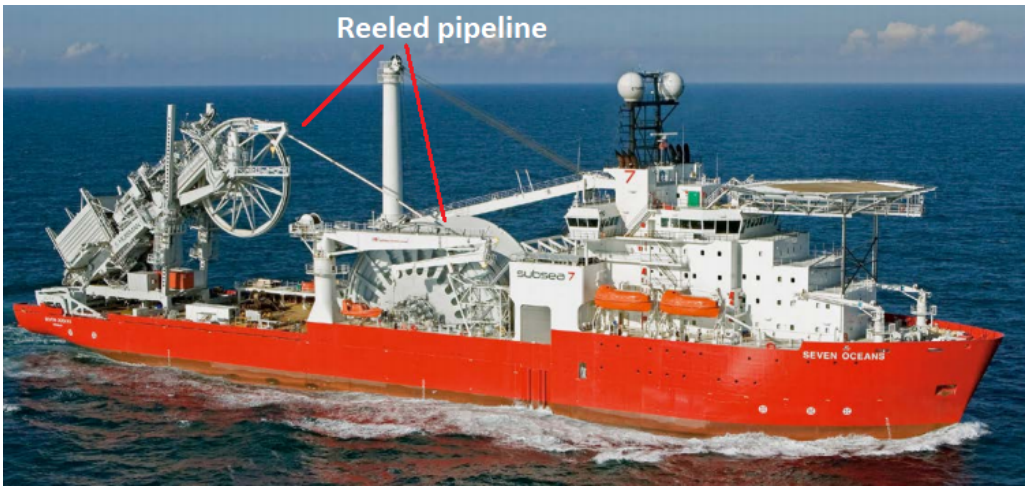

Figure 1.1: *Subsea7 vessel "Seven Oceans" during reeling pipeline installation.* [2]

1.3 Importance of The Research

Austenitic AISI 316L stainless steels are widely used as structural components in heavy industry facility due to their good corrosion resistance, weldability, and mechanical properties [3].These structural components are usually subjected to severe cyclic mechanical stress/strain during operation and hence due to its large application there is a growing interest in failure analysis of 316L austenitic steel. The 316L austenitic steel has a predominantly austenitic microstructure with fractions of delta ferrite. A feature of austenitic stainless steel is that the austenite may partially transform to martensite when the steel is subjected to plastic strain, this is commonly referred to as strain induced phase transformation. This is well known for lower alloyed austenitic stainless steel such as AISI 304 austenitic steel but has also been shown to happen in 316L austenitic steel. If martensite is present in austenitic stainless steel, it may be prone to cracking mechanisms relating to hydrogen, such as sulphide (H_2S) stress cracking. The formed martensite will also affect mechanical properties. Because of this it is important to know how much martensite is present in the material after it has subjected to desired strain condition.

1.4 Challenges and Problems Faced

One of the main challenges encountered during this thesis was to make the test specimen from the material received. Since the material received was a section of pipe (see Fig. 3.1) with a diameter of 273.10 mm and thickness of 18.90 (15.90+3.00) mm of which 3 mm was the inner liners of austenitic stainless steel 316L and rest of the pipe material was of carbon steel. A lot of machining hours (see Table 3.2) were used to make a dogbone shape like structure according to ASTM standard.

Another major problem was related to Scanning electron microscope (SEM). SEM got damaged during beginning of thesis and was not repaired until the end time. So, SEM

examination was not performed for this work. Also, XRD machine was out of use for some duration due to some technical problems in it which delayed some part of work. Also, COVID restrictions were followed in the laboratory and we need to book the lab in advance in order to use it.

1.5 Thesis Organization

Chapter 1: **(Introduction)** This chapter briefly summarizes the background and objectives of the thesis. It also emphasizes the importance of research and challenges faced during thesis.

Chapter 2: **(Literature review and theory)** This chapter deals with the theoretical part related to austenitic steel and martensite formation. It goes in details on the parameters which influence the formation of martensite and stainless-steel properties, for example influence of alloying elements, temperatures, chemical composition etc.

Chapter 3: **(Experimental methodology)** This chapter deals with the experimental methodology adopted for this thesis. It briefly explains the processes used for specimen preparation for various methods of examination for example specimen preparation for straining, Optical microscope, TEM and X-ray diffraction. It also goes into the details of various experimental procedure carried out.

Chapter 4: **(Results)** In this chapter author have discussed the results obtained from experimental work carried out. It also briefly explains the reason behind the findings.

Chapter 5: **(Discussion)** In this section a brief discussion about the overall findings is discussed and links the results with the work done by other people.

Chapter 6: **(Conclusion)** In this chapter author concludes the work performed by stating the major findings and results.

Chapter 7: **(Further work)** In this chapter author discusses some possible future work to be carry out to verify the findings more precisely and other approach to the problem.

2 Theory and Literature Review

Different published articles, journals and books were studied to research the thesis topic and experimental works needed to be carried out. This section in general explains the theory behind the austenitic stainless steel, for example microstructure, martensite transformation and austenitic stability. Below subsection will discuss related theories in more detail.

2.1 Austenitic Stainless Steel

Austenitic stainless steels (ASS) are the largest category in the stainless-steel family in terms of tonnage produced yearly. These steels can be made soft enough such that it can be formed easily using the same instrument which can be used for carbon steel (i.e. with a yield strength of about 200 MPa), but they can also be made extremely hard by cold working process, up to a yield strength of over 2000 MPa. Down to absolute zero their austenitic (fcc, face-centered cubic) structure is very tough and ductile and at increased temperatures, they do not lose their strength as easily as ferritic (bcc, body-centered cubic) iron base alloys [4]. When selecting an austenitic steel, the basic and fundamental criteria is usually that it should withstand with virtually no corrosion under the condition in which it is going to be used. Table 2.1 below summarizes the general chemical composition of 300 series and some 200 series ASS. Those in the AISI 300 series, Cr-Ni acts as the main alloying elements and are most commonly used. It is possible to consider the grade containing around 18wt%Cr and 8wt%Ni (often called 18-8 steel) as the foundation for this series. Because of high price of nickel, as a replacement usage of nitrogen and manganese is very common nowadays [5]. The 200 series essentially contain Cr-Mn alloys.

Table 2.1: *The composition of steels in the AISI 300 series and some 200 series.* [6]

Steel	Cr	Ni	Mo	Mn	N	C	Si	P	S	Ti
201	16-18	3.5-5.5	-	5.5-7.5	0.25max	0.15	1.00	0.045	0.015	-
201L	16-17	3.5-5.5	-	6-8	0.20max	0.030	1.00	0.045	0.015	-
202	17-19	4-6	-	7.5-10	0.25max	0.15	1.00	0.045	0.015	-
204C	16-18	2	1.00	6.5-8.5	0.30max	0.10	2.00	0.040	0.030	-
301	16-18	6-8	-	2.00max	0.1max	0.15max	1.00max	0.045max	0.03max	-
302	17-19	8-10	-	2.00max	0.1max	0.15max	0.75max	0.045max	0.03max	-
304	17.5-19.5	8-10.5	-	2.00max	0.10max	0.07max	0.75max	0.045max	0.03max	-
304L	17.5-19.5	8-12	-	2.00max	0.10max	0.03max	0.75max	0.045max	0.03max	-
309	22-24	12-15	-	2.00max	-	0.02	0.75max	0.045max	0.03max	-
309S	22-24	12-15	-	2.00max	-	0.08	0.75max	0.045max	0.03max	-
316	16-18	10-14	2-3	2.00max	0.1max	0.08max	0.75max	0.045max	0.03max	-
316L	16-18	10-14	2-3	2.00max	0.1max	0.03max	0.75max	0.045max	0.03max	-
316LN	16-18	10-14	2-3	2.00max	0.1-0.16	0.03max	0.75max	0.045max	0.03max	-
316Ti	16-18	10-14	2-3	2.00max	0.1max	0.08max	0.75max	0.045max	0.03max	5(C+N) min-0.70max

Austenitic grades are the most widely used stainless grades, primarily because they give very predictable levels of corrosion resistance with excellent mechanical properties in many instances. Using them wisely will save considerable costs for the design engineer in his or her product. They are very easy to use metal alloy with a lower life - cycle cost for fully developed products as compared to many others. The austenitic alloys can have composition anywhere in the portion of the Schaeffler - Delong diagram which is labeled as austenitic in Figure 2.1 [7].

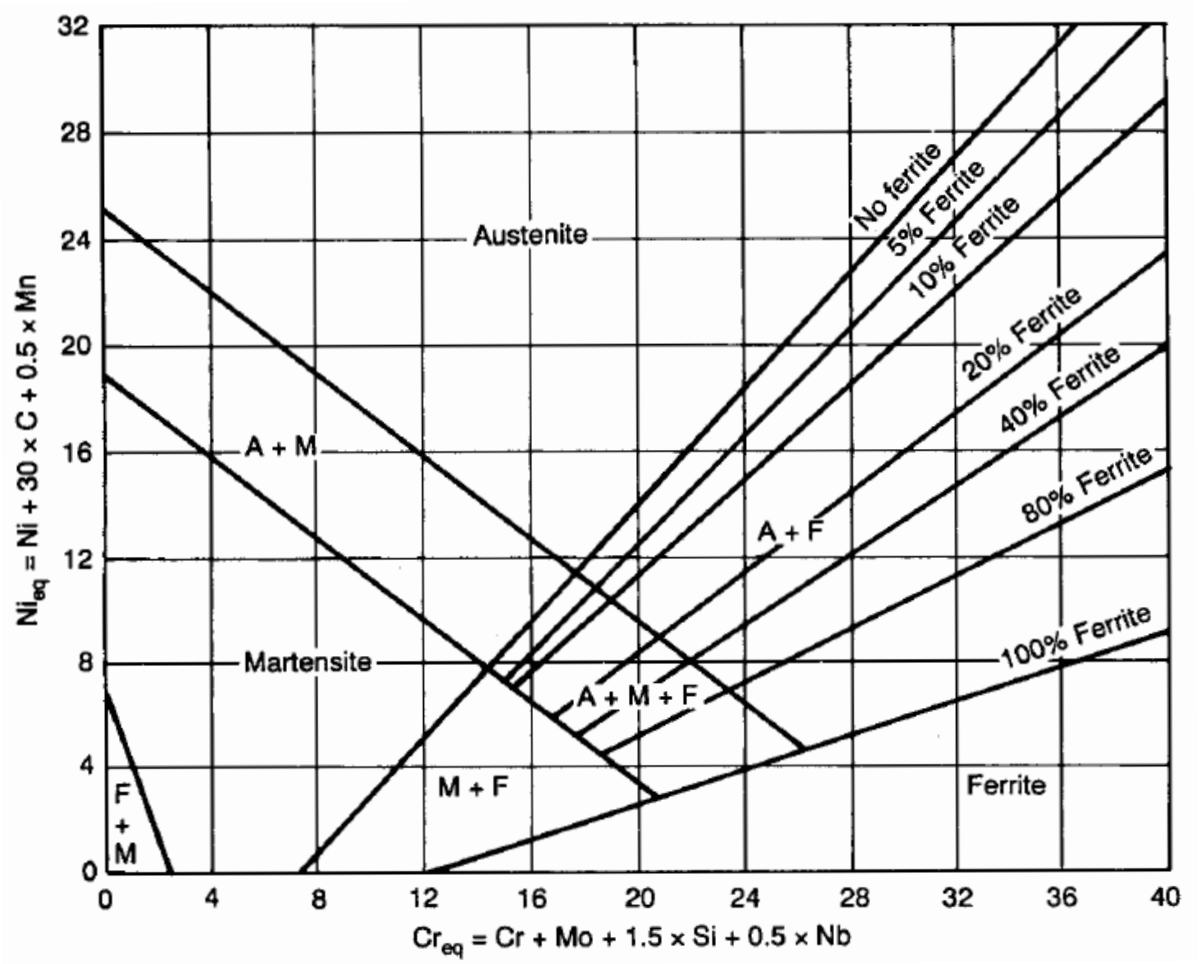

Figure 2.1: *Schaeffler-Delong stainless steels constitution diagram.* [7]

The motive of this diagram is to show which phases are present in alloys in the as-solidified condition, such as found in welds. Therefore, this diagram can also be referred to castings and continuously cast products. Taking the practical fact of castability, the composition of most commercial alloys falls along the zone which contains several percent of ferrite as cast. The key characteristic of austenitic alloys is that, when chromium and molybdenum are increased to enhance specific properties such as corrosion resistance, we must add nickel and other austenitic stabilizers to preserve the austenitic structure [8].

2.2 The Iron-Chromium-Nickel System

In order to better understand the properties of iron based stainless steel and associated phenomena that take place a proper understanding of Iron-Chromium-Nickel system is of utmost importance. Figure 2.2 below shows a binary iron-chromium equilibrium diagram. This are equilibrium diagram i.e. they represent a system of very slow heating or cooling.

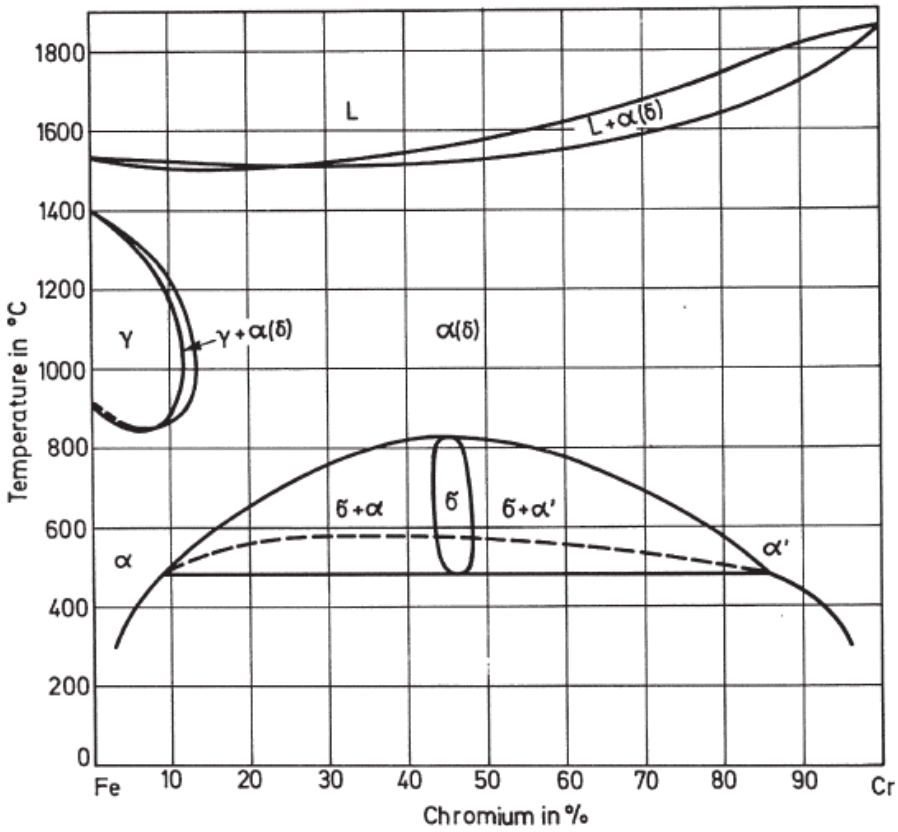

Figure 2.2: *The Fe-Cr equilibrium diagram* [9].

According to the above diagram (Fig.2.2) chromium restricts the occurrence of the austenite - γ loop to the point that above 13wt% Cr the binary alloys are ferrite over the complete temperature range, whereas there is a narrow $(\alpha + \gamma)$ range between 12 and 13 wt% Cr [8]. The ferrite is normally referred to as delta ferrite, because in these steels the phase has continuous existence from melting point to room temperature. This means that alloys with more than about 13% chromium do not show any $\gamma \rightarrow \alpha$ transformation, thus ruling out any further grain refinement and the possibility of steel hardening [9]. Ferrite formation is strongly promoted by chromium to the extent where only ferrite crystals (δ, α) are precipitated from the the melt over the full alloying range. With increased chromium contents about 820°C, the brittle sigma phase starts to precipitate from δ ferrite. It consists of approx. 45% Cr and represents a metallic compound of iron and chromium. Due to high chromium content, embrittlement will occur which may be accompanied by a chromium depletion of the matrix at the grain boundaries of the precipitated sigma phase and which can have a detrimental effect on corrosion resistance [9].

The addition of carbon to binary system expands the γ loop towards a higher chromium content (see in Figure 2.3) and also widens the $(\alpha + \gamma)$ phase field up to 0.3% C [8]. When

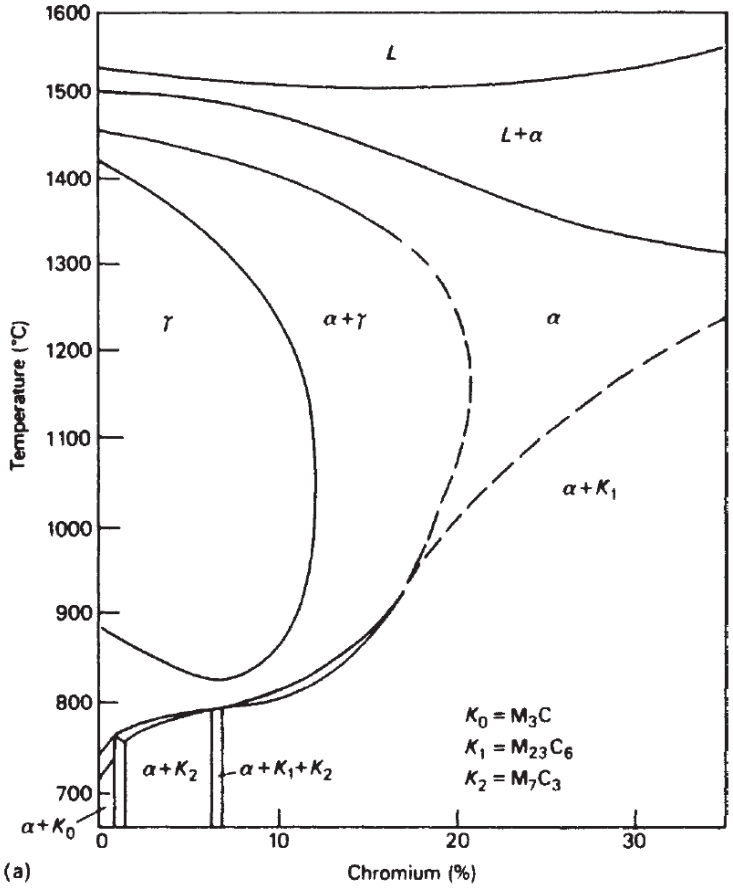

Figure 2.3: *Effect of carbon on the Fe-Cr diagram, 0.05wt% C.* [10]

carbon is steadily added to an 18wt% Cr steel, in the range up to about 0.04wt% C, the steel is fully ferritic (Figure 2.3) and cannot be transformed. Between 0.08% and 0.22% C, partial transformation is possible leading to $(\alpha + \gamma)$ structures, while above 0.40wt% C the steel can be made fully austenitic (Figure 2.4) if cooled rapidly from the γ-loop region. The Another effect of carbon in this binary system is to introduce carbides to the structure as shown in Figure 2.4:

$$K_o = M_3C, \qquad K_1 = M_{23}C_6, \qquad K_2 = M_7C_3 \tag{2.1}$$

where 'M' represents a mixture of metal atoms. $M_{23}C_6$ is the most significant carbide formed in austenitic steels and can have a substantial influence on corrosion resistance [8].

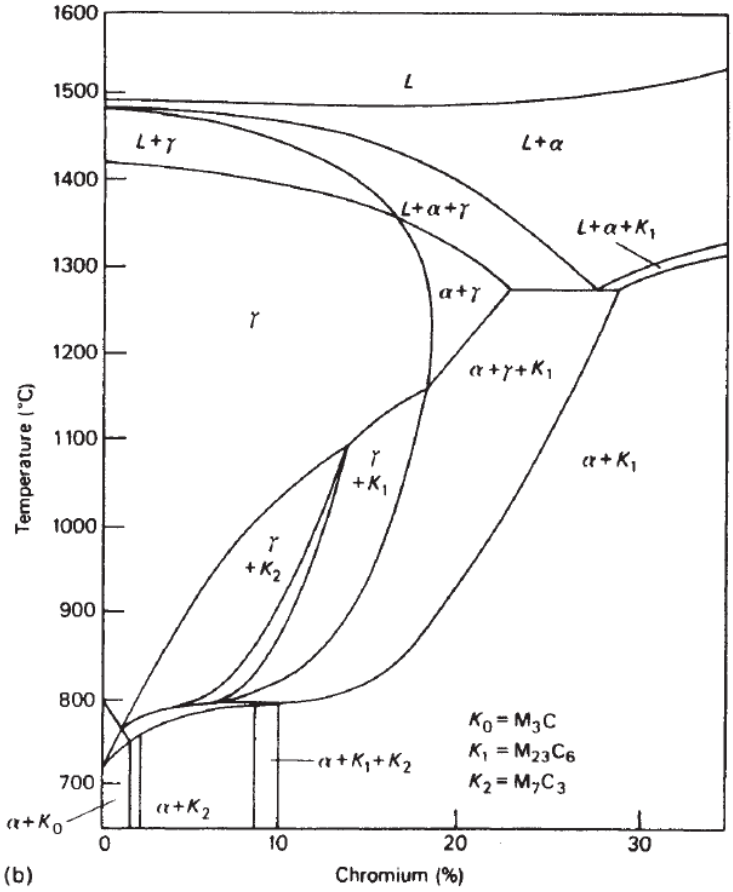

Figure 2.4: *Effect of carbon on the Fe-Cr diagram, 0.4wt% C.* [10]

If nickel is added to a low carbon iron 18wt.% Cr alloy, the γ-phase field is expanded until at about 8wt% Ni the γ-phase persists to room temperature (Figure 2.5) leading to the familiar group of austenitic steels based on 18Cr-8Ni wt%. This particular composition arises because a minimum nickel content is required to retain γ at room temperature. With both lower and higher Cr contents more nickel is needed. For example, higher Cr steels which have more corrosion resistance e.g. for 25wt% Cr about 15wt% nickel is needed to retain the austenite at room temperature. Incomplete retention of austenite is result of martensite formation. When M_s is lower than room temperature than it can be defined as stable austenite. The 18Cr-8Ni steel, in fact, has an M_s just below room temperature and hence on cooling (for example: in liquid or air) will transform very substantially to martensite [8].

As you can also see in Figure 2.5 the carbide phase $M_{23}C_6$ exists below about 900°C. However, when the steel is heated around 1100-1150°C it goes into the solution and on quenching we obtain a precipitate-free austenite. However, we can observe a re-precipitate of $M_{23}C_6$ at the grain boundaries when steel is heated in the range of 550-750°C [8].

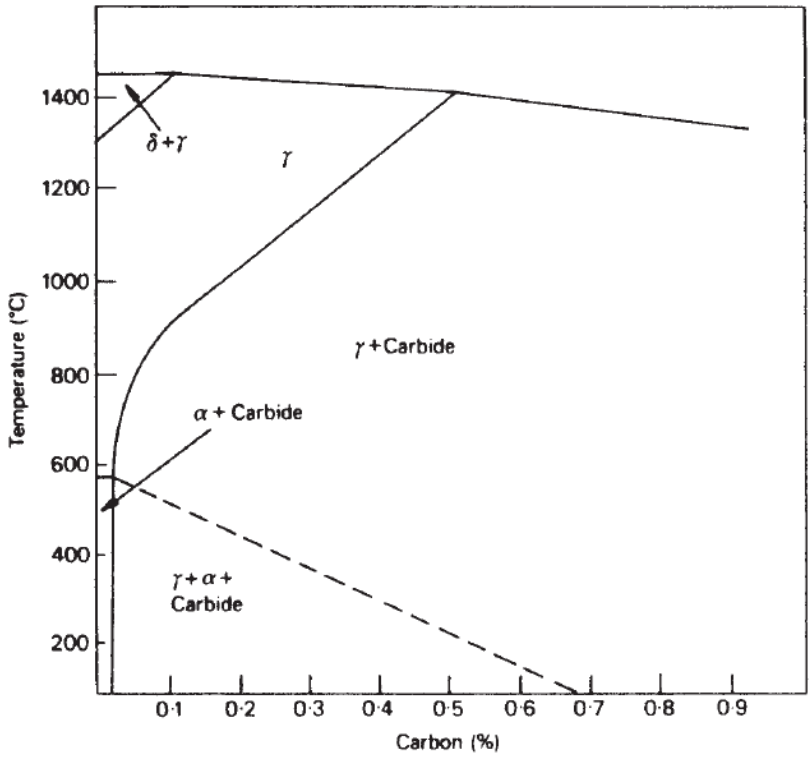

Figure 2.5: *Effect of carbon on the phase diagram for an 18Cr-8Ni.* [10]

Instead of nickle we can use manganese because it also expands the γ-loop. However, manganese is not as effective as nickle and the effective is around half of nickel, hence higher concentration must be used. If there is no concentration of chromium, then around 12wt% Mn is required to stabilize even higher carbon (1-1.2wt.%) austenite. If carbon content is low typically Cr-Mn steels require 12-15% Cr and 12-15wt.% Mn to remain austenitic at room temperature.

The chromium equivalent has been empirically determined using the most common ferrite-forming elements [11].

Cr equivalent (wt%)

$$= \%Cr + 2.0\%Si + 1.5\%Mo + 5\%V + 5.5\%Al + 1.75\%Nb + 1.5\%Ti + 0.75\%W \tag{2.2}$$

While the nickel equivalent has likewise been determined with the familiar austenite-forming elements [11].

Ni equivalent (wt%)

$$= \%Ni + \%Co + 0.5\%Mn + 30\%C + 0.3\%Cu + 25\%N \tag{2.3}$$

2.3 Influence of other Elements on the Iron-Chromium-Nickel Diagram

2.3.1 Influence of Molybdenum

Besides chromium and nickel another important alloying elements in stainless steel is molybdenum. Addition of molybdenum is necessary because it reduces the general corrosion rate, improves resistance to localized corrosion at elevated temperatures and also reduces sulfide stress-corrosion cracking susceptibility. Therefore, steels used in oil and gas transportation often have molybdenum as one of the alloying elements [12]. Figure 2.6 shows the iron-molybdenum constitution diagram. Likewise, chromium, molybdenum also narrows the area of γ phase. This means, molybdenum also supports the formation of ferrite. In the case of chromium, it takes around 12-13% to produce a complete constriction (loop) of the pure γ range, in case of molybdenum 2.7% is suffice (See detail in Fig.2.6) [9].

Iron and molybdenum together form a inter-metallic phase. The most important one is the Laves phase Fe_2Mo with approx. 45% Mo [9], (Laves phases are inter-metallic phases with the general formula A_2B. The major criterion for their formation is the tendency towards interstitial packing in the crystal lattice which reaches a maximum at a ratio of atomic radii of B:A = 1.1225. Examples of Laves phases in stainless steels are (Fe_2Mo, Fe_2Mo, Fe_2Ti or Fe_2Nb).

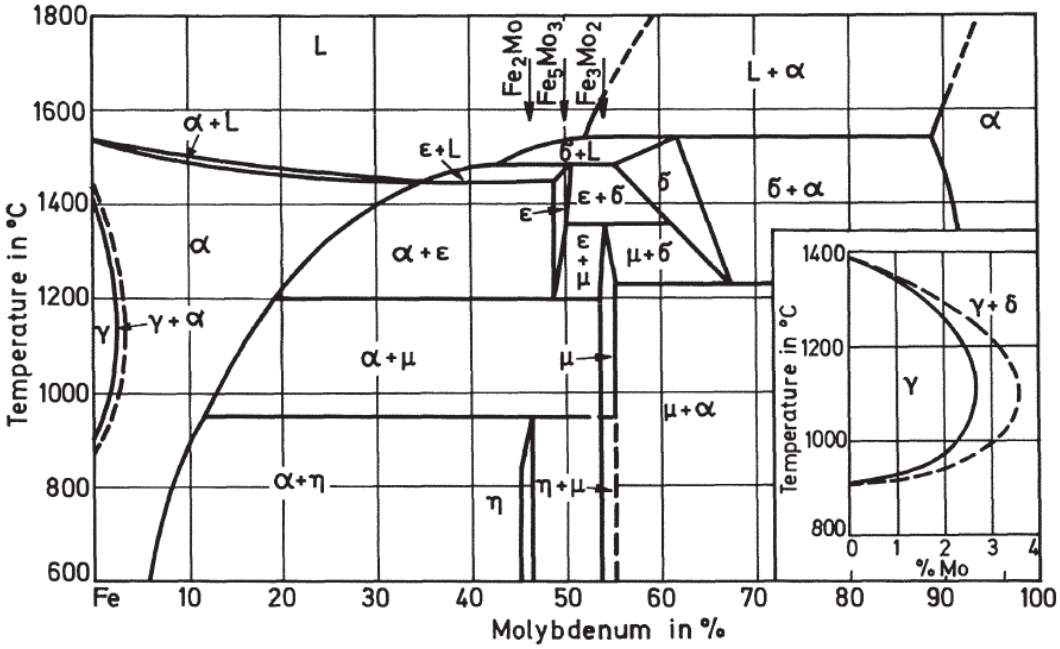

Figure 2.6: *Iron-molybdenum constitution diagram.* [13]

Molybdenum is a strong ferrite stabilizing element and hence this must be balanced by proper addition of austenite stabilizing elements such as carbon, nitrogen or nickel to have an austenitic microstructure in steel [12].

2.3.2 Influence of Nitrogen

Nitrogen is often undesirable element in low alloyed steels but in stainless steel it might act as an important alloying element. Nitrogen stabilizes austenite and has an equally strong influence on transition phenomena in the ternary iron-chromium-nickel diagram as carbon does [9]. Nitrogen has a much higher solubility in austenitic chromium-nickel stainless steel alloys as compared to carbon which results in a much lower susceptibility to form undesirable precipitations in austenitic steel grades [9].

Figure 2.7 shows the nitrogen solubility of liquid iron-chromium-nickel alloys at 1600 °C. A strong rise in solubility with increasing chromium contents is seen [14].

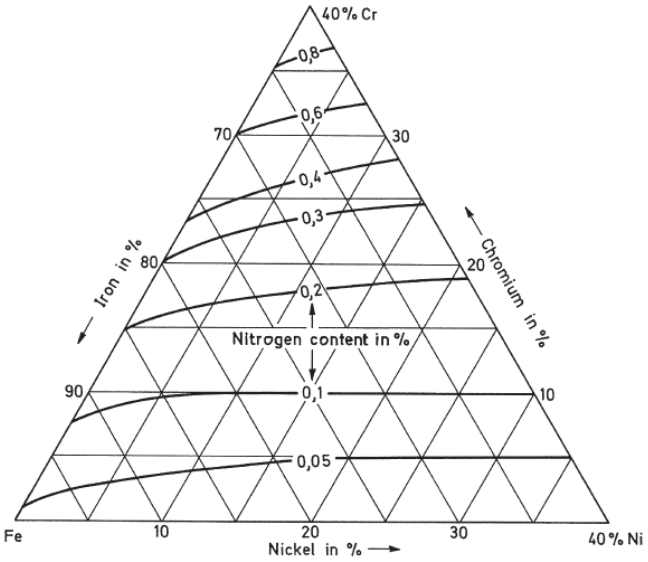

Figure 2.7: *Solubility of nitrogen in iron-chromium-nickel alloys at 1600°C.* [14]

Figure 2.8 shows the nitrogen solubility of austenitic Cr-Ni steels during solidification and the chance of porosity formed at various different composition of chromium at the time of solidification. The maximum nitrogen content for porosity-free solidification rises from 0.20% at 17% chromium to 0.50% at 25% chromium in linear proportion with the chromium content [9].

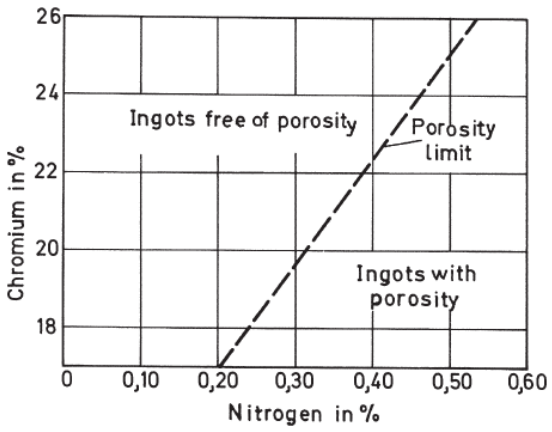

Figure 2.8: *Solubility of nitrogen in iron-chromium-nickel alloys at 1600°C.* [9]

2.3.3 Influence of Niobium

Niobium shows a strong affinity towards carbon. This effect is used, in particular, in stainless steels and welded metals to trap carbon in the form of niobium carbide in a stable manner, thus increasing the resistance to intergranular corrosion [9]. Figure 2.9 shows the iron-niobium constitution diagram [13]. Niobium severely constricts the area of γ phase (see detail in Fig. 2.9). Niobium forms a very stable carbides with carbon, represented by the formula NbC or Nb_4C_3. The affinity of niobium to carbon is so strong that before it even enters the matrix, niobium is preferentially bound to carbon [9].

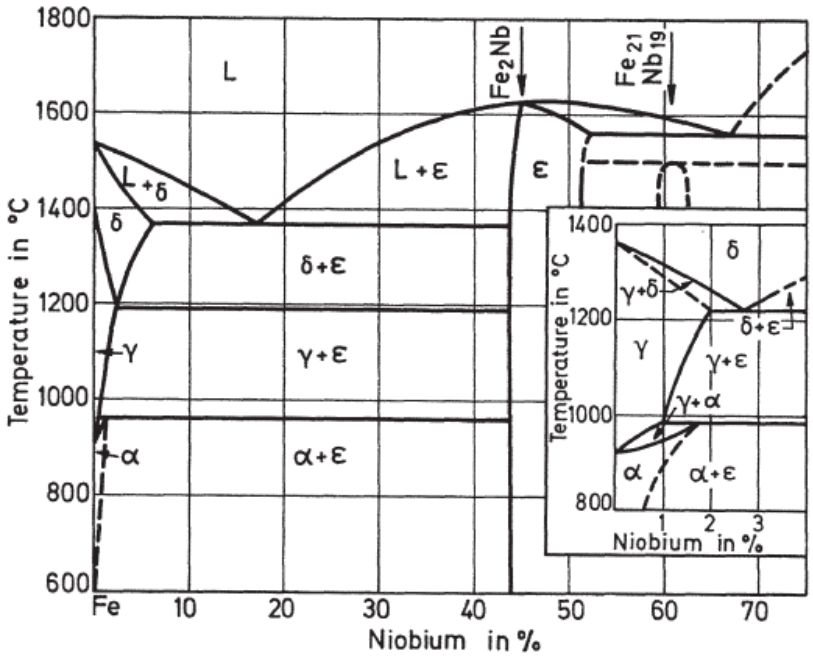

Figure 2.9: *Iron-niobium constitution diagram.* [13]

2.3.4 Influence of Titanium

Titanium also possesses a high affinity to carbon same as niobium and therefore is also used to arrest carbon by making a stable form of titanium carbide. Such steel grades are termed as " titanium stabilized " steels [9]. Same as niobium titanium also constricts the γ range in iron-chromium-nickel system. Figure 2.10 shows the iron-titanium constitution diagram. A eutectic is formed at 13.2% titanium and iron titanide is formed at approximately 30% titanium with formula Fe_2Ti [9].

Together with carbon, titanium forms a highly stable titanium carbide TiC. Titanium also shows high affinity to nitrogen and forms a nitride, TiN, and together with carbon forms a titanium carbo-nitride Ti(CN). The formation of these nitrides takes place parallel to the formation of titanium carbide. Together with nickel, titanium forms a compound with the formula Ni_3Ti with about 25% titanium, which is used for precipitation hardening purposes in the case of high nickel steels and nickel-base alloys [9].

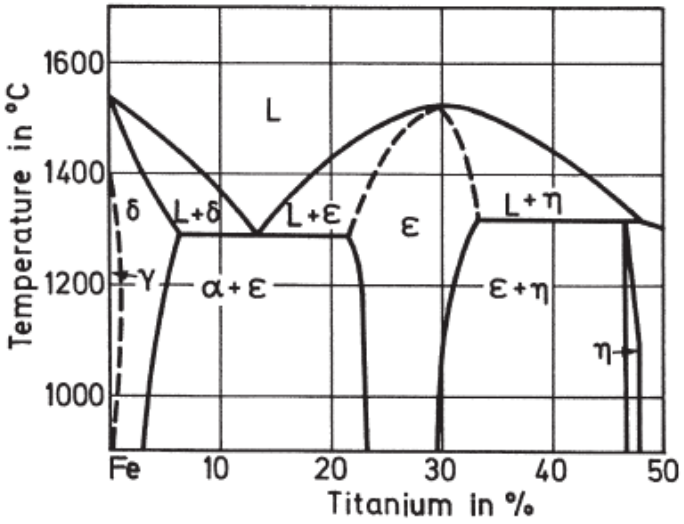

Figure 2.10: *Iron-titanium constitution diagram.* [13]

2.3.5 Influence of Silicon

Silicon has gained importance as an alloying element because it greatly improves the corrosion resistance of austenitic chromium-nickel steels to strong nitric acid [15]. In case of heat resistance stainless steel, silicon is used in contents of 1-3% to improve the scaling resistance [9]. Silicon severely constricts the range of γ phase and promotes the formation of δ ferrite to the detriment of austenite. Of much greater importance is the influence of silicon on the expansion of the sigma phase range. Figure 2.11 below summarizes the influence of silicon on the sigma phase in the binary iron-chromium system and influence of silicon in the ternary iron-chromium-nickel system seems to be similar to that in the binary iron-chromium system [9]. Silicon greatly expands the sigma phase range to a lower chromium content.

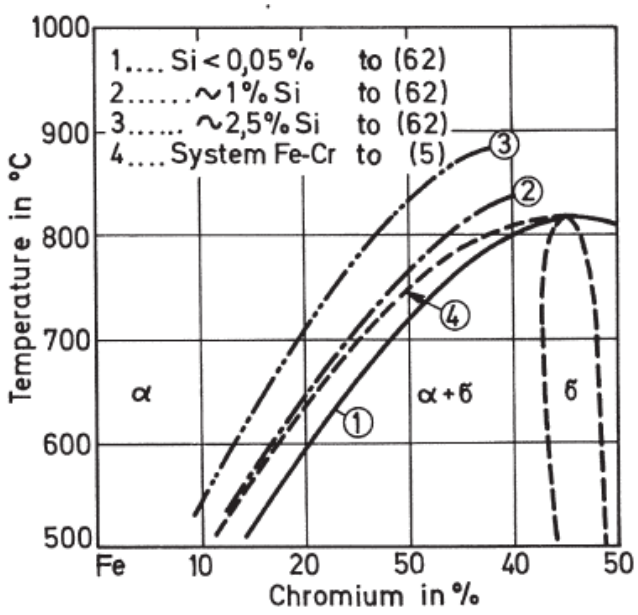

Figure 2.11: *Influence of silicon on the sigma phase range in the iron-chromium system.* [13]

2.3.6 Influence of Sulphur

Sulphur represents an undesirable impurity in stainless steels and stainless-steel weld metals which gives rise to hot cracking problems during welding due to the formation of low melting sulphides which may precipitate during solidification as liquid film between the grain boundaries of newly formed crystals [9]. Sulphur forms a low melting eutectic with iron and has a very poor solubility in γ iron. Considering the influence of Sulphur in iron-chromium-nickel system, the solubility of sulphur decreases with increase in nickel and chromium content and due to this the negative effect of Sulphur is reduced [16].

2.3.7 Influence of Phosphorus

Like Sulphur, phosphorus also forms low melting eutectics with the basic elements of stainless steels, i.e., iron, chromium and nickel. Contrary to Sulphur, however, both iron and nickel are capable of dissolving relatively large amounts of phosphorus [17]. Phosphorus has a severe constricting effect on the γ range in iron-chromium-nickel but the amount of phosphorus is so low that this effect can be neglected. phosphorus has a negative effect on hot cracking behavior in Austenitic stainless steel [9].

2.3.8 Influence of Copper

In order to improve corrosion resistance as well as increase the hardness and tensile strength through precipitation effects of this element, copper is added to stainless steels. Nickel and copper are completely soluble in each other. Chromium on the other hand shows practically no solubility for copper. copper shows an austenitizing effect in the ternary iron-chromium- nickel system but however this effect is weaker than that of nickel [9].

2.3.9 Influence of Boron

Boron is sometimes added in small amounts to stainless steels during melting for crystal refinement during solidification, in order to achieve better hot forming properties. In the ternary iron-chromium-nickel system, iron possess a low solubility for boron and it decreases with the addition of nickel and chromium [13].

2.3.10 Influence of Oxygen

Oxygen is an undesirable tramp element in stainless steels. The three base elements of stainless steels-iron, chromium and nickel-can dissolve oxygen around their respective melting points. However stainless steel always contains deoxidizing alloying elements such as carbon, manganese, silicon, aluminium or titanium to counter its effect.

2.4 Formation of Martensite

Introduction

Martensite is formed by a deformation of the austenite lattice and without any diffusion of atoms. The deformation causes the transformed region to change its shape, consisting of a large shear and volume expansion. Martensite is, often called as a diffusionless, shear transformation, which is highly crystallographic in nature because it is generated by a specific deformation of the austenite. Thin plates or lathes is developed when the formation of martensite is restricted by its surroundings in order to minimize the strain energy due to the deformation [8]. Occurrence of martensite in ASS significantly changes the properties of the material. The appearance of martensite separations in the austenite matrix results in both positive consequences (e.g. strengthening of material) and negative ones (e.g. a decrease in corrosion resistance, lower fatigue and fracture strength and the appearance of an undesirable magnetic phase) [18]. α' martensite has a bcc structure and is magnetic in nature, which is formed from austenite (γ) which has fcc structure and is non-magnetic in nature.

There are mainly two main types of martensite transformation:

1. Thermal transformation resulting from rapid cooling from (1050 - 110°C), the fcc austenite structure transform to bcc α' martensite below the temperature M_s. [19, 20]
2. Strain-induced martensite (SIM) transformation resulting from the occurrence from plastic deformation. [19]

Martensite can also be obtained in austenitic stainless steel by the application of a strong magnetic field. This thesis will only be focusing on the strain-induced martensite transformation (you can find detailed explanation in section 2.5).

2.4.1 The habit plane

The habit plane is an interface plane between austenite and martensite as measured on a macroscopic scale as can be seen in Figure 2.12. Under unconstrained transformations this plane is generally flat in nature, but under constrained conditions this plane has some curvature to minimize the strains introduced. Steels with different chemical composition can have martensite with the same habit plane and also some other crystallographic characteristics [8].

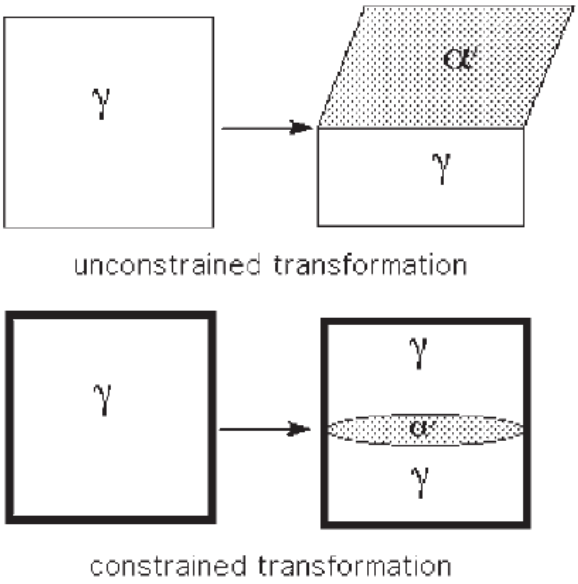

Figure 2.12: *An illustration of habit plane between austenite(γ) and martensite(α').* [8]

2.4.2 Orientation relationships and structure of the interface

The formation of martensite involves the coordinated movement of atoms. This means the austenite and martensite lattices will be related to one another. Therefore, all the martensitic transformations lead to a reproducible orientation relationship between the parent and product lattices [8]. There exist a specific orientation relationship between the new phase(α') and the austenitic matrix (γ) [20].

$$(111)_{\gamma}//(110)_{\alpha'} \tag{2.4}$$

$$[110]_{\gamma}//[111]_{\alpha'} \tag{2.5}$$

Note that these have been stated approximately: the true relations are irrational, meaning that the indices of the parallel planes and directions cannot be expressed using rational numbers. Any process that contributes to the formation of martensite must have a level of continuity across the interface between martensite and austenite. The interface must be coherent or semi-coherent; in the latter case, the dislocations in the interface must be able to glide as the martensite grows. It turns out that a stress-free coherent interface cannot be found between austenite and martensite, the best that can be achieved is semi coherency, with one direction within the interface remaining fully coherent. This direction is known as an *invariant-line* since it is unrotated and undistorted [8].

2.4.3 The shape deformation

The passage of a slip dislocation through a crystal results in the formation of steps like structures where the glide plane intersects the free surface (Figure 2.13 a, b). Shear on a macroscopic level

is caused due to the passage of many such dislocations on parallel planes (Figure 2.13 c, d). Slip can cause a change in the shape but it does not have any effect on the crystal structure, because the Burgers vectors of the dislocations are also lattice vectors [8].

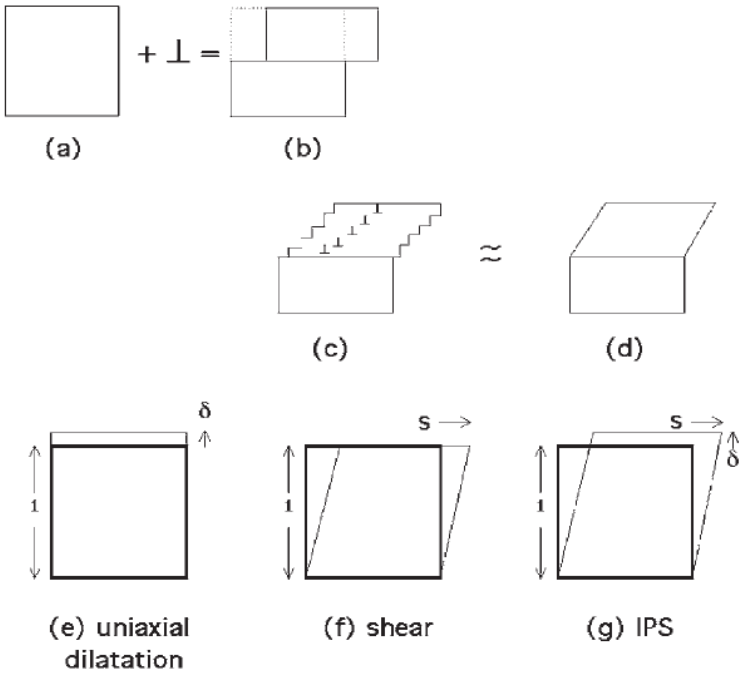

Figure 2.13: *(a) and (b) steps caused due to the passage of slip dislocations. (c) and (d) Macroscopic shear due to many slip dislocations. (e) An invariant-plane strain with a uni-axial dilation. (f) An invariant-plane strain which is a simple shear. (g) An invariant-plane strain resulted due to the combined effect of a uni-axial dilation and a simple shear.* [8]

At the time of martensitic transformation, the way in which atoms in parent crystal are aligned is deformed in such a manner that it is ideal for martensite and due to this there must be a corresponding change in the macroscopic shape of the crystal undergoing transformation [8]. Dislocations which cause the deformation are in the α'/γ interface, with Burgers vectors in such a way that in addition to deformation they also result in a change of crystal structure. Initially the deformation is such that a flat surface is uniformly tilted about the line formed by the intersection of the interface plane and the free surface. Any scratch traversing through the transformed region is deflected in a similar way, even though the scratch remains connected at the α'/γ interface. These types of shape deformation belong to a class of deformations called as invariant plane strains (Figure2.13, e-g), with martensite being the most general case in this class with a combined shear and dilatational strain perpendicular to the habit plane [8].

2.4.4 The crystal structure of martensite

Martensite in steels is a supersaturated solid solution of carbon in ferritic iron. For alloys which have a low martensite-start temperature or a high carbon concentration, the carbon atoms tend to order in such a way that the crystal structure changes from body-centred cubic (bcc) to body-

centred tetragonal (bct). The tetragonality of the ordered martensite, measured by the ratio between the axes, *c/a*, increases with carbon content [8]:

$$\frac{c}{a} = 1 + 0.045 wt\%C \tag{2.5}$$

This means that at zero carbon content the structure would be bcc and free of distortion. The effect of carbon on the lattice parameter of austenite, and on the *c* and *a* parameter of martensite is shown in Figure 2.14 [21].

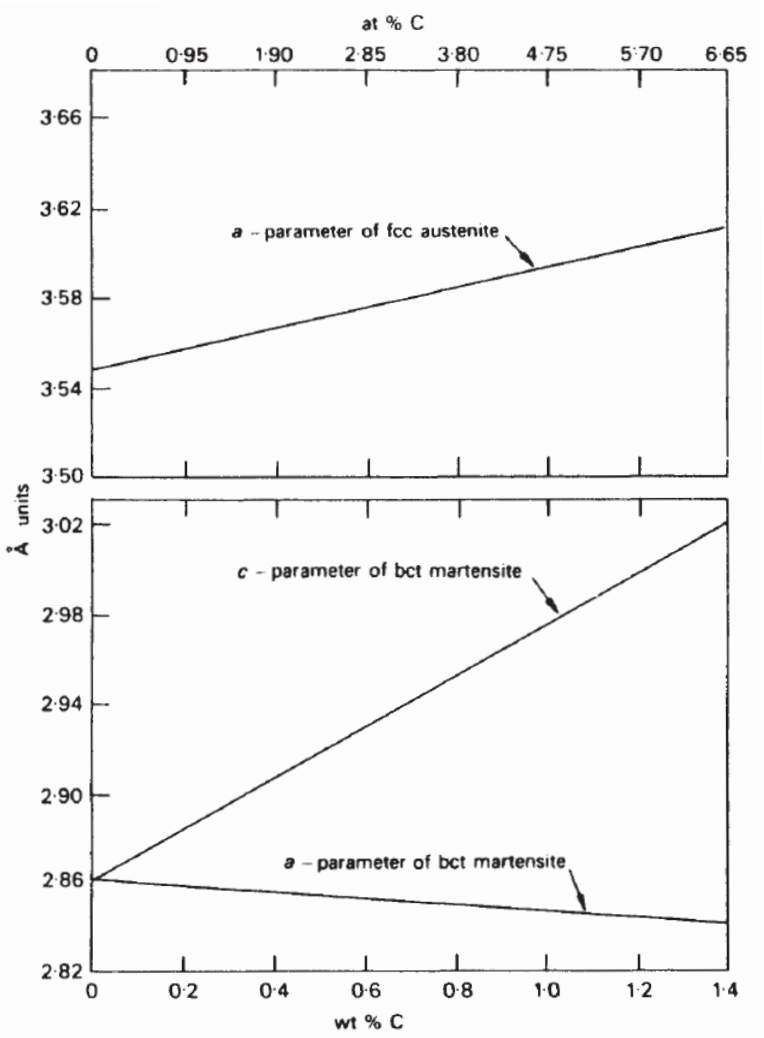

Figure 2.14: *Effect of carbon on the lattice parameters of austenite and of martensite.* [21]

It is interesting to note that carbon in interstitial solid solution expands the fcc iron lattice uniformly, but with bcc iron the expansion is non-symmetrical giving rise to tetragonal distortion. To understand this important difference in behavior, it is necessary to compare the interstitial sites for carbon in the two lattices. In each case, carbon atoms occupy octahedral sites, indicated for martensite in black in Figure 2.15, and have six near-neighbor iron atoms. In the fcc lattice the six iron atoms around each interstitial carbon atoms form a regular octahedron, whereas in the bcc case the corresponding octahedra are not regular, being

shortened along the z-axis. These compressed octahedra only have four-fold symmetry along the shortened axis in each case, in contrast to the fcc structure in which the regular octahedra have three, four-fold axes of symmetry [8].

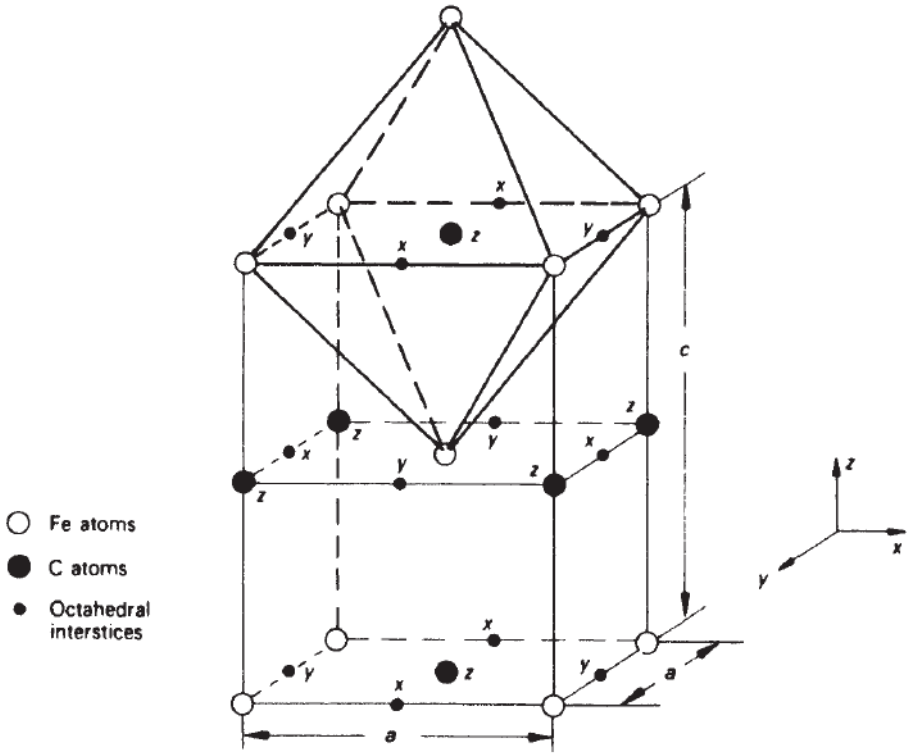

Figure 2.15: *Martensite bct lattice illustrating the three sets of octahedral interstices. The z-set is fully occupied by carbon atoms.* [21]

Examination of the distortion developed by carbon atoms in the several types of sites available in the fcc and bcc lattices, has shown that in the fcc structure the distortion is completely symmetrical, whereas in the case of bcc structure, interstitial atoms in z positions will give rise to much greater expansion of iron−iron atom distances along z than in the x and y positions [8].

Assuming that the face-centered cubic (fcc→bcc) transformation occurs in a diffusionless way and there is no possibility for carbon atoms to move. The ferrite contains three octahedral interstices per iron atom whereas the austenite has only one octahedral interstice per iron atom. Each of the three sets of octahedral interstices (the three sub-lattices) in the ferrite is associated with one of the cube edges of the ferrite unit cell. Upon diffusionless transformation, all the carbon atoms in the austenite end up on just one of the octahedral sublattices of ferrite, causing a tetragonal distortion of the bcc lattice into a bct lattice. Thus, in Fig. 2.15, since only the z sites are common to both the fcc and bcc lattices, on transformation the z-axis becomes the c-axis of the tetragonal form.

Therefore, the tetragonality of martensite arises as a direct result of interstitial solution of carbon atoms in the bcc lattice, together with the preference for a particular type of octahedral site imposed by the diffusionless character of the reaction [8].

2.4.5 Effects of martensite on mechanical properties

The influences of the ε and α' martensite have been studied out in several recent studies. Same as α' martensite, ε can also lead to strengthening mechanism [22]. In a 304 stainless steel, the appearance of ε leads to a rapid decrease in strain hardening, but as soon as α' forms, the rate of strain hardening increases [23]. A uniform distribution of ε produced in high strain rate deformation is believed to enhance ductility in the S31254 superaustenitic stainless steel [24].

Martensitic transformation induced by local stress has the effect of relieving stress concentrations, increasing the work-hardening rate, and promoting homogeneous deformation, with consequent improvements in the strength, ductility and toughness of steels [8].

2.5 Strain-Induced Martensite (α') Transformation

The formation of martensite during deformation is a very common phenomenon in austenitic stainless steels and if steel experiences such transformations, then it is referred as metastable steel. It is reported that a number of factors such as stress, strain, steel chemistry, strain rate, strain path, deformation mode, grain size, grain orientation and temperature of testing effects the formation of deformation induced martensite [25]. Austenitic stainless steels can undergo plastic deformation-induced phase transformation of face-centered cubic (fcc) γ austenite to hexagonal closed packed (hcp) ε-martensite and body-centered cubic (bcc) α'-martensite [26]. The crystal structure is usually referred to as bcc rather than body-centered tetragonal (bct) because of the low interstitial content. ε-martensite (non-magnetic) forms from randomly spaced overlapping stacking faults and α'-martensite (magnetic) forms at shear band intersections [27–29]. Materials have a stacking sequence of atomic planes and there might be interruption in this sequence which may arise due to number of reasons for example manufacturing method, heat treatment, applied stress/strain etc. These stacking faults carry an energy with it and this is known as stacking fault energy (SFE). High stacking fault energy (>20 mJ.m^{-2}) promote direct transformation ($\gamma \rightarrow \alpha'$), while low stacking fault energy (<20 mJ.m^{-2}) leads to the transformation ($\gamma \rightarrow \varepsilon \rightarrow \alpha'$) [30].

The ASS is generally stable at room temperature and can transfer to martensite upon rapid cooling to subzero temperature. The spontaneous martensite transformation begins at M_s-temperature, but the martensite transformation can also be induced by the aid of deformation at higher temperature. As the stress is applied it will generate a positive contribution towards the driving force for austenite to martensite transformation and thus elastic deformation will generate stress-assisted martensitic transformation at temperature above M_s but below the M_s^σ - temperature. The stress-assisted martensitic transformation is generally considered to start at the same sites responsible for spontaneous martensite nucleation e.g. nucleation can occur at grain boundaries [31].

Martensite is also formed above the M_s^σ - temperature and it is called as strain-induced martensitic transformation. The condition to form this type of martensite is that it must be preceded by plastic deformation and the strain induced martensite α' nucleates at sites generated by the plastic deformation, e.g. twins, stacking faults and ε-martensite (hcp). These nucleation sites are often grouped under the name shear-bands, and the nucleation is believed to occur at the intersection of these shear-bands [32]. The nucleation process of martensite has been studied in detail by [33, 34].

The upper limit for the SIM is M_d - temperature and beyond this temperature no martensite will form in the metastable austenitic stainless steel no matter how high is the strain applied.

Figure 2.16 below shows schematic illustration of the critical stress to initiate martensite transformation as a function of temperature [32]. Below the M_s - temperature martensite will form spontaneously without the aid of stress. Between the M_s and M_s^σ - temperature

martensite will form with the aid of applied stress. With increasing temperature, the stress required to initiate transformation increases, meaning that yielding becomes easier with a decrease in temperature below M_s. Above M_s^σ yielding first occur by slip and then martensite is formed at the potent nucleation sites newly generated by the slip. The yield stress decreases with increasing temperature above M_s^σ and the stress necessary to initiate strain-induced martensite is close to the yield stress at temperatures just above M_s^σ, but it is significantly higher than the yield stress at higher temperatures [31].

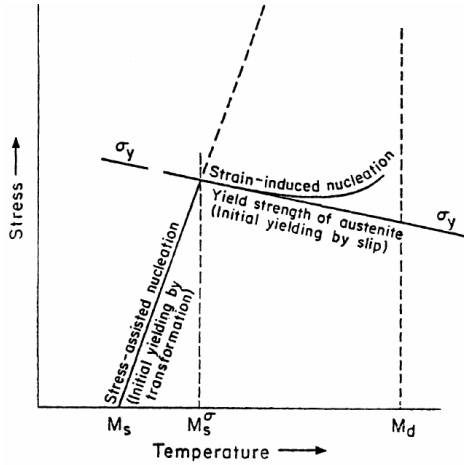

Figure 2.16: *Schematic illustration of the critical stress to initiate martensite transformation as a function of temperature.* [32]

2.5.1 Thermodynamics of strain-induced martensite transformation

Austenite (the parent phase) will decompose into martensite when the free energy of austenite is greater than that of free energy of martensite. The difference in energy between austenite and martensite may be regarded as the driving force behind the martensite transformation [19]. Figure 2.17 below represents the change in chemical free energies of martensite and austenite (parent phase) with temperature. In the Figure 2.17, T_o represents the temperature at which martensite(α') and austenite(γ) are in equilibrium, and M_s is the point at which transformation starts on cooling. The difference in free energies between austenite and martensite, $\Delta G_{M_s}\gamma\rightarrow\alpha'$ at the M_s temperature is the driving force for the onset of the martensitic transformation.

However, martensite transformation can also occur at the temperatures $T_1(>M_s)$, if a sufficient mechanical driving force U' is applied [35] , such that:

$$\Delta G_{T_1}^{\gamma\rightarrow\alpha'} + U' = \Delta G_{M_s}^{\gamma\rightarrow\alpha'} \tag{2.6}$$

The mechanical driving force is believed to originate from the applied stress, which in turn aids the chemical driving force. Below is the expression for mechanical driving force as a function of stress and orientation [36].

$$U' = \tau s_o + \sigma\epsilon_o = \frac{1}{2}s_o\sigma sin2\theta \pm \frac{1}{2}\epsilon_o\sigma(1 \pm cos2\theta) \tag{2.7}$$

where the terms τs_0 and $\sigma\epsilon_o$ represent the work done by the shear and normal stresses respectively. θ is the angle between the stress axis and the normal of the habit plane and σ denotes the absolute value of the applied stress. The plus and minus signs represent tensile and compressive stress, respectively. Figure 2.17 shows that the chemical driving force for martensitic transformation decreases linearly with the increasing temperature. Equation (2.7) shows that stress level responsible for mechanical driving force also increases linearly and this linear relationship has been shown to be valid up to the stress level corresponding to the yield strength of the austenite, which is shown in Figure 2.16.

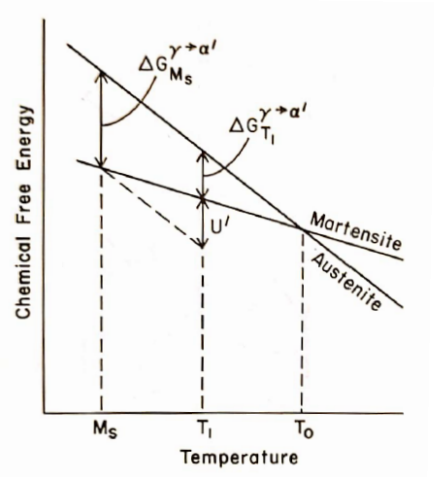

Figure 2.17: *Schematic illustration of the critical stress to initiate martensite transformation as a function of temperature.* [32]

2.5.2 Special sites for strain-induced nucleation

The formation of ε (hcp) martensite in γ (fcc) austenite of low stacking-fault energy is well-established [37]. There have been some instances in which ε has been observed to provide favorable nucleation sites for the formation of α' (bcc or bct) martensite.

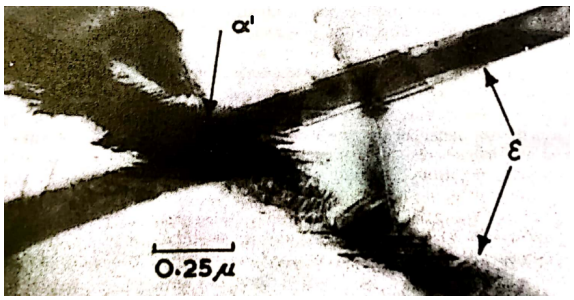

Figure 2.18: *Nucleation of α'-martensite at the intersection of two ε plates in ASS.* [37]

Figure 2.18 above, shows α' formed at the intersection of two ε plates in an austenitic stainless steel (type 304) deformed at 78 K [37]. It is clearly a case where a nucleating site has been created by plastic straining. The α' thus generated may be constructed as a strain-induced embryo; it has not triggered-off into a countable martensite plate in the sense of operational

nucleation [32]. According to [38] it is found that α' can be nucleated by the intersection of two ε plates or by the intersection of an ε plate with a twin or grain boundary in the austenite.

It is worth noting that ε intersections obviously play an important role in the strain-induced nucleation of α' martensite, but this might not be true in all case even ε can form in alloys. (R Lagneborgj) [39] has noted, and later confirmed by [40], that α' can be generated in austenitic grains which are so oriented relative to the tensile-straining axis that ε formation is suppressed. Similarly, (Breedis and Kaufman) [41] have also concluded that α' can nucleate independently of the ε, particularly in those cases where the ε is not even thermodynamically stable with respect to either the γ or α'.

The formation of α' martensite affects significantly the mechanical behavior of the steels by enhancing the work hardening. The amount of α'-martensite increases with increasing plastic strain at the expense of austenite and ε-martensite phases [42]. Strain-induced martensite (SIM) is often seen in stainless steels during forming and machining operations, such as deep-drawing, wire drawing, grinding or polishing. The extent of α'-martensite transformation depends strongly on the steel composition and the temperature at which the deformation takes place [43].

Figure 2.19 shows the extent of martensite transformation as a function of temperature and true elongation for an 18Cr-8Ni type austenitic stainless steel [44]. It can be seen as the temperature is lowered there is more martensite formation. At room temperature, the influence of alloy chemistry on the martensite transformation is illustrated in Figure 2.20, which shows the amount of magnetic α' as a function of cold-rolling reduction for 18Cr-8Ni, 18Cr-12Ni and 18Cr-12Ni-Ti austenitic grades.

The effect of alloying elements (in weight%) is described by the formula:

$$-M_{d30}(^{\circ}C) = 497 - 462(C + N) - 9.2(Si) - 8.1(Mn) - 13.7(Cr) - 20(Ni) - 18.5(Mo) \tag{2.8}$$

Where M_{d30} is the temperature at which 50% of martensite has formed for true strain of 30% [45]. An increase in the nickel content inhibits the formation of strain induced martensite α', while stabilization with titanium exerts the opposite effect, by reducing the amount of carbon and nitrogen in solid solution.

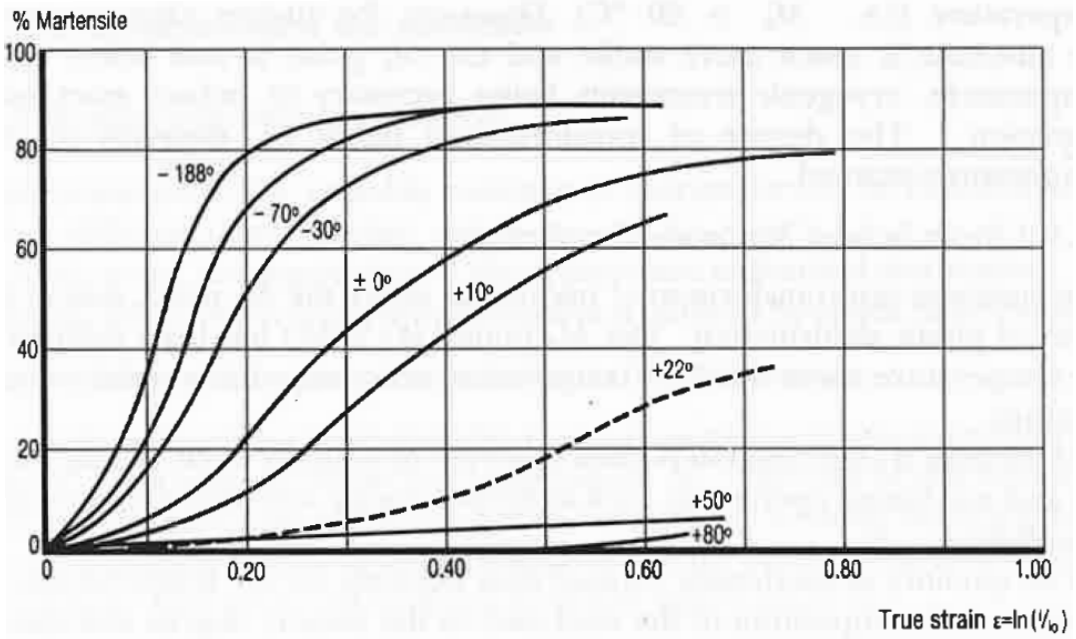

Figure 2.19: *Effect of true elongation $\epsilon = ln(l/l_o)$ on the extent of martensite transformation at different temperatures, in a type 18Cr-8Ni austenitic stainless steel.* [44]

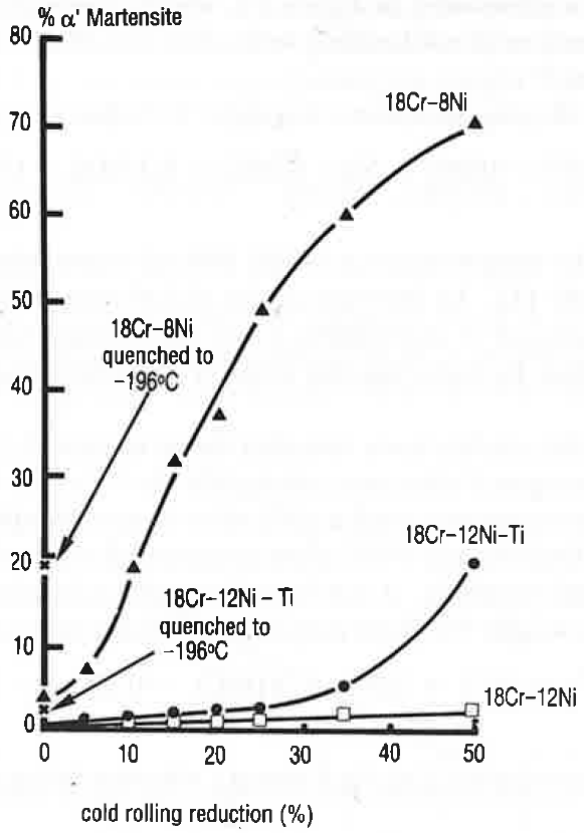

Figure 2.20: *Effect of room temperature rolling reduction and cryogenic treatment at -196°C on the amount of α′ martensite in three austenitic stainless steel.* [46, 47]

Crystallographic studies have revealed the presence of ε martensite, with closed-packed hexagonal structure, alongside the bcc α'-martensite. The ε -martensite is non-magnetic, and is difficult to detect by optical microscopy, hence its identification requires diffraction techniques.

The stacking fault energy (SFE) plays an essential role in the strain-induced martensite transformation. It can be calculated as a function of chemical composition (in weight %), from the empirical formula given below [45].

$$-SFE(mJ.m^{-2}) = 25.7 + 2(Ni) + 410(C) - 0.9(Cr) - 77(N - 13(Si) - 1.2(Mn) \tag{2.9}$$

Nickel increases the stacking fault energy, whereas manganese and nitrogen decrease it.

The ε martensite phase is formed in steels with low stacking fault energy, either by cryogenic quenching (-196°C), when SFE < 43 mJ.m^{-2}, or by quenching to room temperature and cold working, when SFE < 30 mJ.m^{-2} [11].

No relationship has been established between alloy chemistry and the M_s or M_d points for ε martensite. As for α' martensite, the formation of ε martensite is independent of diffusion, and the crystallites of this phase grow in certain privileged directions in the matrix.

Reversion of ε and α' martensite to γ austenite

The ε and α' martensite are metastable phases and can be transformed back to γ austenite at high temperatures. X-ray diffraction analysis has shown that reversion of ϵ-martensite occurs in the temperature range 150-400°C as studied by the author (DR Harries) [46], whilst α'-martensite to γ reversion in 50% cold-worked 18Cr-8Ni steel takes place at temperatures of 400-800°C for annealing times of 20h (Figure 2.21) according to (DR Harries) [46]. However, the α' to γ reversion has been variously reported to occur at 500-600°C [48] and at about 570 - 700 - 850°C [46] in austenitic steels of differing composition. The reversion occurs principally by a diffusionless shear mechanism during rapid heating or annealing for short times but some thermally activated reversion can also occur with relatively slow heating rates [49]. The reverted γ usually has an almost identical orientation to the original untransformed γ but may contain a high density of tangled dislocation, fine twins and/or stacking faults [49]. This thesis work will not go through the study of reversion of martensite to austenite because it's not the main objective to be achieved.

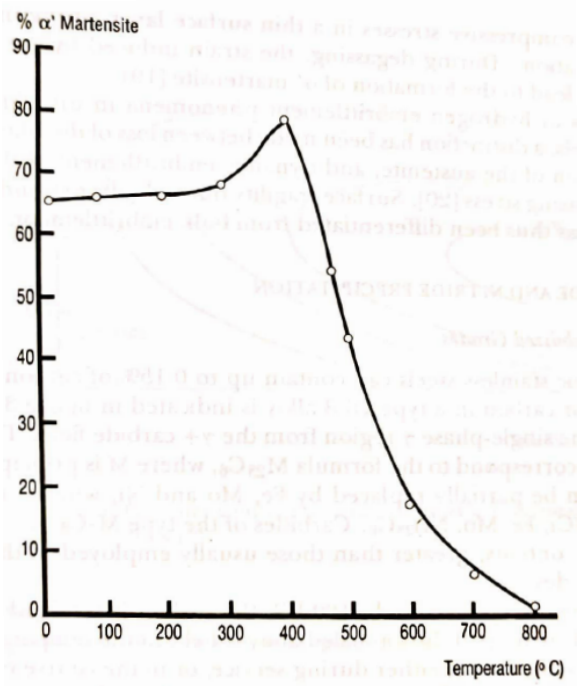

Figure 2.21: *Effect of annealing for 20h on α-martensite reversion in 50% cold-worked 18Cr-8Ni steel.* [46]

.

2.5.3 Methods for detection of α' induced martensite

There are several techniques to detect the strain-induced martensite α' in ASS. Below is a list of methods which can be used for its examination:

- By measuring the magnetic parameters such as ferrite content, coercivity, remanence, and saturation magnetization because when α'-martensite is formed it is magnetic in nature which is formed by a non-magnetic γ-austenite phase. Ferrite content can be measured by using Ferritescope, a device that is normally used to measure the δ-ferrite content of austenitic stainless steel weldments [50]. Coercivity, remanence and saturation magnetization can be found out using Magnetic force microscope (MFM) [51].

- The use of nonlinear ultrasonic methods can be used for an understanding of the evolution and accumulation of the plastic deformation of materials occurring in the very early stages of fatigue [52–55]. Various authors have stated that an enhanced generation of high-order harmonics can be seen as a result from distortion of ultrasonic waves propagated through the materials, and recent experimental studies and physical models provide strong evidence that the ultrasonic non-linearity parameter β is highly dependent on fatigue degradation [56, 57].

- Neutron diffraction (ND), can be used in evaluation of microstructure of steel. Volume fraction and texture of retained γ-austenite can be simultaneously measured using neutron

diffraction [58].

- X-ray diffraction (XRD), can be used to investigate the transportation of the martensite phase in AISI 316 steel. According to [51] the XRD profiles of the fatigue-failed specimens under various strain amplitudes are shown in [51]. The diffraction peak of $2\theta = 44.5°$is defined as delta ferrite (δ) in the as-received sample. The intensity of this peak increased with a higher strain amplitude, as indexed with $\delta + \alpha'$. This increase in XRD intensity was caused by the strain-induced formation of martensite (α'). Additionally, the intensity of the α'-martensite diffraction peaks increased as the strain amplitude was increased [51].

- We can also examine the formation of strain induced martensite by using various different microscopes such as optical microscope, TEM and SEM by studying the change in microstructure. TEM can be used to examine the dislocation substructure in as-received specimen and in specimen after deformation. The typical dislocation cell microstructure was well developed in [51]. The initial cyclic hardening was attributed to the increased dislocation density, and the subsequent softening was ascribed to the formation of dislocation cells resulting from fatigue [51]. With the help of optical microscope, we can perform image examination to look for formed martensite and compare it with as received samples. Electron channeling contrast imaging (ECCI) and electron backscattering diffraction (EBSD) techniques can be performed using SEM for microstructure analysis [59].

- By comparing the hardness of the as received sample and the strained sample we may also say that the hardness of the material might have increased due to the formation of α'-martensite.

The project work will be mainly carried out using methods such as XRD, EBSD, SEM, TEM, Optical microscopy and hardness measurement to study the amount of SIM formed. Due to the limitation of equipment available at the university, experimental investigation will be limited to the above-mentioned methods. The detailed experimental methods and processes used to carry out the work are discussed in the further chapter of 'Experimental Methodology'.

2.6 Results from Previous Work Done

A number of research has been carried out by different authors to find out strain induced martensite (α') in 316L ASS, but the test condition varies from work done by author to author and most of the work has been done relating to analysis of fatigue failure of material. According to the findings of (Chungseok) [51], Strain induced martensite can be seen in 316L material around strain amplitude of 3% under fatigue failure condition. (Chungseok) has used several different methods to validate his results such as magnetic and acoustic NDT techniques, microstructure examination using optical microscope, SEM and TEM. (Chungseok) [51] concludes that the volume fraction of strain-induced martensite increases with the strain amplitude under fatigue failure condition.

Work done in article [59] had examined the stability of austenitic 316L steel against martensite formation under fatigue loading condition. In his work, author has used heat treated (solution annealing at 1080°C/water quenching) material which was subjected to fatigue deformation. Author examination method includes, neutron diffraction (ND), Ferritescope, EBSD, ECCI and TEM. He concluded his finding by stating that no deformation-induced martensite was detected in the bulk by Neutron diffraction (ND) At room temperature under fatigue loading even with very high plastic strain amplitude of 5% until fracture. No and/or only limited amount of α' - martensite (with small variations around the specimen circumference) were found by the ferritescope (FS) close to the fracture surface [59]. Authors of literature [59] concludes that, AISI 316L at room temperature exhibits a very high stability of austenite during cyclic straining (fatigue failure) up to strain amplitudes of 5%. No deformation-induced martensite was detected in the bulk of material during room temperature straining. Very limited martensite formation was revealed only on fracture surface produced by the growth of long fatigue cracks.

It can be seen that there is a contradicting result between the findings in literature [51] and [59]. The main reason for this contradiction is that in [59] the material was heat treated before deforming and it is well known from previous works that by performing heat treatment the chances of strain induced martensite (SIM) transformation is reduced. Whereas in article [51] there was no heat treatment done to the material.

Work done in this project is quite unique because two types of deformation is studied in this project first one is cyclically deformation (without failure) and other one is tensile failed specimen at various temperature.

2.7 Material Examination Methods

2.7.1 Optical microscope (OM)

Optical microscope is an instrument that uses visible light to create a magnified image of an object which is projected onto the retina of the eye or onto the photosensitive surface of an imaging device [60]. In a *compound light microscope* two lenses, the objective and the eyepiece (or ocular), are responsible to produce the final magnification M of the image such that:

$$M_{final} = M_{obj} \times M_{oc} \tag{2.10}$$

Two important components in optical microscope for image formation are: (1) the *objective*, which uses diffracted light by the specimen and forms a magnified real image near the eyepieces/oculars, which is known as the real intermediate image plane, and (2) the *condenser*, the condenser, which focuses light from the illuminator onto a small region of the sample [60]. Figure 2.22 shows how an image is magnified and perceived by the eye. It also shows the important focal planes in relation to the objective, the ocular, and the eye. Due to limited resolving power of visible light the maximum magnification power of OM is typically limited to around 1000x resolution.

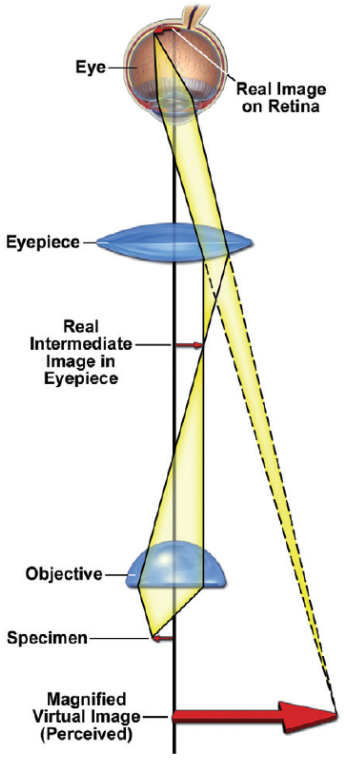

Figure 2.22: *How a magnified virtual image of a specimen is perceived in optical microscope.* [60]

2.7.2 Scanning electron microscope (SEM)

SEM is mainly used to study the surface or near surface structures in the specimen. Its main application is to examine topography, morphology, crystallographic information and composition of a given sample. It uses electron beam to study the specimen. Figure 2.23 below is the schematic SEM diagram, showing the main components and mode of operation. Electron source (gun) is primarily of tungsten filament thermionic emission type, but field emission guns are also employed for higher resolution examination [61]. Electrons are accelerated to an energy in the range of 1 keV to 30 keV. The beams of electrons are de-magnified using two or three condenser lenses to a spot size of 2-10 nm in diameter. The beam than passes through pairs of scanning coils or pairs of deflector plates in the electron column, typically in objective lens which deflects the beam in the x and y axes such that it scans in a raster fashion over a rectangular area of specimen. Electrons loses its energy when primary electron beam interact with the sample by repeated random scattering and absorption in a drop-shaped volume of the specimen known as *interaction volume* as shown in Figure 2.24b. A number of rays are emitted (see Figure 2.24a) when an electron beam hits the specimen. The reflected rays are result of repulsion and elastic scattering and are captured through various special detectors designed for each ray. The signal through the detector is processed further and finally we receive a magnified and high-resolution image of our sample [61].

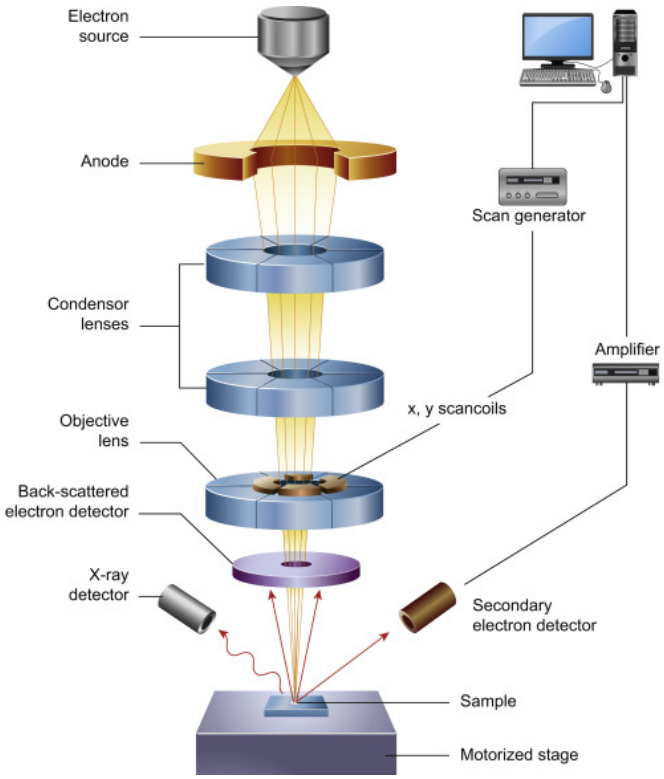

Figure 2.23: *Schematic diagram of SEM.* [62]

.

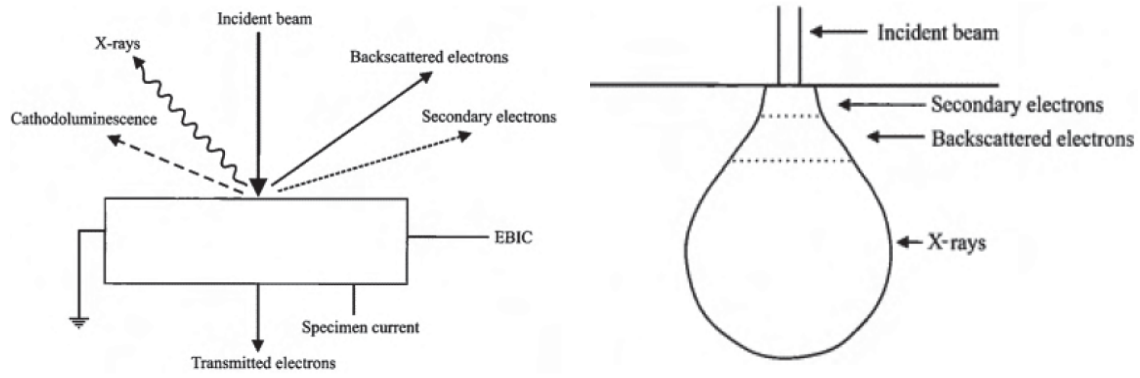

Figure 2.24: *(a) Different rays coming out when electron beam hits the specimen, (b) Interaction volume through which secondary electrons, backscattered electrons and characteristic X-rays may be detected.* [61]

Energy dispersive spectroscopy (EDS)

A SEM has also the capability to perform EDS and EBSD. EDS is an analytical method used for chemical characterization of a sample. When high energy electron beam hits the specimen, characteristic X-rays are produced and this X-rays are proportional to the mass fraction of the element in the specimen [63]. In EDS, X-rays are detected by a solid-state spectrometer which converts them to electrical pulses proportional to the characteristic X-ray energies. So, by comparing the X-ray intensity of each element to that of standard known composition, the mass fraction of each element can be calculated [63].

Electron backscatter diffraction (EBSD)

The main advantage of this method is the possibility to link morphology (grain size and shape) with crystallographic features (phase, orientation, disorientation) on the microscopic scale. In EBSD, an electronic backscatter pattern (EBSP) is created, an image consisting of relatively intense bands (Kikuchi bands) which intersects with one another and overlay the normal distribution of backscattered electrons, due to Bragg diffraction of electrons by atomic planes in the crystal lattice [63]. Results obtained from EBSD can be compared by TEM, but the specimen preparation method for EBSD is much simpler as compared to TEM specimen preparation. However, specimen preparation for EBSD is complex as compared to normal imaging in SEM, because of very low information depth of the EBSD signal based on channeling effects. Etching is generally not required for EBSD because the contrast is defined through the orientation differences. Etching should be avoided (oxide polishing suspension (OPS) can be done), as the induced surface roughening is disturbing due to the high specimen tilt (70°) during the examination process.

2.7.3 Transmission electron microscope (TEM)

In TEM an electron beam is transmitted through the specimen to create an image. It has an accelerating voltage values between 100 to 300 keV [64]. The higher is the accelerating voltage, the easier it is for electron to penetrate the thicker specimen. For example, at 100 keV voltage maximum thickness of specimen is of order 200 nm and at 200 keV it is 1000 nm. A very high-resolution image and rows of atomic columns can be obtained using TEM because, a high accelerating voltage results in low wavelength of electrons, about 1/100000 of the wavelength of visible light [64]. By the help of TEM, we can perform imaging of microstructure (grain boundaries, dislocations, defects etc.), diffraction and different forms of spectroscopy of the given specimen. Electron beams penetrates the specimen and during this process they are diffracted by different planes at crystal lattice and interferences arise. By the help of diffraction patterns obtained, we can know about the lattice structure of the specimen. Below Figure 2.25 shows the schematic diagram of TEM. The main challenge with working on TEM is the sample preparation. A prerequisite for TEM sample is that it should be sufficient thin such that electrons can easily pass through it and thick enough for their structural features to remain verifiable. In TEM by observing the diffraction pattern and indexing it in correct manner we can get information about the phase present in certain region and also some details related to the microstructure.

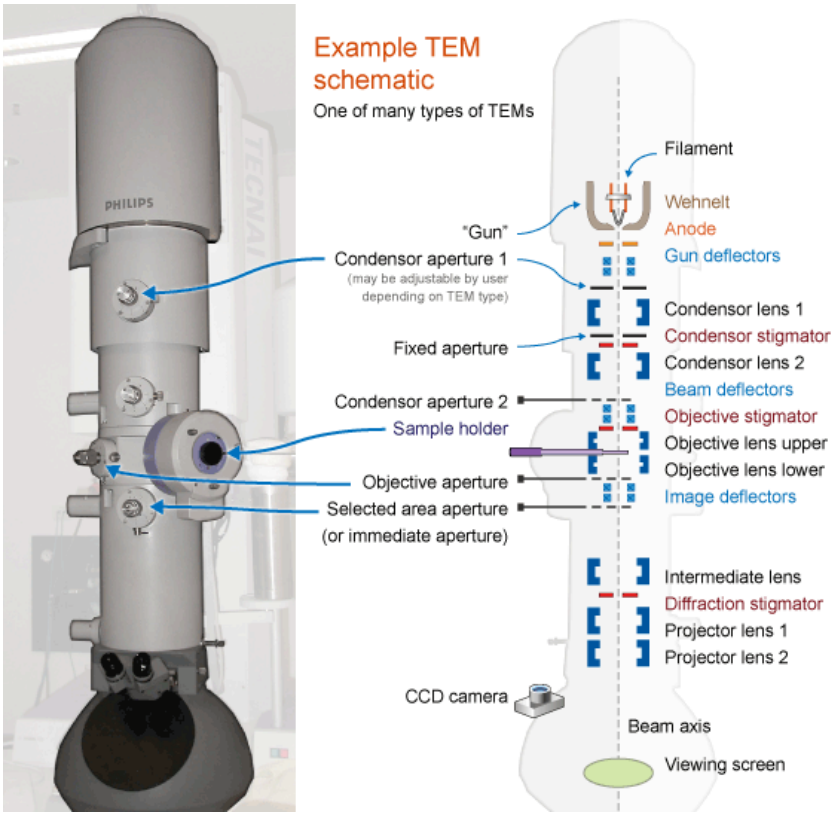

Figure 2.25: *Schematic diagram of TEM.* [65]

2.7.4 X-ray diffraction (XRD)

X-ray diffraction (XRD) is an analytical method that can provide information about unit cell dimensions and is mainly used for phase identification of crystalline materials. Crystalline structure of an atom diffracts the incoming X-ray into various directions. When the X-ray hits an atom, electrons in atom act as a new source of waves and these waves have destructive and constructive interference according to the Bragg's law [66]:

$$2d\,sin\theta = n\lambda \tag{2.11}$$

Where 'd' is the distance between the diffracting planes, 'θ' is the incident angle, 'n' is any integer and 'λ' is the wavelength of the beam (see Figure 3.4d). By measuring the angle and intensities of a diffracted beams, a crystallographer can generate a three-dimensional picture of the density of electrons within the crystal. This electron density can give information such as mean position of the atoms in crystal, chemical bonds, crystallographic arrangement, crystallographic disorder and various other information [66]. An X-ray diffraction pattern is a plot between the intensity of X-rays versus beam scattering angle by the sample. The detector moves in a circle around the sample and its position is recorded as the angle 2θ (see Figure 3.4a). Each "phase" in the sample produces a unique diffraction pattern. Experimental XRD data obtained are compared with the reference data (patterns) to determine which all phases are present [67]. The reference pattern will be denoted by sticks in the graph. If all the major peaks listed in the reference pattern is not shown in the experimental data, then that is not a good match. We cannot guess the relative amounts of phases present based upon the plots of relative intensities of the diffraction peaks. Broadening of diffraction peak may contain the information about the sample microstructure [67].

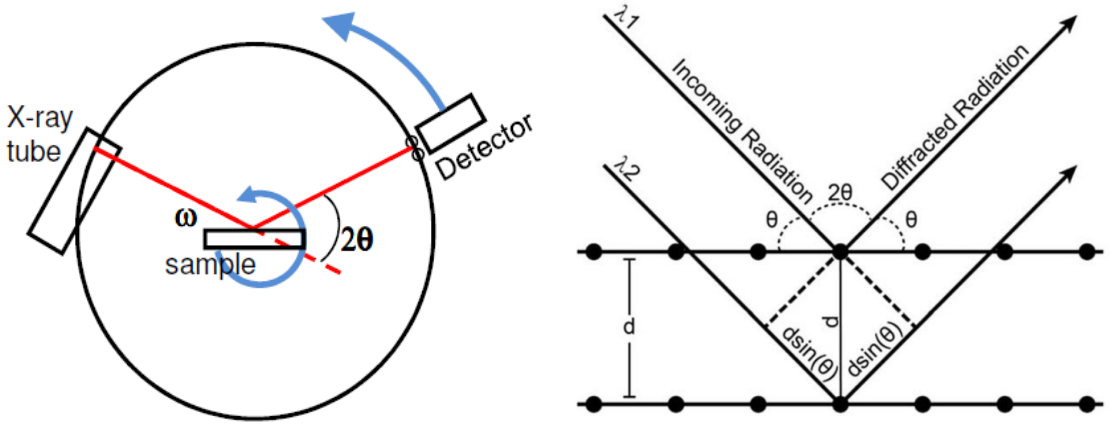

(a) **(b)**

Figure 2.26: *(a) Schematic drawing of XRD [67], (b) Figure representing Bragg's law. [66]*

2.7.5 Hardness test

Hardness of a material can be defined as the resistance to localized plastic deformation induced by mechanical indentation or abrasion. There are different measurements of hardness such as scratch hardness, rebound hardness and indentation hardness. Indentation hardness computes the resistance of a material deformation caused by a constant load from a sharp object. Commonly used indentation hardness scales are Rockwell, Vickers, and Brinell [68].

Vickers hardness is frequently used to assess mechanical properties of the material because pyramidal shaped (See Figure 2.27) indenters cause yielding of the indented material at a lower load and hence can also be used to examine the properties of very thin materials [69]. In this thesis Vickers hardness measurement technique have been used. In Vickers hardness the size of the indentation mark is measured. A soft material will have large indent size giving low hardness value, while a hard material will have small indent size giving high hardness value. The load can vary from 1 to 120 kg, but the hardness value obtained at different loads will be same. Below equation (2.13) shows the formula to calculate hardness value.

$$d = \frac{d_1 + d_2}{2} \tag{2.12}$$

$$HV = \frac{1.8544F}{d^2} \tag{2.13}$$

Where, HV = Vickers hardness, F = load in Kg, d = mean value of d_1 and d_2 in mm

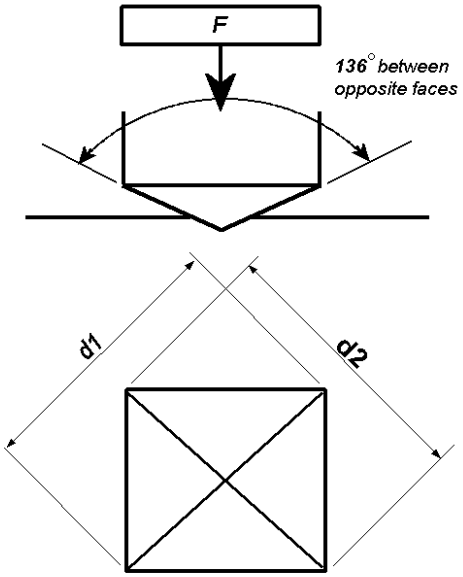

Figure 2.27: *Schematic diagram of Vickers hardness test Indent.* [70]

3 Experimental Methodology

3.1 Material used

The material used for this thesis is austenitic stainless steel AISI 316L. The material was provided by Subsea7, Norway in the form of a section of pipe used for offshore applications. The dimension was 550 mm in length and 273.10 mm outside diameter with thickness of 18.90 (15.90 + 3) mm. The pipe is made up of plain carbon but had a 3 mm inner layer of ASS 316L inside to protect it from corrosion. My thesis examination will be restricted in this 3 mm austenitic layer material. The pipe is fabricated in such a manner that one plate of plain carbon steel and one plate of 316L stainless steel (3 mm layer) is hot rolled together which produces a metallurgical bond between the two plates. The plates are bend to take a pipe shape structure and then a longitudinal weld is done to complete the pipe. Below Figure 3.1 shows the as received material and Table 3.1 shows the chemical composition of plain carbon steel and ASS 316L material.

Table 3.1: *Chemical composition of received sample material.*

Material	Cr	Ni	Mo	Mn	N	C	Si	P	S	Ti	Cu
316L ASS	16.640	10.610	2.550	1.830	0.0820	0.017	0.320	0.030	0.0010	-	-
PC steel	0.174	0.480	0.119	1.640	0.0049	0.034	0.192	0.006	0.0003	0.002	0.032

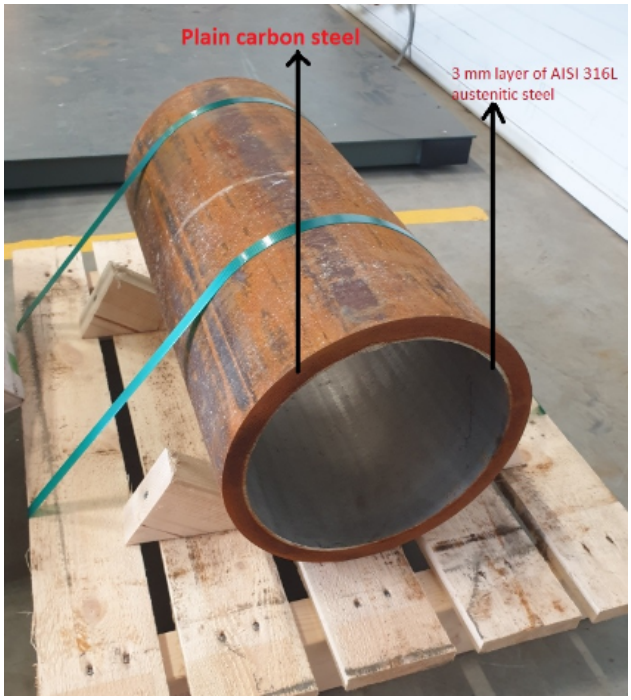

Figure 3.1: *As received pipe material from Subsea7.*

3.2 Straining of material

3.2.1 Specimen preparation for straining the material using tensile testing machine

Since the material received was a section of pipe, first step was to make a dogbone shape like structure according to ASTM standard in order to strain it using 250kN INSTRON uniaxial tensile test machine. For that a couple of machining operation was performed. Below Figure 3.2(a-f) summarizes the machining methods used for making the specimen.

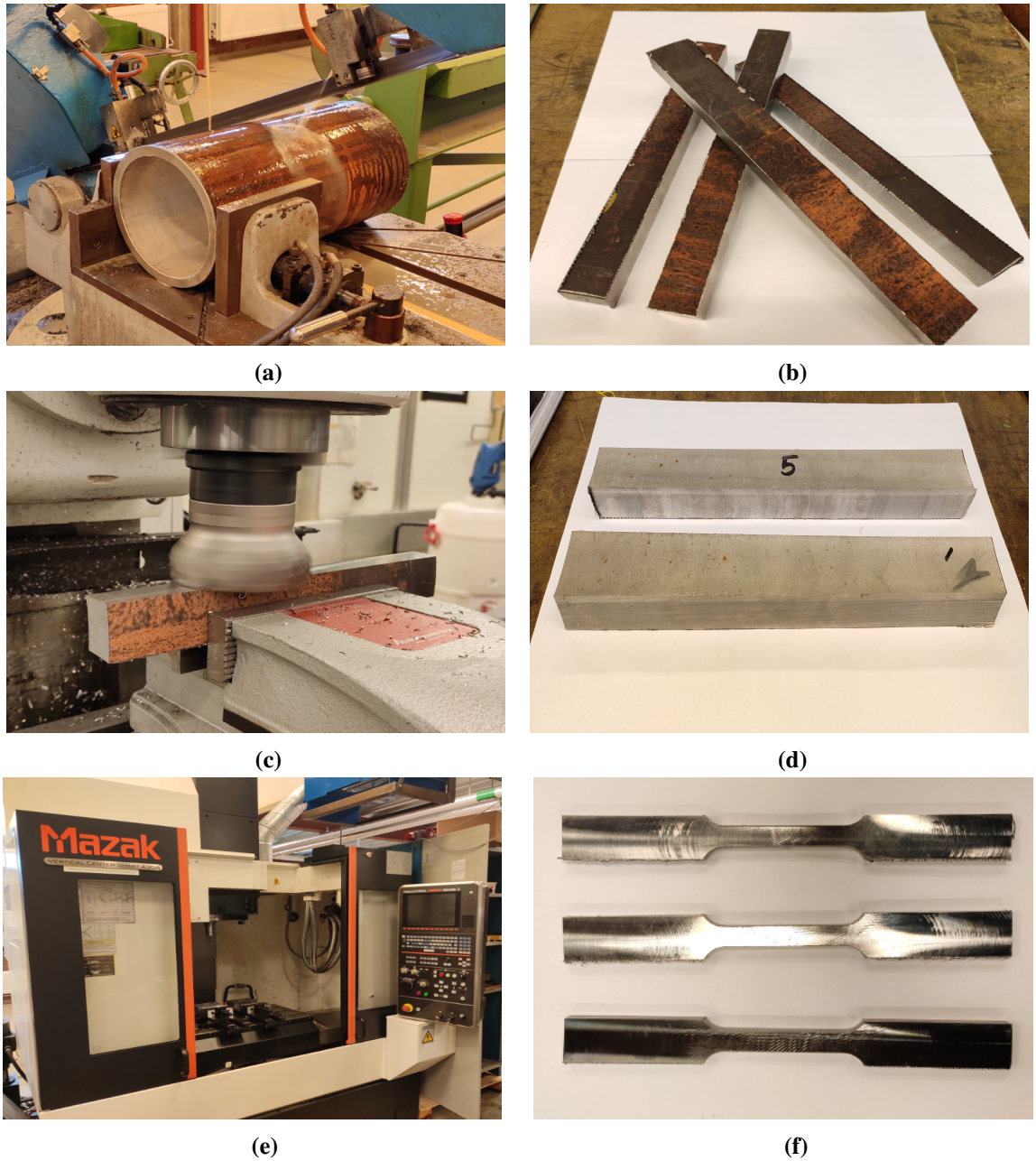

Figure 3.2: *(a) Shows the cutting of pipe using saw machine, (b) The cutted pipe in shape of horizontal bar of approximately 30 mm in width and 250 mm in length, (c) Milling operation of cutted part to make flat on both side and reduce its thickness to 26 mm so that it can be machined in CNC, (d) Final milled part ready for CNC machining, (e) CNC machine used for making final specimen for deformation, (f) Final part, made by CNC which was deformed using tensile test machine.*

Making the final specimen for deformation was quite challenging and time-consuming task. It required a lot of effort and time in machining the part. Below Figure 3.3 shows the dimension of the specimen to be made by CNC machine. A total of 15 such specimen was prepared using CNC machine. CNC machining operation was performed by lab engineer, apart from that all the machining operations was performed by the author of this work (cutting and milling). Below Table 3.2 shows the machining operation, machines used and approximate machining time for each step during specimen preparation.

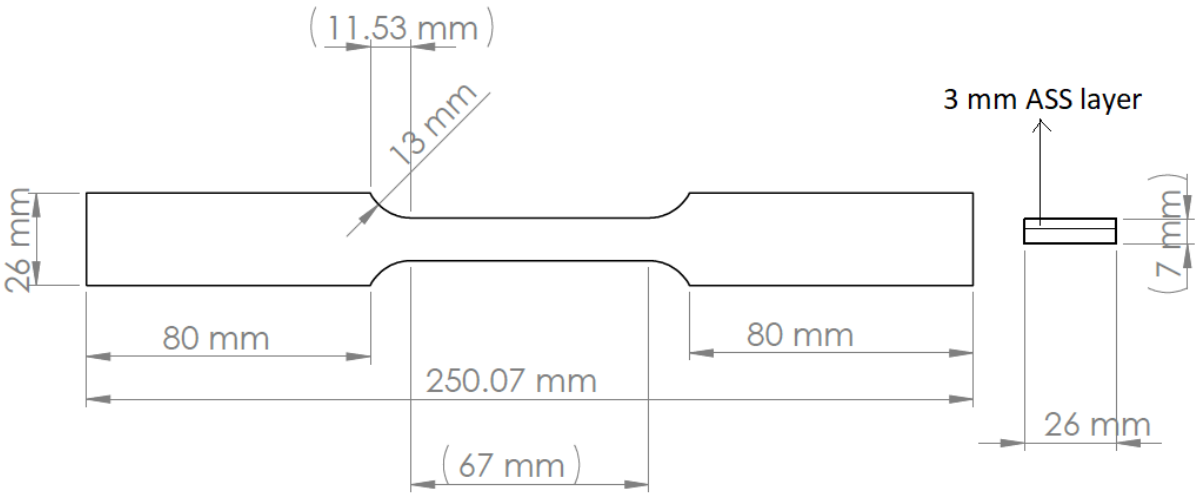

Figure 3.3: *Engineering drawing of specimen used for straining.*

Table 3.2: *Machining method and time consumed.*

Machining process	**Time consumed**	**Machine used**
Cutting	6 hours (approx.)	Band saw SOMATEC cutting machine
Manual milling	50 hours (approx.)	JAFO FWF32 milling machine
CNC	8 hours (approx.)	Mazak vertical center smart 430A CNC machine

3.2.2 Method of deformation

The sample prepared after CNC machining was deformed using 250kN INSTRON uniaxial tensile testing machine. The samples were deformed under different test parameters, Table 3.3 below describes all the parameters in detail used for deformation. Few samples were cyclically deformed at certain strain rate and strain amplitudes (no failure), few were tensile tested until failure in room temperature and in depressed and elevated temperature. Below Figure 3.4 shows the tensile machine used for deformation.

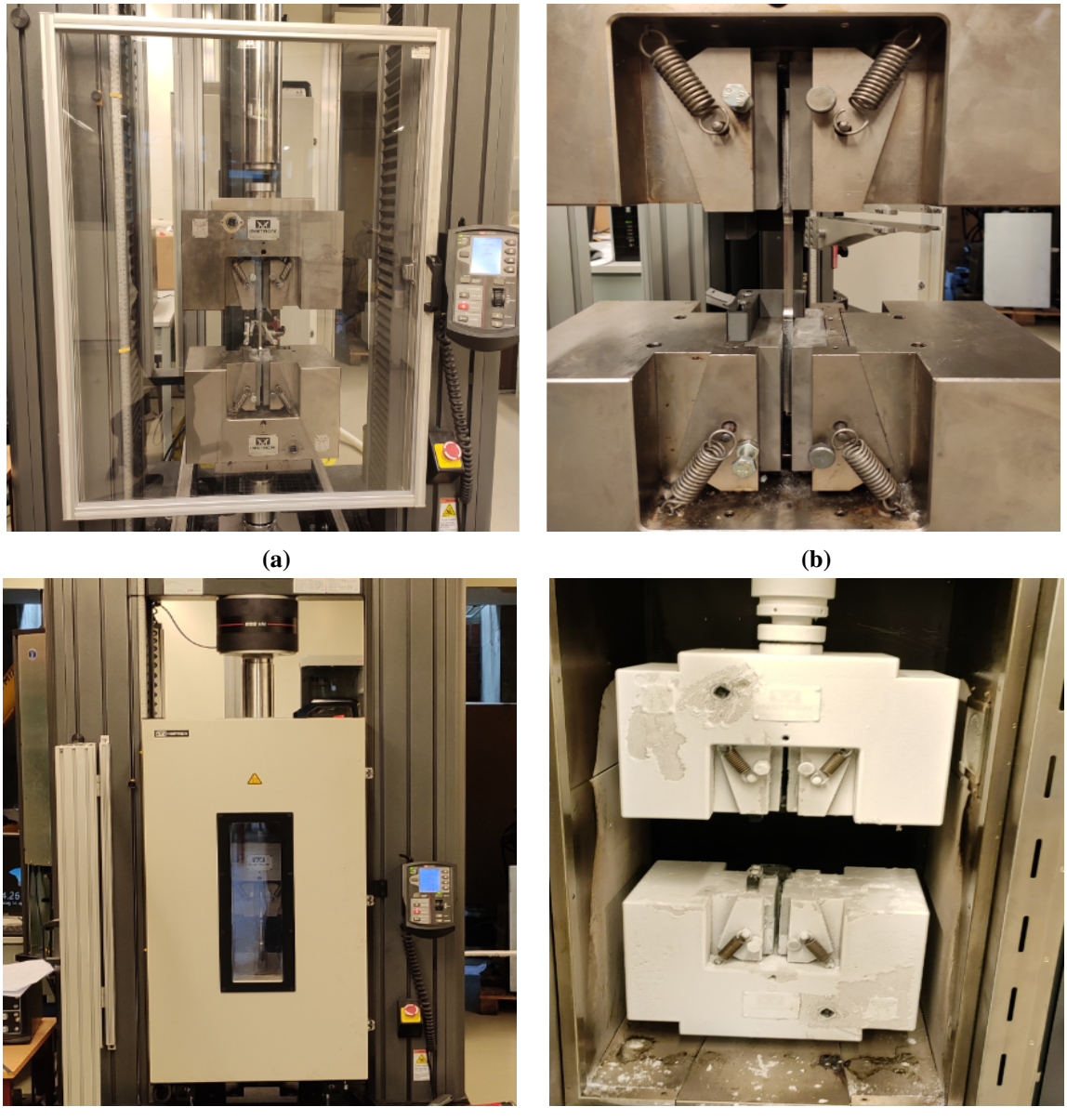

(a) **(b)**

(c) **(d)**

Figure 3.4: *(a) Figure of 250kN INSTRON uniaxial tensile testing machine used, (b) Tensile machine rig jaw holding the sample at room temperature, (c) Tensile machine set up (White chamber used is for maintaining certain required temperature) for performing straining at depressed and elevated temperatures, (d) Specimen holding jaws after application under -80°C.*

All the deformation and straining of the specimens were done independently except the test done in varied temperature part. For cyclic straining, the number for cycles used was six. This data was provided by the company Subsea7 because they told that around six times the pipeline may experience cyclic strain during reeling and un-reeling pipeline operation. The values of strain rate and strain amplitude used in this work was also provided by the company. The tensile failure observation is also carried in this work in addition to the observation of deformed specimen. For tensile failure under different temperature condition, first the test chamber was brought into the desired test condition environment. Liquid nitrogen container was connected to the test chamber and an in-built fan was used to create an environment of -80°C. For operating at elevated temperature (100°C) heating coils fitted in the chamber was used to make that environment. It took approximately 45 minutes to bring the test chamber at -80°C and approximately 25 minutes to bring the chamber to 100°C.

Table 3.3: *Various straining test condition used.*

Spec. No	**Test Type**	**Temperature (°C)**	**Strain amplitude (%)**	**Strain rate (per second)**
15	cyclic	23	1 (six cycles)	5×10^{-3}
12	cyclic	23	2 (six cycles)	5×10^{-3}
14	cyclic	23	3 (six cycles)	5×10^{-3}
8	cyclic	23	5 (six cycles)	5×10^{-3}
3	cyclic	23	10 (six cycles)	5×10^{-3}
2	monotonic	23	-	5×10^{-4}
9	monotonic	23	-	200
7	monotonic	-80 °C	-	5×10^{-4}
16	monotonic	-40 °C	-	5×10^{-4}
1	monotonic	0 °C	-	5×10^{-4}
6	monotonic	100 °C	-	5×10^{-4}

3.3 Optical microscope (OM)

For observing the microstructure in OM, material was cut into small pieces and then molded in a cylindrical shape which was than followed by mechanical polishing to get a mirror like finish. Further it was then etched using suitable chemical so that the microstructure is visible in the microscope. The etchant used was Kallings No. 2 reagent's, Table 3.5 summarizes the chemical composition of it. Below Figure 3.5 shows the various machines used for sample preparation for optical microscope examination.

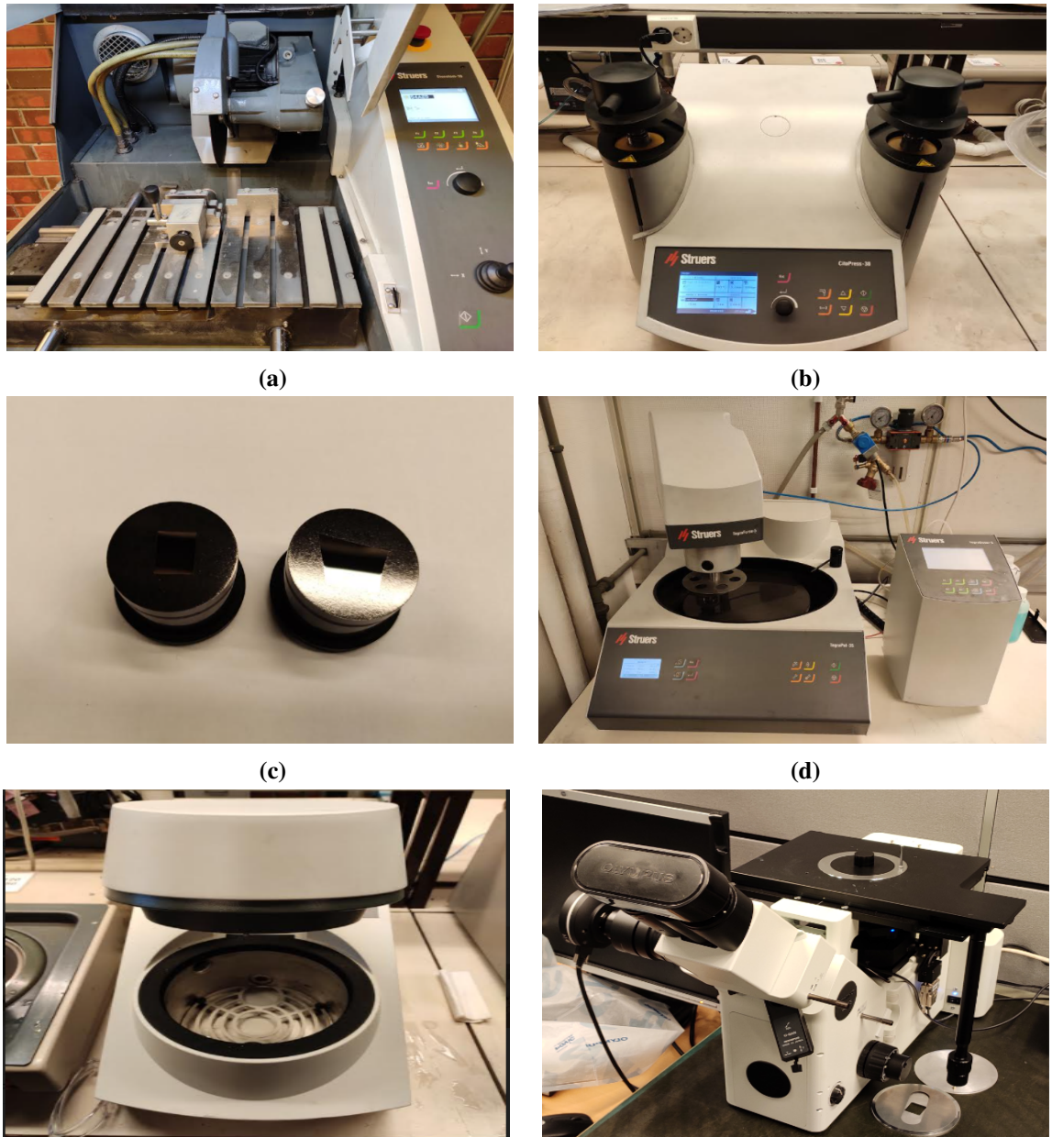

(a) **(b)** **(c)** **(d)** **(e)** **(f)**

Figure 3.5: *(a) Cutting machine used for small parts cutting, (b) Molding machine used for molding the small cutted part, (c) Specimen molded in polyfast resins in cylindrical shape, (d) Mechanical polishing machine used, (e) Ultrasonic cleaning machine used for cleaning the polished samples, (d) Optical microscope used for microstructure examination of samples.*

Below Table 3.5 briefly summarizes the polishing steps and parameters used. It can be seen from the below table that as we go towards the finer abrasive the polishing time is increased to get a perfect mirror like shine in the material. All the steps of material preparation (cutting and polishing) were performed independently. We were given prior training for the usage of equipment's.

Table 3.4: *Mechanical polishing steps and parameter used.*

Step	Abrasive	RPM	Load (N)	Applied time	Lubricant
1	220 grit Sic paper	330	40	2 minutes	water
2	600 grit Sic paper	330	40	2 minutes	water
3	1200 grit Sic paper	330	40	2 m 30 sec	water
4	9 µm	330	30	3 minutes	diamond suspension
5	3 µm	150	30	6 minutes	diamond suspension
6	1 µm	150	15	8 minutes	diamond suspension

Chemical Etching

Chemical etching is the most commonly used method for creating contrast in the specimen. In chemical etching electrolytic action takes place when a chemical solution (etchant) is in contact with a metal surface. The etchant, normally having a reduction component that is usually an acid, an oxidizer component, and a modifier component which causes an electric potential between differently oriented grains, different phases, grains and boundaries, inclusions, matrix, etc. The difference in attack, which is the amount of material removed from the single details, reveals the structure [63]. Below Table 3.5 shows the composition and concentration of etchant used for this work. The etchant was selected after studying the various literature related to this topic.

Table 3.5: *Chemical etchant used.*

Etchant	Composition	Conditions	Comments
Kalling's No.2	$CuCl_2$ (5 grams), HCL (100ml), C_2H_5OH ethanol (100ml)	Swab rubbing method used for approx. 1 minute 30 secs	Mostly attacks austenite and martensite

3.4 Transmission electron microscope (TEM)

Sample preparation

For TEM analysis (i.e. microstructure and diffraction pattern), thin foils were prepared, first by thinning down mechanically to a thickness of approx. 50-100 µm and then these foils were punched into a circular section of 3 mm in diameter using a special punching tool. The punched part was than electropolished to create a hole in the center by using a dual jet polishing system, Struers TENUPOL-5 operated at -30 °C and 15 V in an electrolyte solution of 95% methanol and 5% perchloric acid. A hole is created in the center to further achieve more thinning of specimen in the region from where we tend to take the diffraction pattern and image of the sample. Below Figure 3.6 shows TEM machine used for this work.

TEM analysis

Transmission Electron Microscopy (TEM) JEOL-2100 (LaB_6 filament), operating at 200kV, equipped with EDAX, high angle annular bright field and dark field detectors was used for the observation. Below Figure 3.6 represent the microscope used. Diffraction pattern was taken from a number of regions in the sample by tilting it at various angles.

Indexing of diffraction pattern

Diffraction pattern gives the information about the crystal structure in reciprocal space. Obtaining diffraction patterns from the region of interest and indexing them is an important step for analysis and interpretation of the region of interest in the material. Images were taken in three different modes which were diffraction mode, bright field image and dark field image.

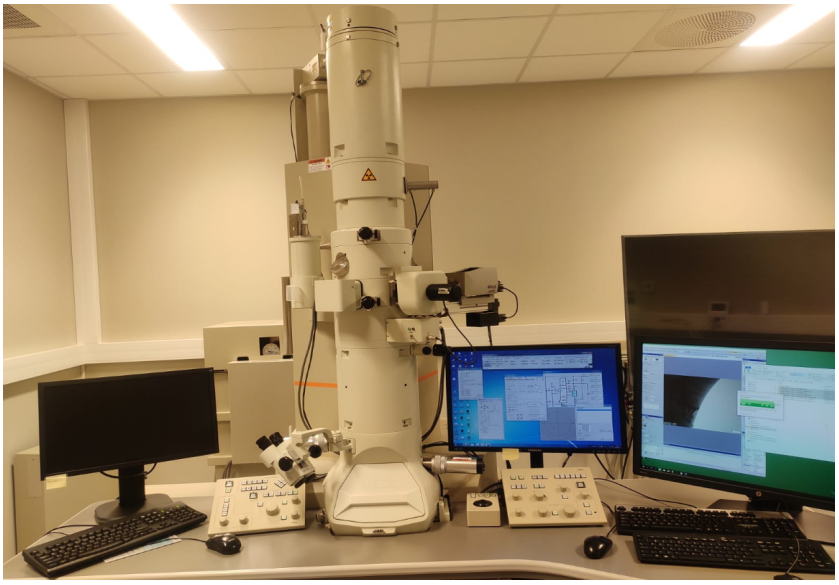

Figure 3.6: *TEM machine used to carry out experimental work.*

3.5 Scanning electron microscope (SEM)

The experimental part related to scanning electron microscope such as EBSD and ECCI were not performed because the machined was damaged and it could not be repaired within the time frame of master thesis due to COVID rules because the engineer had to travel from other country to fix it.

3.6 X-ray diffraction (XRD)

For XRD analysis flat polished samples were created to analysis it in the XRD machine. The samples were mechanically polished up to 1 µm finish. XRD patterns were acquired using bruker D8 diffractometer with CuK_{α} radiation ($\lambda = 1,54060$Å). Below Figure 3.7a shows the XRD machine used for the experimental work.

3.7 Ferritescope

Ferritescope is a non-destructive test which is mainly used to find ferrite or martensite content in the stainless steel and duplex steel. The basic working principle is according to the magnetic induction method. The magnetic components of the specimen interact with the magnetic field generated by the coil. A voltage proportionate to the ferrite concentration in a second coil is induced by variations in the magnetic field. This voltage is then evaluated and the amount of ferrite or martensite can be known. Below Figure 3.7b shows the apparatus of ferritescope used for the work. One major drawback of this equipment is that it cannot give accurate reading when the content of ferrite or martensite is in lower range (i.e. less than 1%).

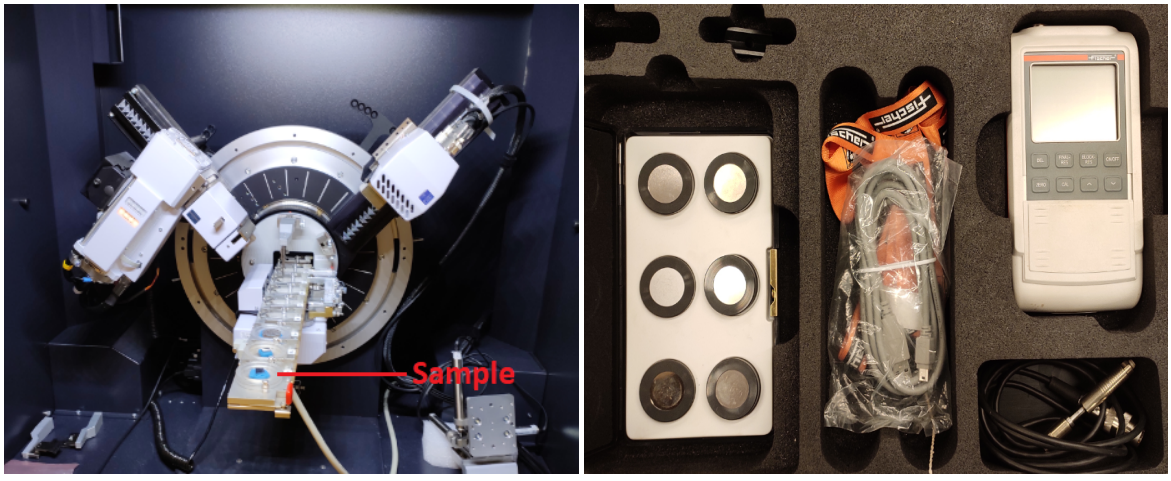

(a) **(b)**

Figure 3.7: *(a) Figure show test sample being hold inside XRD machine, (b) Ferritescope equipment.*

3.8 Hardness measurement

Hardness tests were performed using a Vickers Struers DuraScan testing machine using 5HV loads with a dwell time of 10 seconds. The measurement was taken along two cross sections, first along the plane parallel to tensile axis and another plane perpendicular to tensile axis. Readings obtained were calibrated manually to get more precise result by matching the lines to the corner of the indent shape obtained (see Fig. 3.9). Ten readings were taken for all the specimens and then an average hardness value was obtained for each specimen. The readings were taken from different regions in the sample to get uniformity in the results. Below Figure 3.8 shows the hardness machine used to carry out the experiment and Figure 3.9 shows the indentation mark after the application of the load.

Figure 3.8: *Struers Durascan Vickers hardness testing machine.*

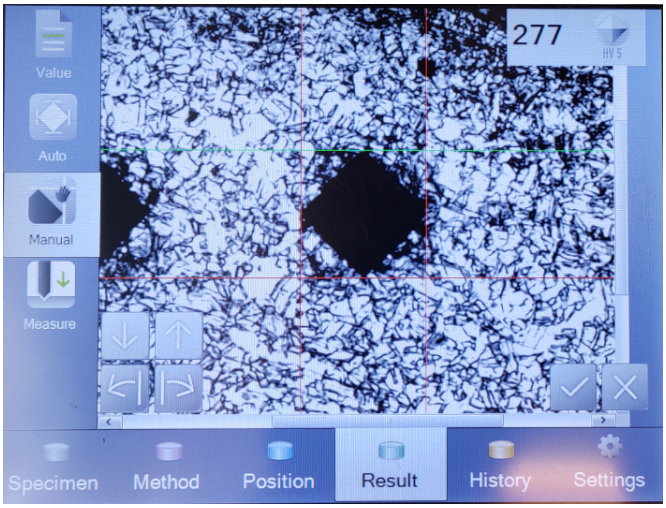

Figure 3.9: *Indentation created after the application of load, red and green lines were adjusted manually to get exact values.*

4 Results

4.1 Deformation of material

The test material was cyclically deformed and following below figures shows the graph obtained between strain amplitude and time. The strain rate value for the following method was kept 0.005 per seconds and the number of cycles used was six cycles. Figure 4.1 and 4.2 is for lower strain amplitude and Figure 4.3 is for higher strain amplitude.

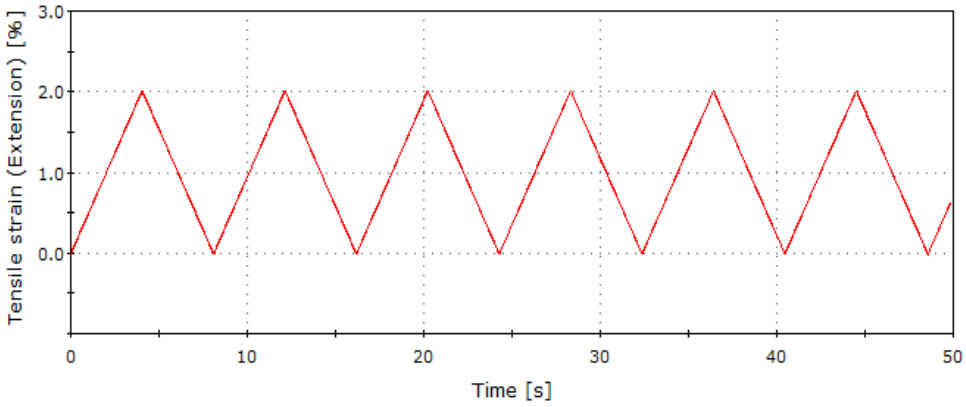

Figure 4.1: *Graph showing cyclically deformation of material at 1 percent strain amplitude.*

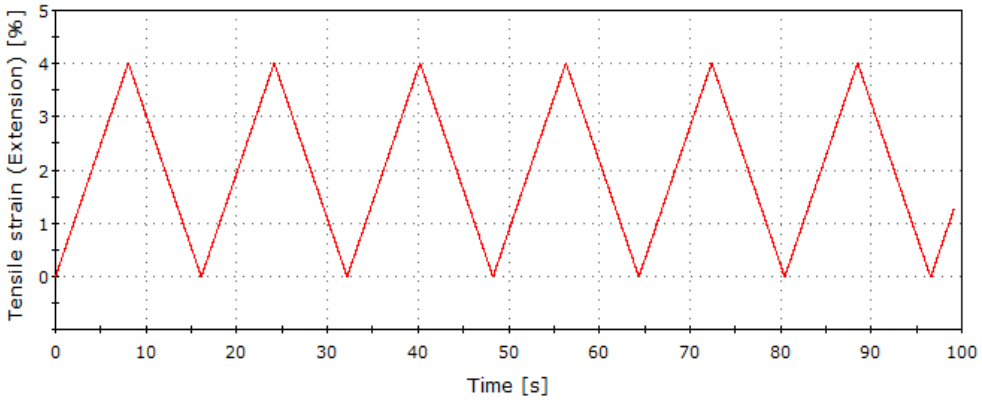

Figure 4.2: *Graph showing cyclically deformation of material at 2 percent strain amplitude.*

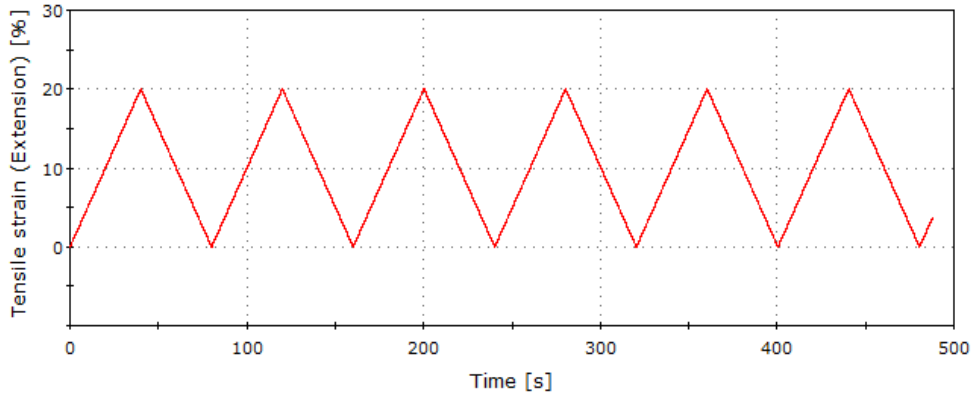

Figure 4.3: *Graph showing cyclically deformation of material at 10 percent strain amplitude.*

Some of the samples were strained until failure at a very slow strain rate (0.0005 per second) and at a very high strain rate (200 per second) to observe the properties and microstructural changes happening in it. It can be seen from the Figures 4.4 and 4.5 that tensile stress is increased as the strain rate value is increased due to the effect of work-hardening. These findings are consistent with the work done by authors [35]. It was also observed that a high amount of heat was generated when the material was strained at high strain rate as compared to low strain rate value.

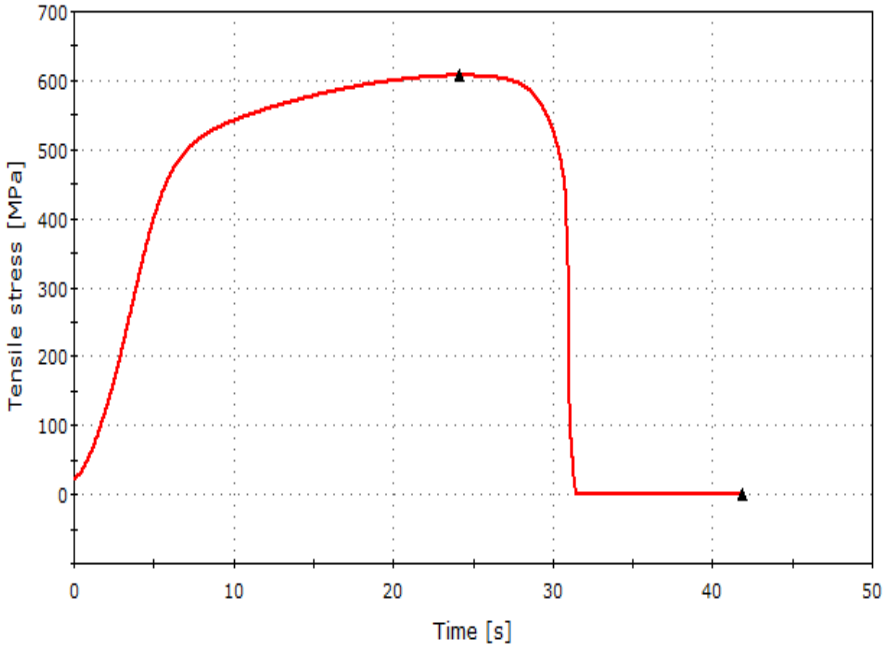

Figure 4.4: *Graph showing failure of the material at 0.0005 per second strain rate.*

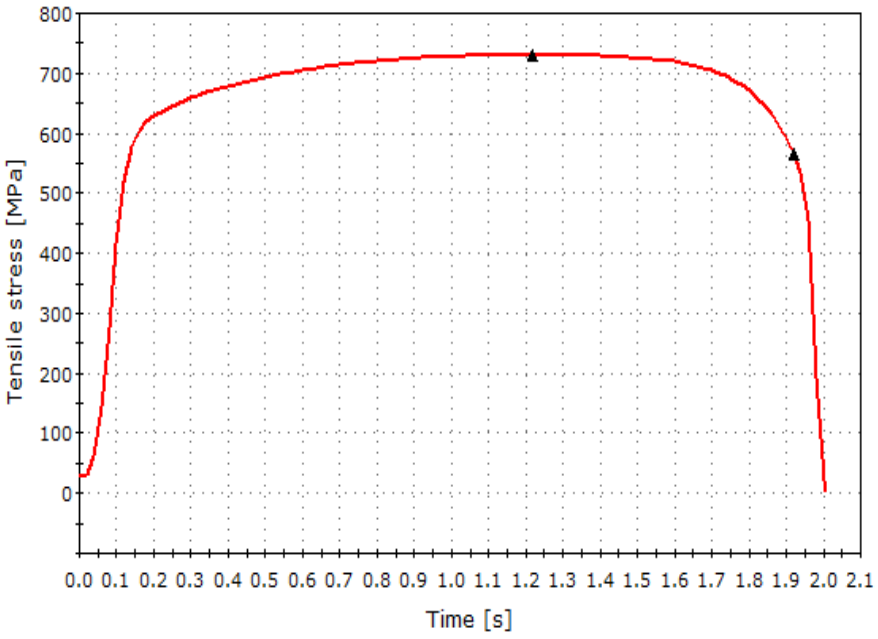

Figure 4.5: *Graph showing failure of the material at 200 per second strain rate.*

4.2 Optical microscope

Cyclically deformed specimens (six cycles) without failure

Below Figure 4.6 shows the image analysis obtained through the optical microscope. The images were taken at 50x magnification.

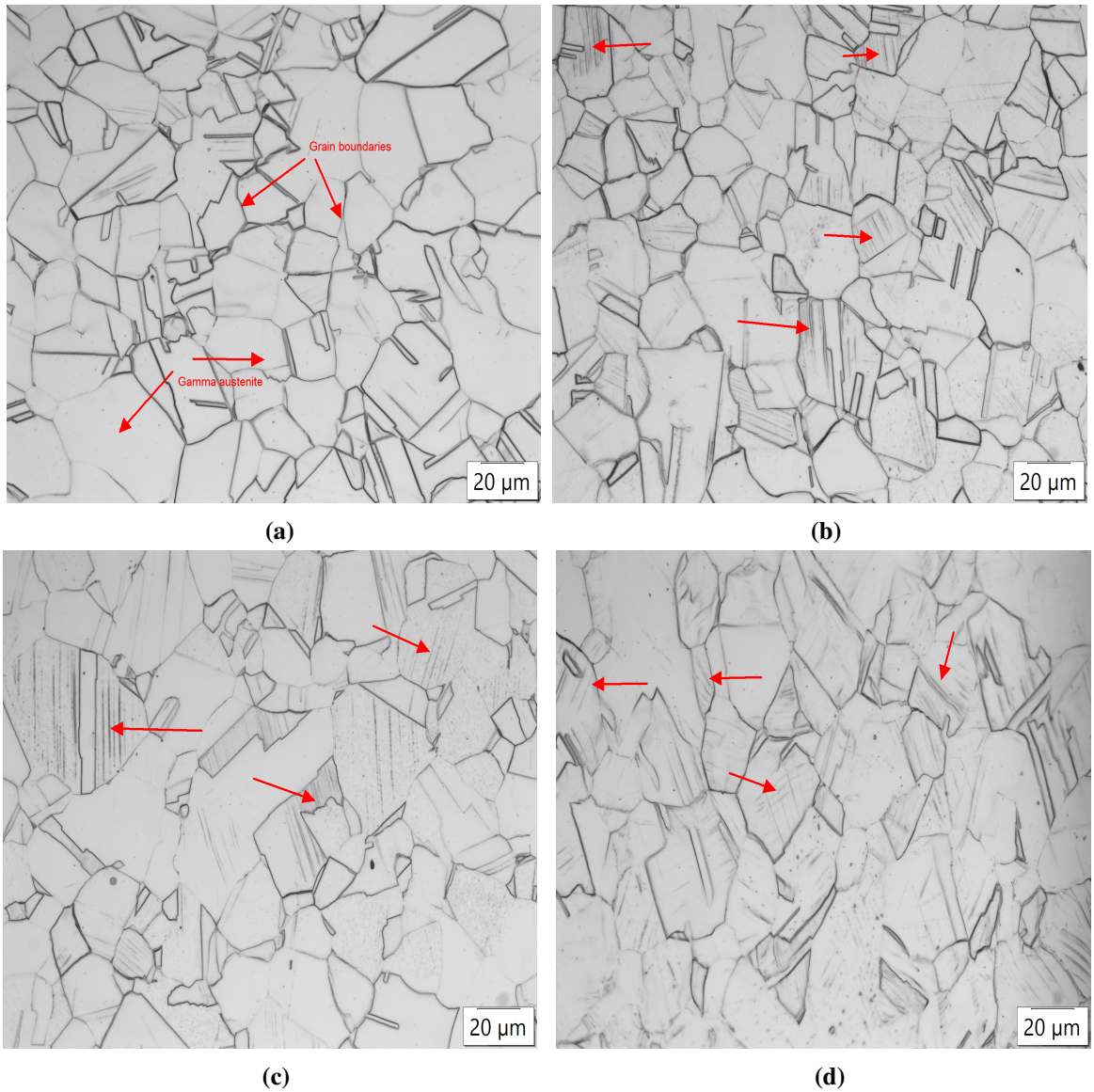

(a) **(b)**

(c) **(d)**

Figure 4.6: *(a) Microstructure of as received ASS material, (b) Microstructure of material after 1 percent strain amplitude deformation, (c) Microstructure of material after 2 percent strain amplitude deformation, (d) Microstructure of material after 10 percent strain amplitude deformation.*

From the above Figure 4.6 it can be clearly seen the grain boundaries of γ-austenite is intact in all the cases. There's no significant change in the grain structure and boundaries at lower values of deformation. The only change which was observed between the as received material and deformed material was that, number of scratches/needle shape structure (marked with red arrow) increases with increasing strain amplitude. This structures might be mechanical twin's or martensite, but it turns out to be twin's which was confirmed by other methods which is

discussed later in this chapter. This structures might have developed due to the twining or shear deformation of the material. Grain elongation can also be observed at higher strain amplitude values but the austenite structure is intact. Martensite presence was not observed in the above discussed cases and these results were supported by TEM analysis. So, it can be concluded that the austenite phase is stable according to OM image analysis and the findings complies with the work done by author [59].

Tensile failed specimens (straining of material until failure)

Following below figure shows the OM image analysis of tensile failed specimens. Figure 4.7a shows the microstructure of tensile failed specimen at a very slow strain rate (i.e. 0.0005 per second) and Figure 4.7b shows the microstructure of tensile failed specimen at -80 °C and 0.0005 per second strain rate.

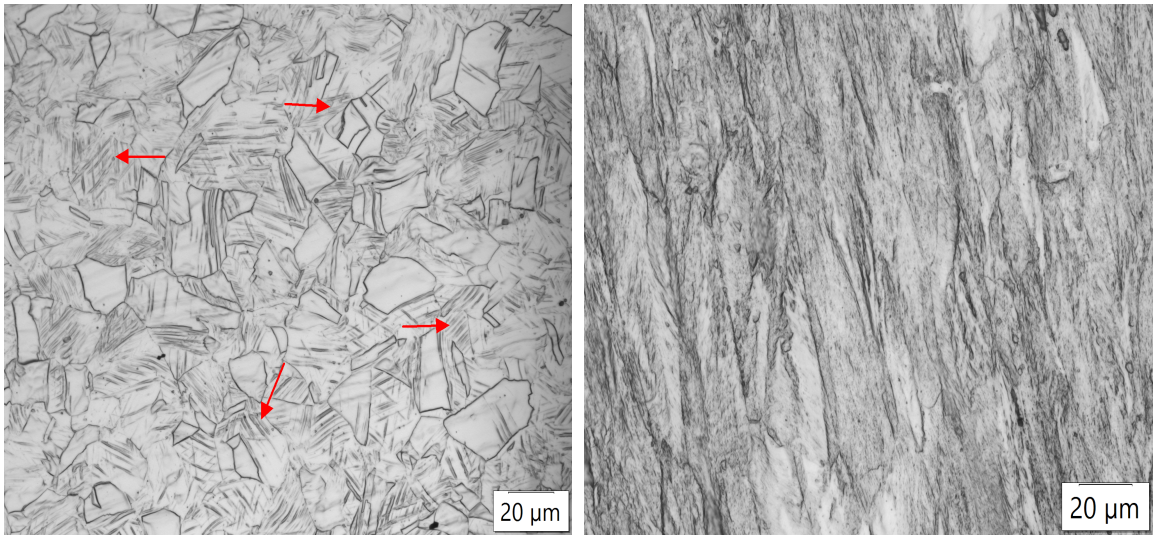

(a) **(b)**

Figure 4.7: *(a) Microstructure of tensile failed specimen at room temperature using strain rate of 0.0005 per second (specimen number 2, see Table3.3), (b) Microstructure of tensile failed specimen at -80 °C using strain rate of 0.0005 per second (specimen 7).*

When the specimen was strained to failure using slow strain rate (i.e.0.0005 per second), it is seen from Figure 4.7a that a lot of scratches morphology is been seen. This might be an indication that austenite phase is no more stable and some of its parts may have been induced to martensite this can be defended Since the etchant used mainly attacks the austenite and martensite structure and there's a lot change being seen through the image analysis. Tensile failed specimen at depressed temperature (Figure 4.7b), It can be clearly seen that there has been phase change or distortion of γ- austenite phase and martensite has been induced in this case. The findings were confirmed by using ferritescope and its shows the martensite percentage of approximately 21%. So, it can be concluded that martensite is induced in tensile failed specimen and the amount is increased as the temperature is lowered, this result is in accordance with Graph 2.19.

4.3 Transmission electron microscope (TEM)

Cyclically deformed specimens (six cycles) without failure

Below Figure shows the TEM image analysis of deformed sample. Images and diffraction patterns were taken from various regions. Some of the images and their diffraction pattern is shown below:

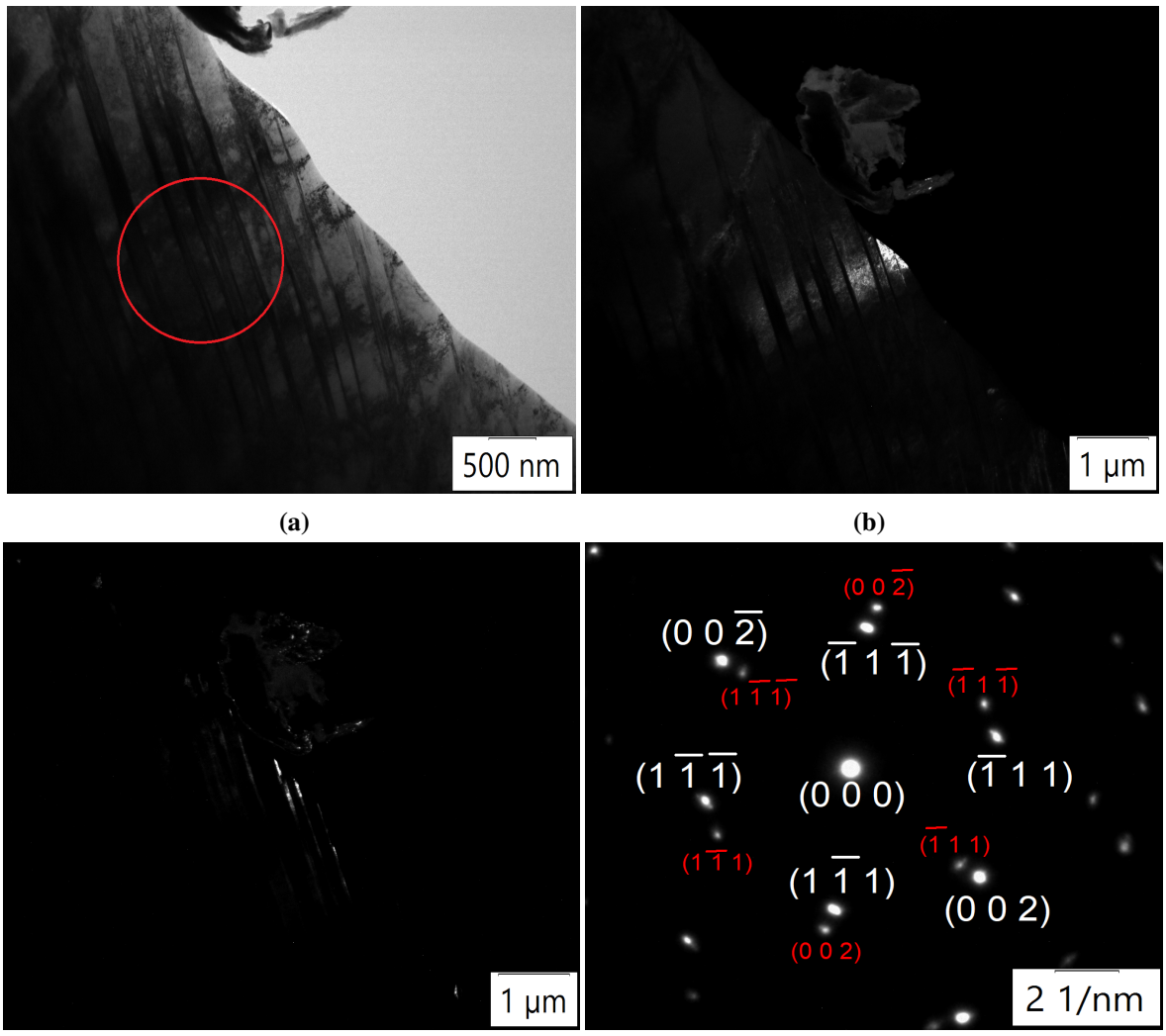

Figure 4.8: *Austenite matrix of material deformed at one percent strain amplitude (specimen no. 15), (a) Bright field (BF) image, (b) Dark field image from* $(\bar{1}1\bar{1})$ *reflection, (c) Dark field image from* $(00\bar{2})$ *reflection, (d) Selected area diffraction (SAD) pattern from region marked as red circle in (a) along* $[110]$ *zone axis.*

Needle/plates like structure were observed and the analysis of selected area diffraction (SAD) pattern (Figure 4.8d) reveals the presence of twin's structure which have fcc unit cell. The twins are of (111) type twining, often observed in fcc metals with the orientation relationship of $[\bar{1}10]_w // [1\bar{1}0]_s$. Subscript's 'w' and 's' indicate 'weak' and 'strong' spots, respectively. The lattice spacing are $d_{002} = 0.139$ nm and $d_{-11-1} = 0.160$ nm. The ratios of $(h^2+k^2+l^2)^{\frac{1}{2}}$ for (111 / 002) = 1.15. The camera length used was 300 mm and wavelength of radiation was 2.5079

pm(picometer). In Figure 4.8d white colour indexing of bright spots and red coloured indexing is for weaker spots. This kind of needle/plates structure was found in number of regions and they were analyzed, but all the structure seems to have a fcc unit cell structure. Observing a particular phase in TEM is quite challenging and it becomes more difficult if the phase amount is quite low in number.

Below are some more TEM analysis image at higher strain amplitude (10%) deformation. The suspected regions were examined:

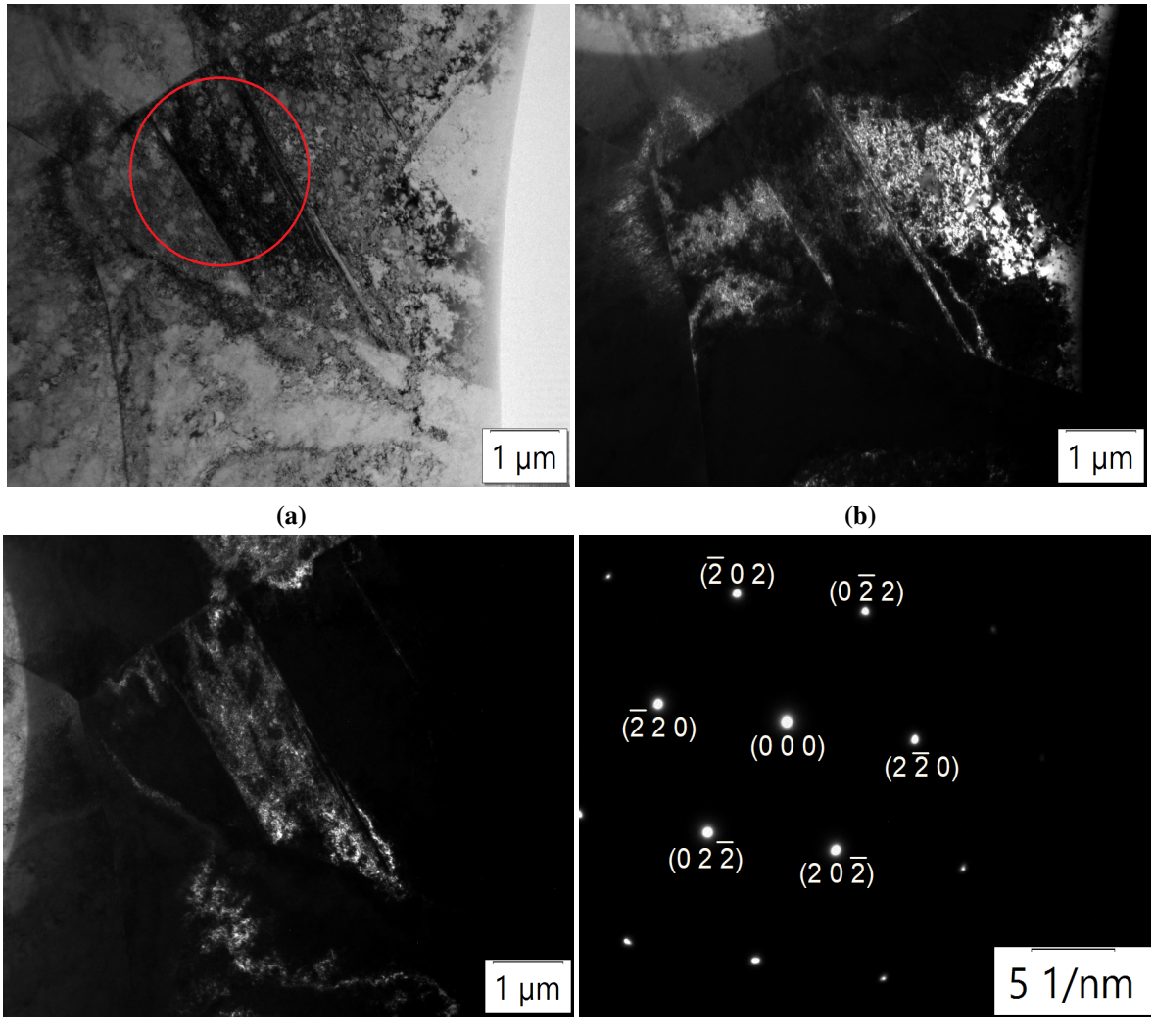

Figure 4.9: *Austenite matrix of material deformed at 10 percent strain amplitude (specimen no.3), (a) Bright field (BF) image, (b) Dark field image from* $(2\bar{2}0)$ *reflection, (c) Dark field image from* $(\bar{2}20)$ *reflection, (d) Selected area diffraction (SAD) pattern from region marked as red circle in (a) along* [111] *zone axis.*

The analyzed region (Figure 4.9) shows an austenite matrix and the SAD pattern reveals a fcc structure along the [111] zone axis. The lattice spacing along $d_{220} = 0.098$ nm.

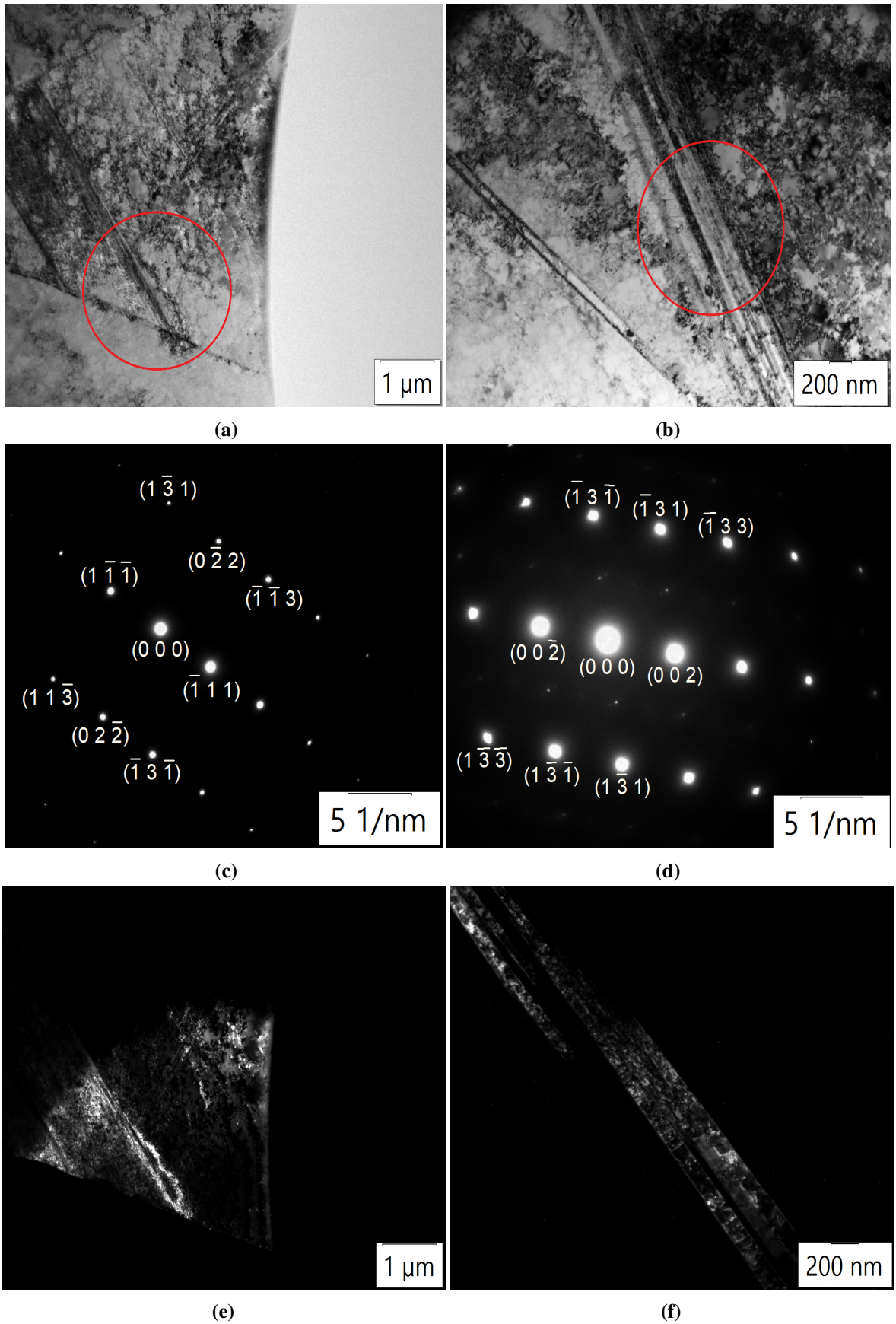

Figure 4.10: *Microstructure of austenite (γ) phase for material deforms at 10 percent strain amplitude (specimen no.3), (a) and (b) are TEM BF images from two different domain of interest, (c) and (d) are SAD pattern from marked regions along zone axis [211],[310] in (a) and (b) respectively, (e), (f) are dark field images from reflections of $(02\bar{2})$ in (c) and $(\bar{1}3\bar{1})$ in (d) respectively.*

From TEM analysis (Figures 4.8, 4.9 and 4.10) both image and selected area diffraction pattern reveals that under various deformed state of material (i.e. low and high strain amplitude) and using six strain cycle, strain induced martensite is not observed (TEM analysis), only we can see increase in twins through image analysis. All the diffraction pattern observed is of fcc structure. This finding is also supported by the XRD pattern observed and by ferritescope measurement. No peaks of martensite were seen through XRD analysis and no change of reading was seen in the ferritescope when compared with undeformed specimen.

Tensile failed specimens

Below (Figure 4.11) are the some of the images taken from the TEM. It is seen that a lot of needles and plate's structure is seen as compared to the deformed specimens.

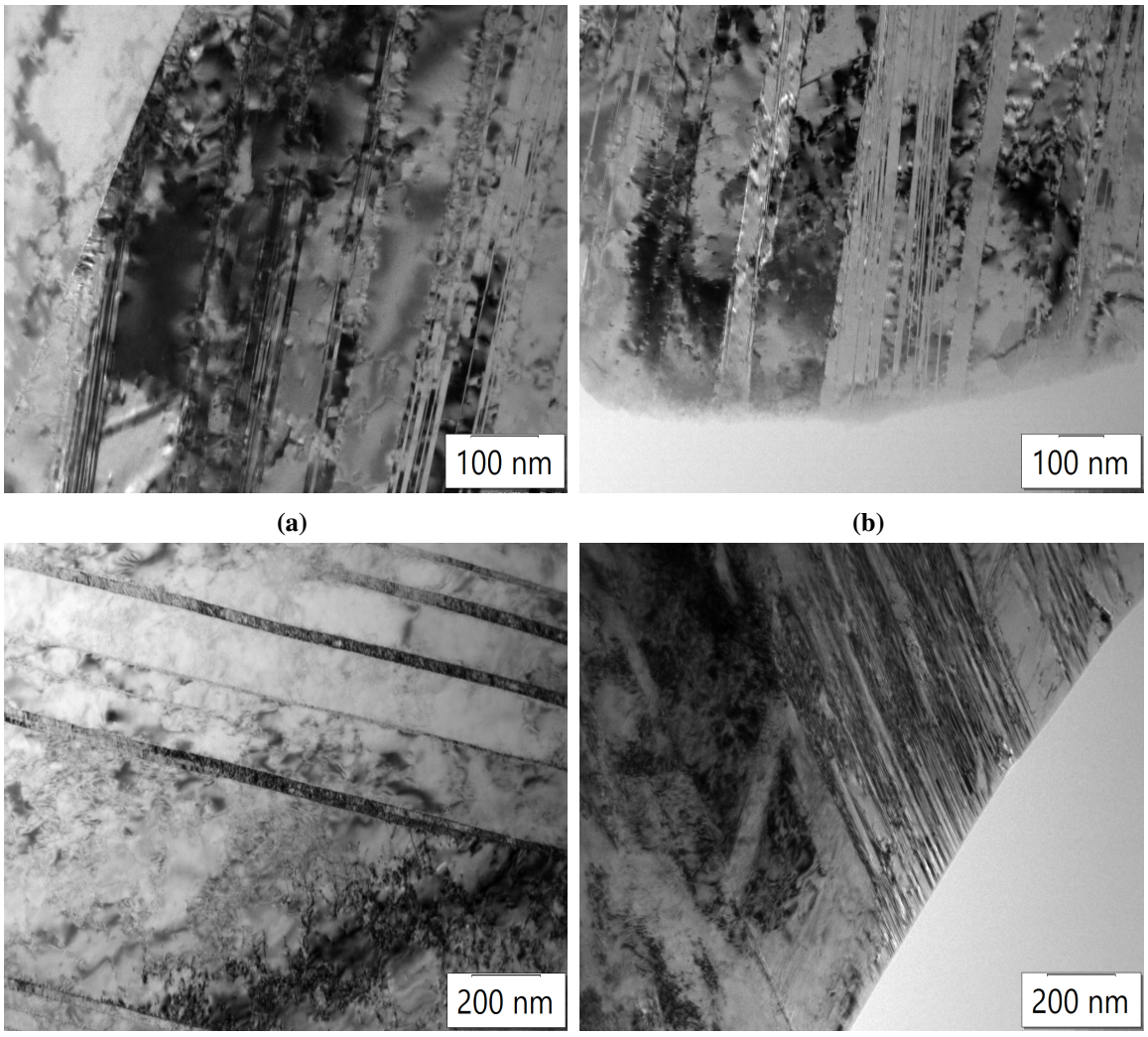

Figure 4.11: *(a), (b) shows the TEM microstructure image of tensile failed specimen at room temperature using 0.0005 per second (specimen no.2), (c) shows the image of tensile failed specimen at 100°C using 0.0005 per second strain rate (specimen no.6), (d) shows the image of tensile failed specimen at -80°C using 0.0005 strain rate (specimen no.7).*

Below Figure 4.12 shows some of the TEM images of tensile failed specimen at 0.0005 per second strain rate at room temperature. It includes diffraction pattern, bright field image and dark field image.

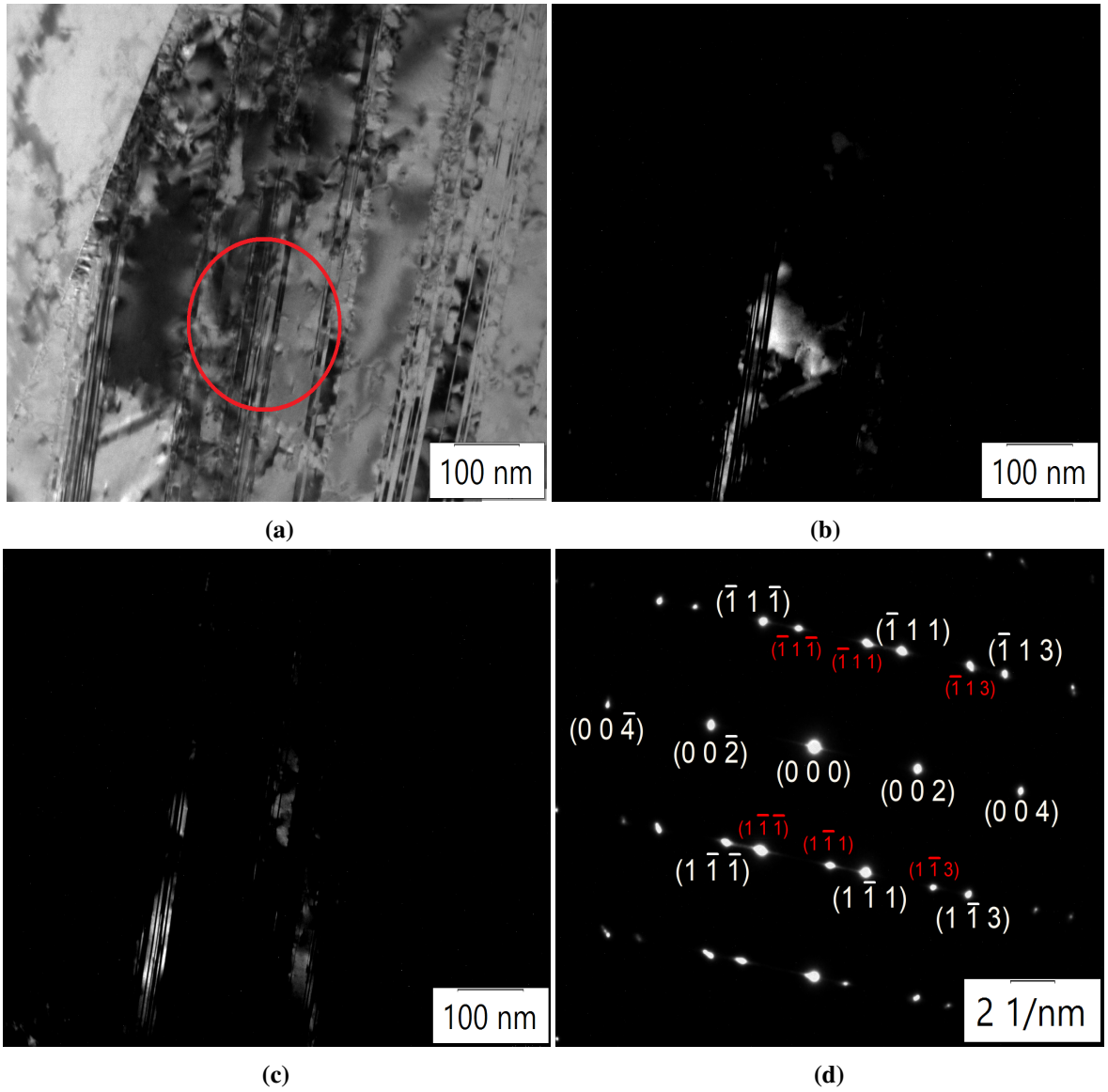

Figure 4.12: *Austenite matrix of material failed at room temperature using 0.0005 per second strain rate (specimen no.2), (a) Bright field (BF) image, (b) Dark field image reflection from* $(\bar{1}1\bar{1})$ *bigger spot, (c) Dark field image from* $(\bar{1}1\bar{1})$ *reflection (twins) marked with red color, (d) Selected area diffraction (SAD) pattern from region marked as red circle in (a) along [*$1\bar{1}0$*] zone axis.*

The SAD pattern (Figure 4.12d) shows that it is an austenite matrix along [110] zone axis. The inspected area turns out to be mechanical twin's were red coloured is indexing from twins reflection. The lattice spacing is $d_{002} = 0.158$ nm and along $d_{-11-1} = 0.137$ nm. Ratios of $(h^2 + k^2 + l^2)^{\frac{1}{2}}$ for (200/111) = 1.15. Camera length used was 300mm and wavelength of the radiation was 2,5079 pm.

Below Figure 4.13 depicts some more TEM images analysis of tensile failed specimen at 0.0005 per second strain rate. The diffraction pattern was taken from the region which shows a change in the morphology.

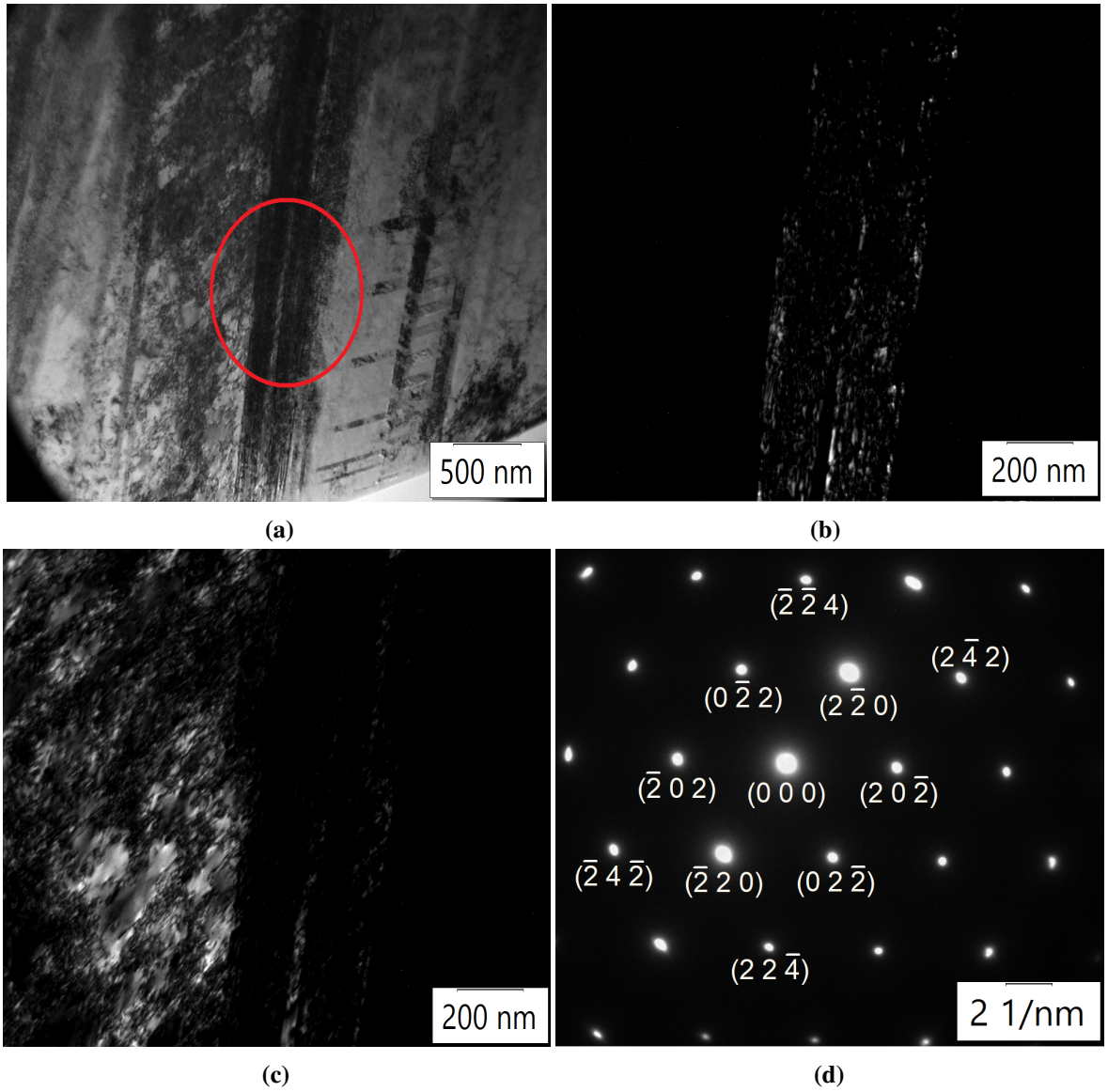

Figure 4.13: *Austenite matrix of material failed at room temperature using 0.0005 per second strain rate (specimen no.2), (a) Bright field (BF) image, (b) Dark field image reflection from (0$\bar{2}$2), (c) Dark field image from (2$\bar{2}$0) reflection, (d) Selected area diffraction (SAD) pattern from region marked as red circle in (a) along [111] zone axis.*

The SAD pattern (Figure 4.13d) reveals that the examined area has austenite matrix along [111] zone axis. The lattice spacing are $d_{2-20} = 0.161$ nm, $d_{0-22} = 0.170$ nm and $d_{2-42} = 0.09$ nm. Ratios of $(h^2 + k^2 + l^2)^{\frac{1}{2}}$ for (0 -2 2/2-2 0) = 1.05 and for (0 -2 2/-2-2 4) = 1.77. Camera length used was 300 mm and wavelength of the radiation was 2,5079 pm. The camera length and wavelength of radiation as same for all diffraction pattern observed.

Below Figure 4.14 shows some more TEM analysis of needles and plate like structure induced in the material.

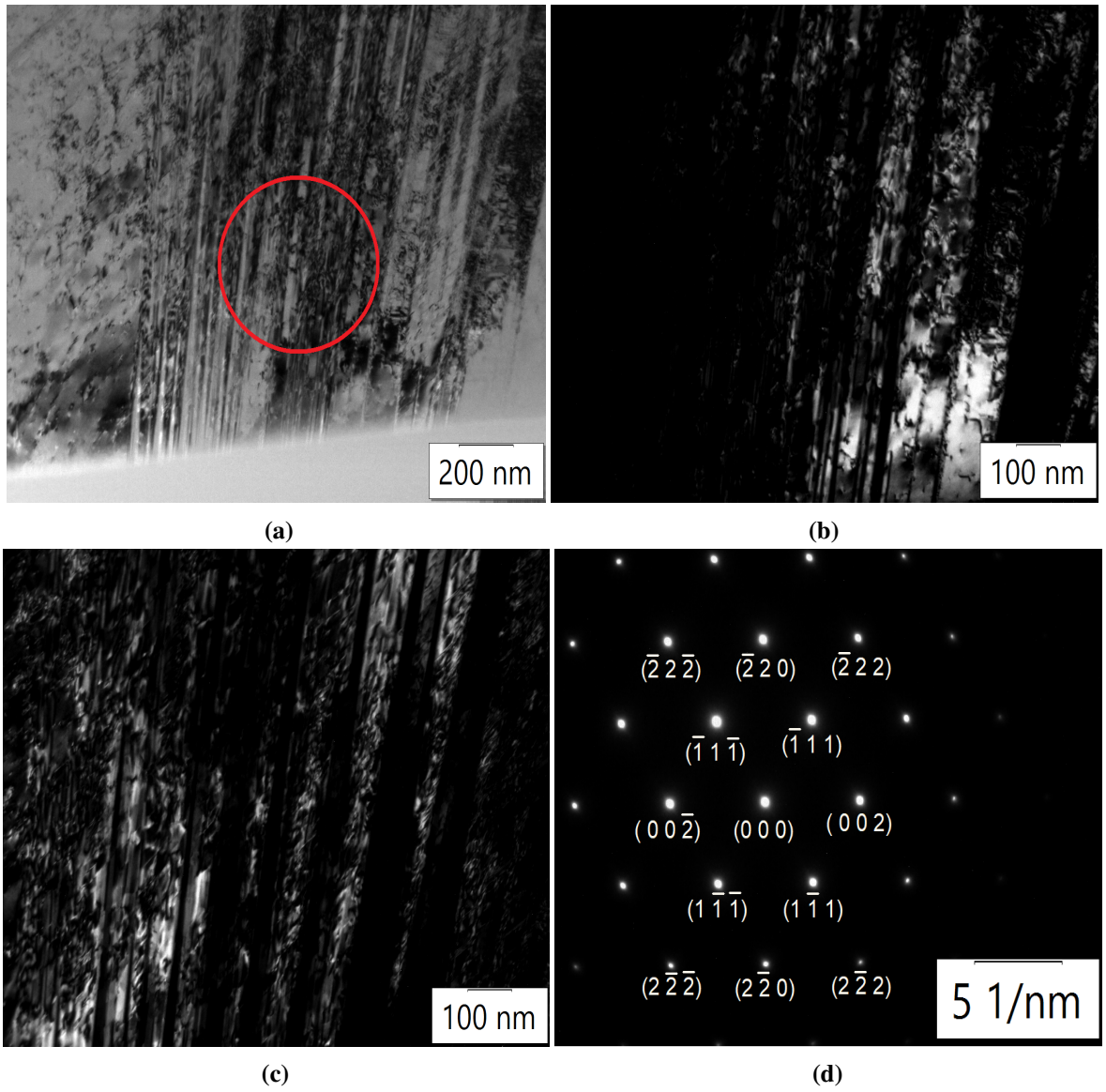

Figure 4.14: *Austenite matrix of material failed at room temperature using 0.0005 per second strain rate (specimen no.2), (a) Bright field (BF) image, (b) Dark field image reflection from* $(\bar{1}1\bar{1})$*, (c) Dark field image from* $(\bar{1}11)$ *reflection, (d) Selected area diffraction (SAD) pattern from region marked as red circle in (a) along [*$1\bar{1}0$*] zone axis.*

The SAD pattern (Figure 4.14d) reveals that the examined area has austenite (fcc structure) matrix along [110] zone axis. The lattice spacing are $d_{002} = 0.138$ nm, $d_{-111} = 0.160$ nm, and $d_{-220} = 0.097$ nm. The ratio of $(h^2 + k^2 + l^2)^{\frac{1}{2}}$ for (0 0 2/-2 2 0) = 1.42 and for (-1 1 1/0 0 2) = 1.15. The observed diffraction pattern is confirmed by measuring the angle theoretically (using the formula) and by analyzing the angle using software. Observed pattern was also verified by taking ratios for lattice spacing.

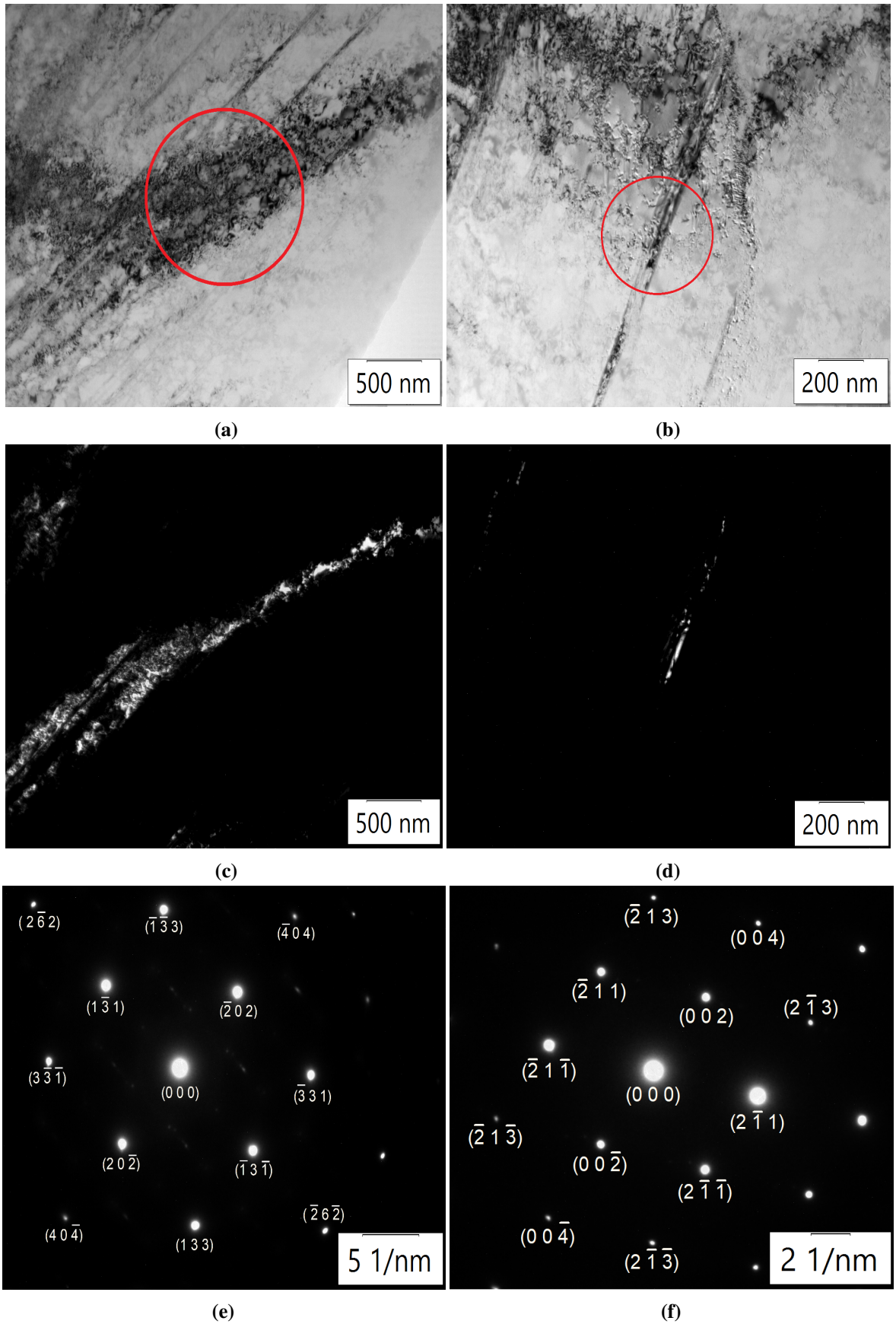

Figure 4.15: *TEM image analysis of material failed at room temperature using 200 per second strain rate (high strain rate, specimen no.9), (a) and (b) are TEM BF images from two different domain of interest, (c) and (d) are SAD pattern from marked regions along zone axis [323], [120] in (a) and (b) respectively, (e), (f) are dark field images from reflections of* (002) *in (c) and* $(3\bar{3}\bar{1})$ *in (d) respectively.*

From the above Figure 4.15 analysis it is see that Fig. 4.15e represents an austenite matrix (fcc) along zone axis [323] where the lattice spacing are $d_{-13-1} = 0.084$ nm, $d_{-202} = 0.100$ nm and $d_{3-3-1} = 0.064$ nm. The ratio of $(h^2 + k^2 + l^2)^{\frac{1}{2}}$ for (202 / 131) = 1.190, (202 / 331) = 1.56 and (131 / 331) = 1.31. From Fig. 4.15f analysis the matrix turns out to be of bcc along [120] zone axis where the lattice spacing are $d_{002} = 0.170$ nm, $d_{-211} = 0.139$ nm and $d_{2-13} = 0.090$ nm. The ratio of $(h^2 + k^2 + l^2)^{\frac{1}{2}}$ for (002 / 211) = 1.22, (211 / 213) = 1.54 and (002 / 213) = 1.88. Although α'-martensite also possess bcc structure but this diffraction pattern is not for α'-martensite because the SAD pattern has been taken from a region which contains both needle like structure and other region due to that the diffraction pattern cannot be so perfect (i.e. it might have some other weak spots nearby which would represent fcc because the maximum matrix is of fcc) so the diffraction pattern turns out to be for ferrite (which also has b.c.c structure) because ASS contains some percentage of ferrite.

Below Figure 4.16 shows tensile failed specimen at 100 °C using 0.0005 per second strain rate. Through TEM image analysis of the material, it is seen that very few needles and plate like structures was observed (only one picture has been used here for reference) because with increase in temperature the stacking fault energy of a material decreases and hence tendency to form martensite is reduced.

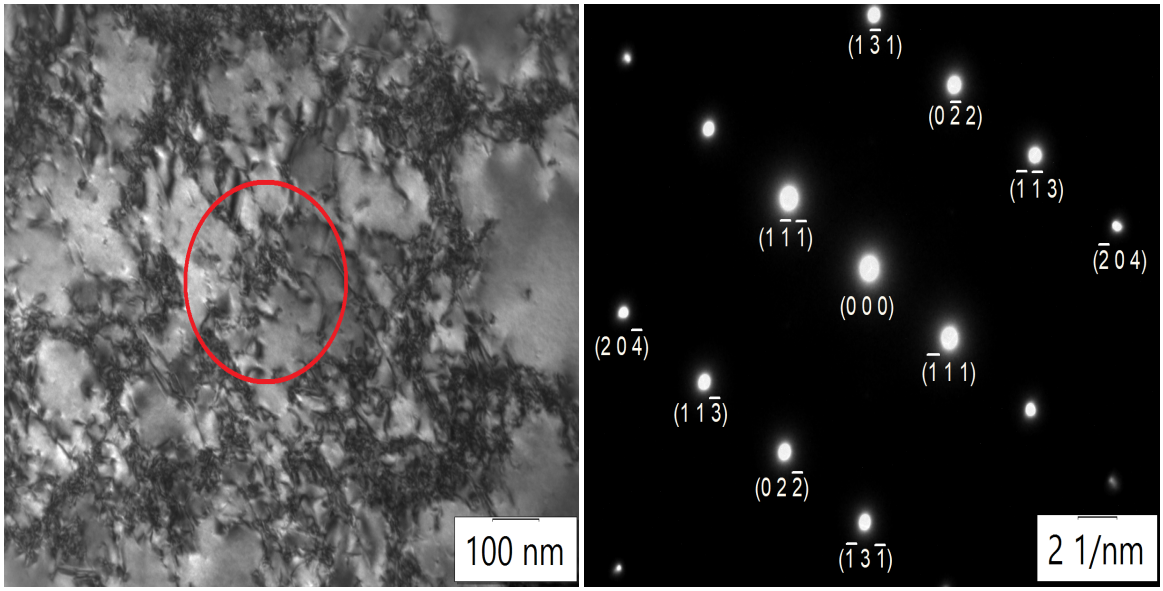

(a) **(b)**

Figure 4.16: *(a) TEM image of tensile failed specimen at 100°C using 0.0005 per second strain rate (specimen no.6), (b) SAD pattern from image (a) along zone axis [211].*

Above analysis of Figure 4.16 shows an austenite matrix diffraction pattern along zone axis [211], where lattice spacing are $d_{-111} = 0.159$ nm, $d_{0-22} = 0.098$ nm and $d_{-13-1} = 0.082$ nm. The ratios of $(h^2 + k^2 + l^2)^{\frac{1}{2}}$ for (111 / 022) = 1.62, (022 / 131) = 1.19 and (111 / 131) = 1.93.

Below Figure 4.17 shows tensile failed specimen at -80°C using 0.0005 per second strain rate.

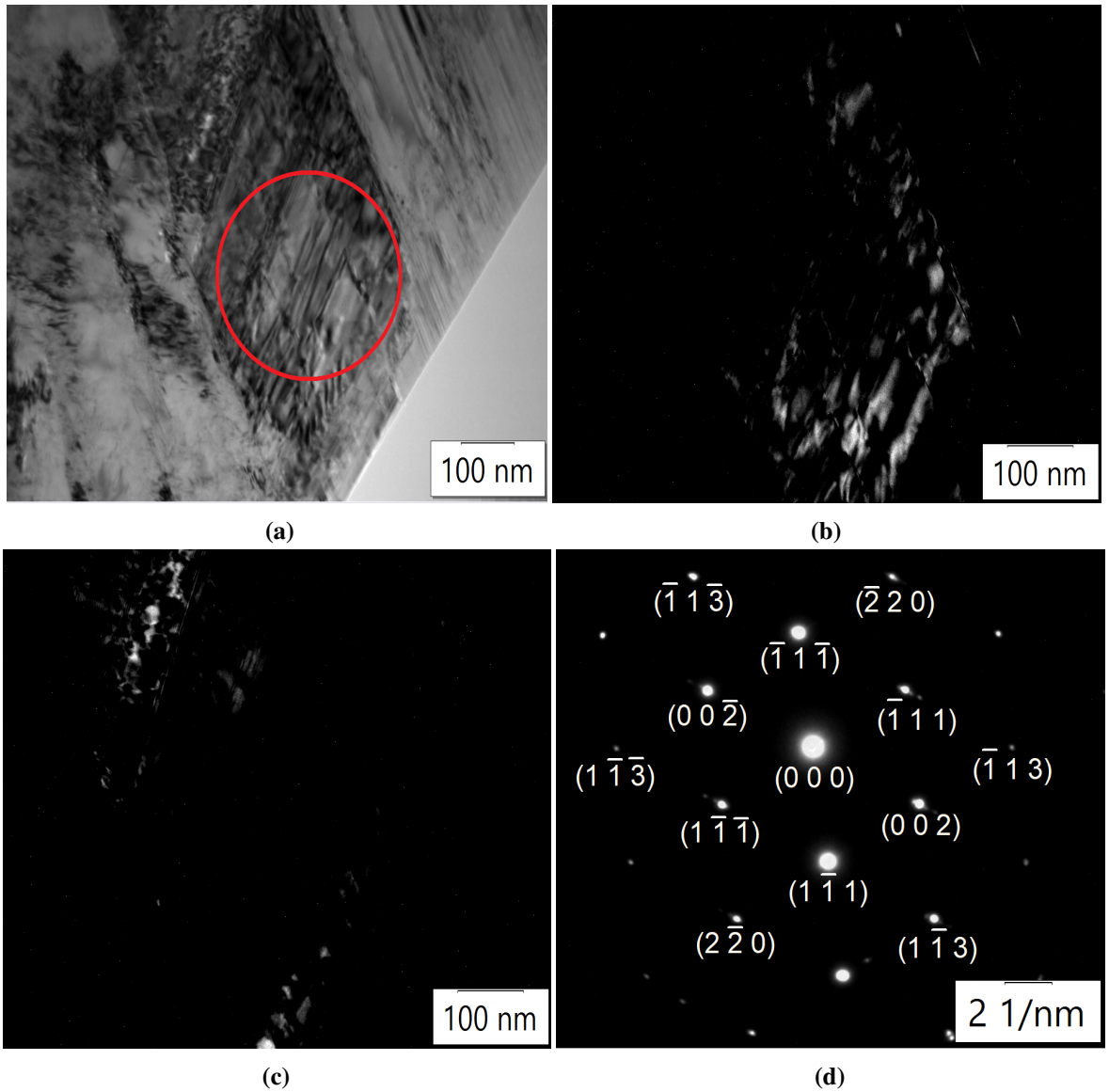

(a) **(b)**

(c) **(d)**

Figure 4.17: *Austenite matrix of material failed at -80°C using 0.0005 per second strain rate (specimen no.7), (a) Bright field (BF) image, (b) Dark field image reflection from* $(1\bar{1}1)$*, (c) Dark field image from* $(00\bar{2})$ *reflection, (d) Selected area diffraction (SAD) pattern from region marked as red circle in (a) along* $[110]$ *zone axis.*

TEM analysis of above Fig. 4.17 reveals a fcc matrix along the zone axis [110], where the lattice spacing are $d_{002} = 0.149$ nm, $d_{-11-1} = 0.161$ nm, $d_{-220} = 0.098$ nm and $d_{113} = 0.090$ nm. The ratios of $(h^2 + k^2 + l^2)^{\frac{1}{2}}$ for (111 / 002) = 1.08, (002 / 220) = 1.52 and (111 / 113) = 1.77. In this case of failure, the chance of induced martensite formation is very high (can also be verified by the Graph 2.19) because as the temperature is decreased the stacking fault energy is decreased and hence the formation of martensite also increases. This finding is in like nature with the work done by author [35].

4.4 Hardness Test

Below Graph 4.18 shows the variation of Vickers hardness value from minimum to maximum of a particular specimen deformed at specific test condition. The mean hardness values of all the different samples are connected by the shown line. The readings were taken along perpendicular to the tensile axis direction and ten readings were taken for each specimen at different points in the samples. The load used for testing was HV5 and the dwell time was 10 seconds.

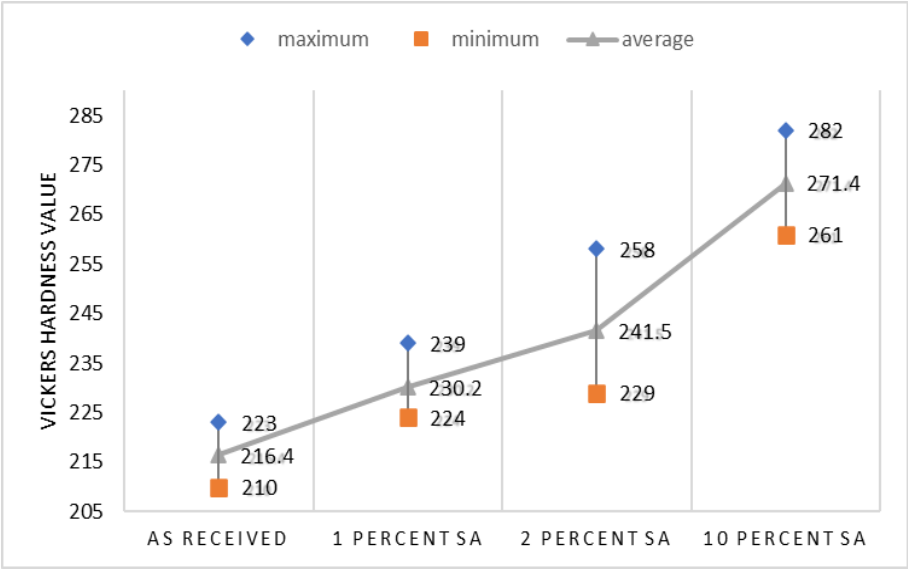

Figure 4.18: *Graph showing hardness value for as received sample, sample deformed at 1 percent strain amplitude (SA), 2 percent SA and 10 percent SA along perpendicular to tensile axis direction.*

Undeformed ASS has a Vickers hardness value of around 218 and from above Graph 4.18 the result is nearby to that value. It can be seen from the Graph 4.18 that as the deformation is increased the hardness value also increases. The increase in hardness value with deformation is attributed to more stacking faults and formation of greater number of twin's with increasing deformation. Also, from microstructure obtained through optical microscope it is seen that austenite grain size is increased as we increase the strain amplitude and due to that stacking fault energy is reduced and more twins formation occurs which results in the hardening of the material. The results are in like nature with work done by author [71].

Graph 4.19 below shows the Vickers hardness value of the same specimen under same test condition as shown in 4.18 but the measurement direction is along the tensile axis direction. If compared with Graph 4.18 the hardness value (as shown in Graph 4.19) under all test condition is lower, this lower in hardness value may be attributed due to the direction of production of the ASS because the material used for this work was a plate of 3mm thickness which is bent and hot rolled inside of the carbon steel pipe.

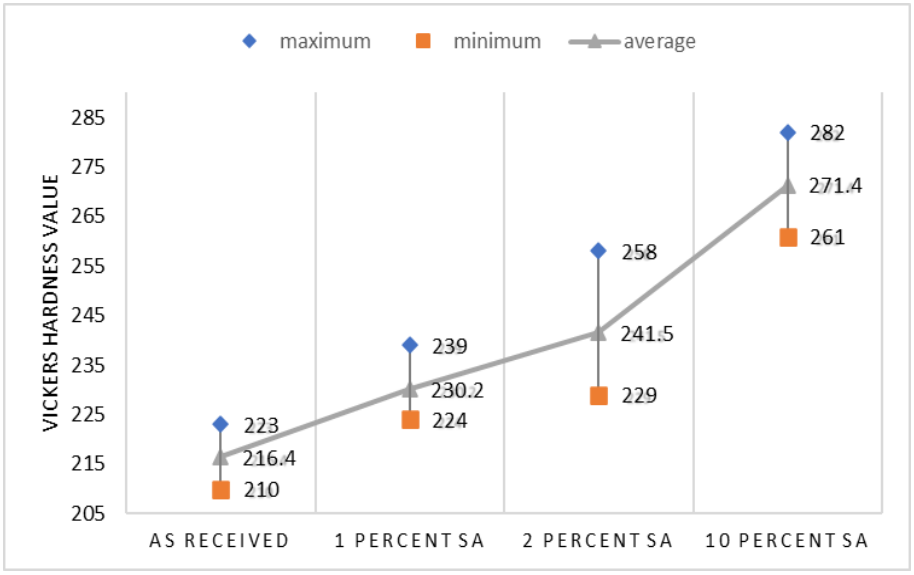

Figure 4.19: *Graph showing hardness value for as received sample, sample deformed at 1 percent strain amplitude (SA), 2 percent SA and 10 percent SA along tensile axis direction.*

Below Graph 4.20 shows the Vickers hardness value of tensile failed specimen at lower (i.e. 0.0005 per second) and higher (i.e. 200 per second) strain rate (SR). Ten readings were taken for each specimen at different points and the measurement direction was along perpendicular to the tensile axis. The load used for testing was HV5 and the dwell time was 10 seconds.

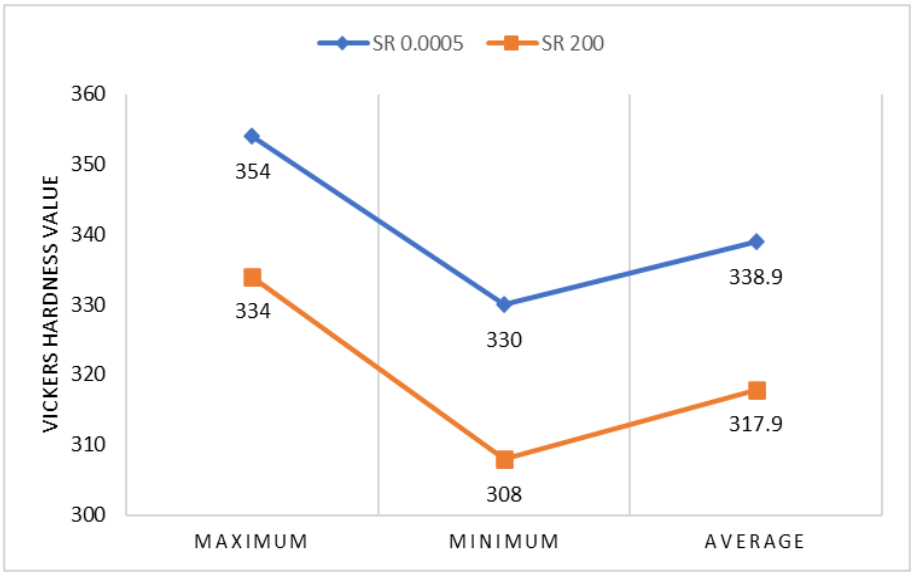

Figure 4.20: *Graph showing hardness value for tensile failed specimen at lower strain rate (SR) i.e. 0.0005 per second and higher SR i.e. 200 per second along the direction perpendicular to the tensile axis direction.*

It can be seen from the above Graph 4.20 that the tensile failed specimen has higher hardness value as compared to deformed specimen (both at low and high strain amplitude). This increases in hardness value can be attributed to the formation of α-martensite and twins generated. It can also be seen that the material failed at high strain rate (i.e. 200 per second) has lower hardness

value as compared to material failed at lower strain rate (i.e. 0.0005 per second) because the tendency to form martensite is reduced as the strain rate value is increased. The results obtained are in like nature with work done by authors [35, 71].

Below Graph 4.21 shows the hardness value of tensile failed specimen along tensile axis direction.

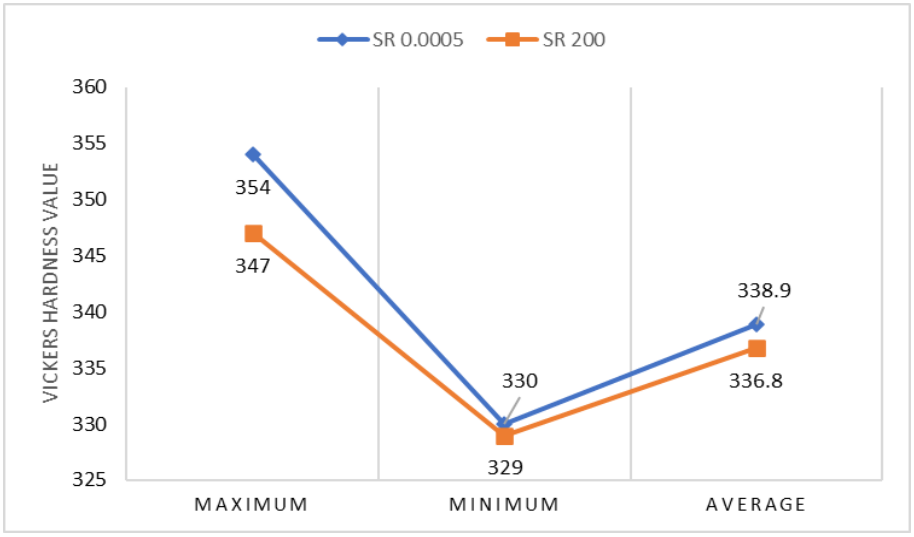

Figure 4.21: *Graph showing hardness value for tensile failed specimen at lower strain rate (SR) i.e. 0.0005 per second and higher SR i.e. 200 per second along the tensile axis direction.*

Below Graph 4.22 shows the hardness value of tensile failed specimen at -80°C, -40°C and 0 °C using 0.0005 per second strain rate. Ten readings were taken for each specimen at different points and the measurement direction was along perpendicular to the tensile axis. The load used for testing was HV5 and the dwell time was 10 seconds.

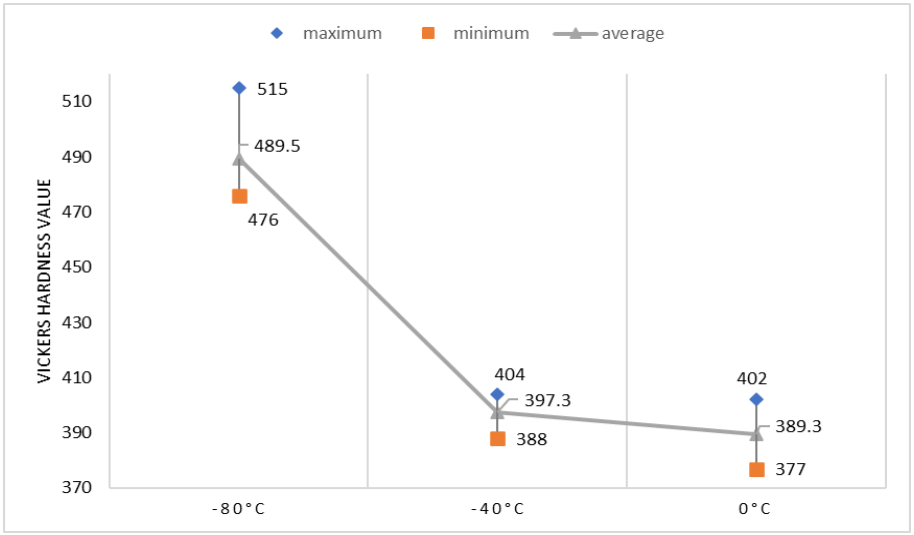

Figure 4.22: *Graph showing hardness value for tensile failed specimen at -80°C, -40°C and 0 °C using 0.0005 per second strain rate along perpendicular direction to tensile axis.*

Below Graph 4.23 shows the hardness value of same specimens and under same test

condition as shown in Graph 4.22, but the only difference is the hardness measurement direction which in this case is along the tensile axis direction.

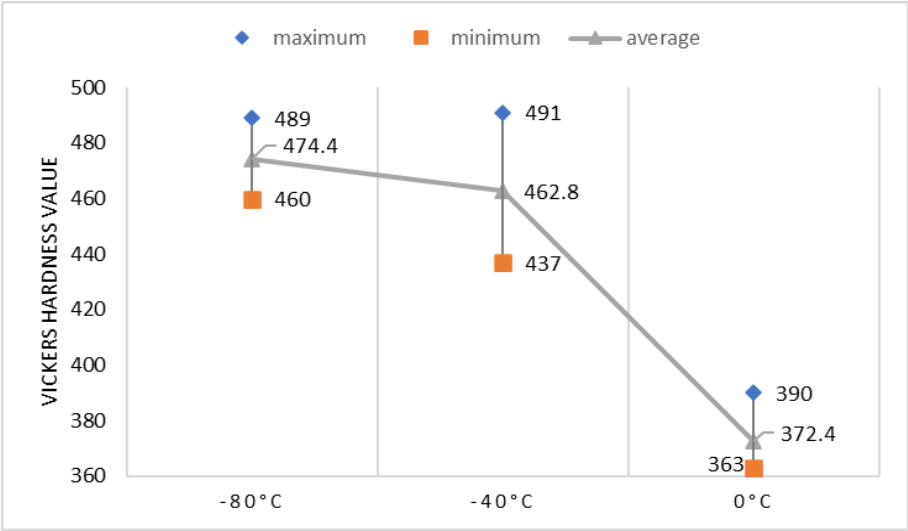

Figure 4.23: *Graph showing hardness value for tensile failed specimen at -80°C, -40°C and 0 °C using 0.0005 per second strain rate along tensile axis direction.*

It can be seen from all above graphs that the hardness value obtained is maximum when the material is failed at depressed temperature (-80°C). This increase in hardness is due to the formation of martensite Maximum amount of martensite is formed when the material is deformed at depressed temperature because the stacking fault energy of material is increased and shear bands acts as the nucleation site for the formation of martensite. The given reason complies with Graph 2.19 and the work done by author [35]. So, the formation of martensite in tensile failed specimens can also be co-related easily with the increase in the hardness value of the material.

4.5 Ferritescope

Ferritescope readings were taken for all the deformed specimen but none of the deformed material showed any amount of martensite content expect for the material failed at -80°C (See Figure A.1 in appendix for further reference). Other tensile failed samples did not show any martensite reading in ferritescope and this may be due to low amount of induced martensite present in those material. The big drawback with ferritescope is that it is not suited to measure the low amount of ferrite/martensite in a given material.

4.6 X-ray diffraction (XRD)

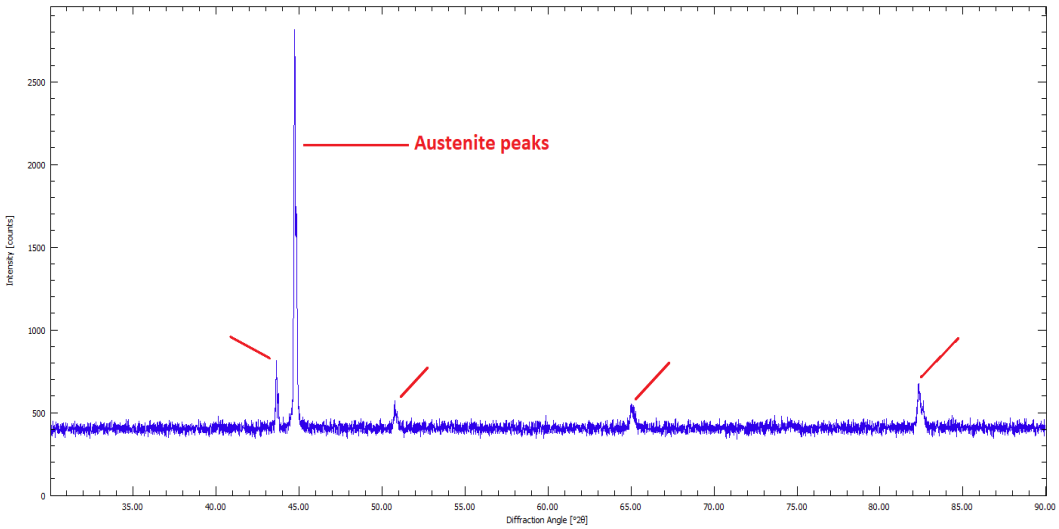

Figure 4.24: *XRD peaks for cyclically deformed specimen at higher strain amplitude (i.e. 10 percent).*

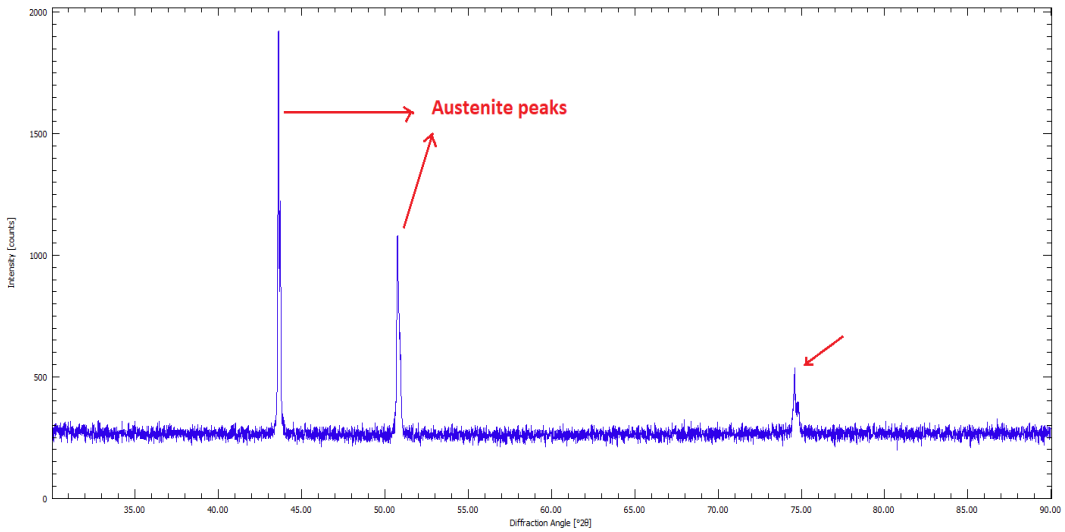

Figure 4.25: *XRD peaks for tensile failed specimen using 0.0005 per second strain rate.*

Above Figure 4.24 and 4.25 shows the XRD peaks for cyclically deformed and tensile failed specimen respectively. The peaks obtained was just of austenite phase when compared with the data stored for this material in the software. The sample used for XRD was solid steel specimen. No martensite peaks were observed in tensile failed specimen and this may be due to low percentage of martensite induced in the specimen.

5 Discussion

In this section author discusses the work done and findings related to it:

- Observation of microstructure for cyclically deformed specimen at low and high strain amplitude using optical microscope reveals the stability of austenite, this result is in like nature with work done in literature [59]. The minor changes which were seen when compared with undeformed specimen, is that there were some scratches/needle shaped structure which was later confirmed as mechanical twin's by the help of TEM analysis. Also, there was some changes in the hardness value of the deformed specimen and this change was attributed to increase in shear faults and mechanical twin's structure. Although it is difficult to rely on XRD result for solid material examination but the peaks obtained through XRD was just peaks for austenite phase and no other phase peak was seen. TEM analysis (i.e. diffraction pattern) reveals only the twin's structure and austenite structure along various zone axis. The material under examination was tilted under various angles and from different points the diffraction patterns were taken.

- Observation of microstructure for tensile failed specimen at room temperature using low strain rate (i.e. 0.0005 per second) and high strain rate (i.e. 200 per second) was examined in this work. Optical microscope image reveals that the austenite grain structure was not stable meaning that a lot of scratches/needle shaped structure was seen and this might be the induced martensite which are in like nature with the work done in literature [35, 51]. This result was not confirmed with TEM and XRD because the induced martensite may be very small in number and it was very difficult to find any bcc or hcp structure from diffraction pattern by TEM analysis, since the examined area in TEM was very very small. Also, due to the small amount martensite it was not possible to get any peaks of martensite from XRD. Although work done in literature [35, 51] have found out the induced martensite following same test condition, but due to limitation of lab facility and equipment's those work were not carried out for this project. The hardness value of tensile failed specimen at room temperature was considerably high as compared to deformed specimen and this may be attributed to martensite formation in the material.

- Observation of microstructure for tensile failed specimen at depressed temperature (i.e. -80°C and -40°C) was examined in this work. Optical microscope image analysis reveals that the austenite grain structure is not stable. According to the Graph 2.19, maximum induced martensite is formed at the depressed temperature. Ferritescope also shows a reading of approx. 20% for martensite content for tensile failed specimen at -80°C. It was not possible to see any diffraction pattern of martensite through TEM, but hardness value (See Graph 4.22) was increased to almost double as compared to undeformed material. This result of increased hardness value may support the formation of martensite.

6 Conclusion

Below points will conclude the findings of the work:

- It can be concluded that there was no induced martensite formation at low (approx.2%) and high (approx.10%) strain amplitude cyclic deformation of material, only increase in mechanical twin's may be seen.
- In tensile failed specimen at room temperature using low strain rate, strain induced martensite can be observed and the result was supported by optical microscope image analysis and hardness measurement. There was limitation of equipment's available to carry out the work otherwise the result would have been verified more precisely using other techniques such as NDT and measuring magnetic properties.
- For tensile failed specimen at depressed temperature maximum amount of induced martensite is observed and this result was supported by ferritescope readings, optical microscope image analysis and hardness measurement. This result is attributed to the temperature dependency of stacking-fault energy (SFE) which decreases as the temperature is lowered.
- With increase in strain rate value the tendency to form induced martensite is reduced due to adiabatic heating which increases the stacking-fault energy (SFE) and decreases the chemical driving force of the martensite transformation.
- The maximum hardness of material was seen in the tensile failed specimen at depressed temperature (i.e. -80°C and then 40°C) followed by tensile failed specimen at room temperature with low strain rate and than followed by cyclically deformed specimen (i.e. without failure).

7 Further work

- Several NDT methods can be used to estimate magnetic properties such as coercivity, remanance and saturation magnetization which can help calculate the amount of induced martensite more precisely.
- Extensive EBSD, XRD and TEM examination is proposed as the subject of further studies.

References

[1] S. Dutta. Different types and new applications of stainless steel. 62, 10 2018.

[2] Seven oceans pipelaying vessel. `https://bit.ly/38hGRUK`.

[3] W. Qin J.A. Szpunar K.S. Guan M. Song, N.P. Gurao. Deciphering deviation in mechanical properties of differently processed aisi 316l austenitic stainless steel using the small punch test. *Materials Science and Engineering: A*, 628(1), 2015.

[4] Michael F McGuire. *Stainless steels for design engineers*. Asm International, 2008.

[5] Baldev Raj U.kamachi Mudali. *High nitrogen steels and stainless steels: manufacturing, properties and applications*. Asm International, 2004.

[6] Joseph Ki Lai Leuk, C. Shek, and K. H. Lo. Stainless steels: An introduction and their recent developments. 2012.

[7] Anton L Schaeffler. Constitution diagram for stainless steel weld metal. *Metal progress*, 56(11):680, 1949.

[8] Harry Bhadeshia and Robert Honeycombe. *Steels: microstructure and properties*. Butterworth-Heinemann, 2017.

[9] Erich Folkhard. *Welding metallurgy of stainless steels*. Springer Science & Business Media, 2012.

[10] Louis Colombier and Joseph Hochmann. *Stainless and heat resisting steels*. Edward Arnold (Publishers) Limited, 1967.

[11] Patrick Marshall. *Austenitic stainless steels: microstructure and mechanical properties*. Springer Science & Business Media, 1984.

[12] Carrouge D. Phase transformations in welded supermartensitic stainless steels. *Doctoral thesis, University of Cambridge*, 2002.

[13] O. Kubaschewski. *Iron-Binary phase diagrams*. Springer-Verlag Berlin Heidelberg, 1982.

[14] JC Humbert. The solubility of nitrogen in liquid fe-cr-ni alloys. *Trans. AIME*, 218:1076–1088, 1960.

[15] Ju-Tung Lee Hon-Yee Liou Wen-Fung Wang Wen-Ta Tsai, Ying-Nan Wen. Effect of silicon addition on the microstructure and corrosion behavior of sintered stainless steel. *Surface and Coatings Technology*, 34, 1988.

[16] Rodney P Elliott. Constitution of binary alloys. *1965, 877 P. MCGRAW-HILL BOOK BO., 330 W. 42 ND ST NEW YORK, N. Y. 10036*, 1965.

[17] Max Hansen and Kurt Anderko. *Constitution of binary alloys*. McGraw-Hill, 1958.

[18] Jerzy Kaleta, Przemysław Wiewiórski, and Wojciech Wiśniewski. Investigation of martensitic transformation induced by cyclic plastic deformation in austenitic steels. *Austenitic Stainless Steels: New Aspects*, page 29, 2017.

[19] W.S.Owen G.B.Olson. *Martensite: a tribute to Morris Cohen*. Asm International, 1992.

[20] G.Beranger P.Lacombe, B.Baroux. *Stainless steels*. 1993.

[21] Roberts. Transactions the metallurgical society of aime. *vol*, 224:638, 1962.

[22] Hakan Holmberg, Jan-Olof Nilsson, and Ping Liu. Development of low cost non-magnetic stainless spring steels. *ISIJ International*, 30(8):594–599, 1990.

[23] Amar K De, John G Speer, David K Matlock, David C Murdock, Martin C Mataya, and Robert J Comstock. Deformation-induced phase transformation and strain hardening in type 304 austenitic stainless steel. *Metallurgical and Materials Transactions A*, 37(6):1875–1886, 2006.

[24] Chia-Chang Wu, Shing-Hoa Wang, Chih-Yuan Chen, Jer-Ren Yang, Po-Kay Chiu, and Jason Fang. Inverse effect of strain rate on mechanical behavior and phase transformation of superaustenitic stainless steel. *Scripta materialia*, 56(8):717–720, 2007.

[25] Jaeyeong Park, Min Cheol Jo, Hyeok Jae Jeong, Seok Su Sohn, Jai-Hyun Kwak, Hyoung Seop Kim, and Sunghak Lee. Interpretation of dynamic tensile behavior by austenite stability in ferrite-austenite duplex lightweight steels. *Scientific reports*, 7(1):1–14, 2017.

[26] Pat L Mangonon and Gareth Thomas. The martensite phases in 304 stainless steel. *Metallurgical transactions*, 1(6):1577–1586, 1970.

[27] Taira Suzuki, H Kojima, K Suzuki, T Hashimoto, and M Ichihara. An experimental study of the martensite nucleation and growth in 18/8 stainless steel. *Acta Metallurgica*, 25(10):1151–1162, 1977.

[28] JW Brooks, MH Loretto, and RE Smallman. Direct observations of martensite nuclei in stainless steel. *Acta Metallurgica*, 27(12):1839–1847, 1979.

[29] Michel Humbert, Bertrand Petit, Bernard Bolle, and Nathalie Gey. Analysis of the γ– –α variant selection induced by 10% plastic deformation in 304 stainless steel at- 60 c. *Materials Science and Engineering: A*, 454:508–517, 2007.

[30] Kazunori Sato, Michiyuki Ichinose, Yoshihiko Hirotsu, and Yasunobu Inoue. Effects of deformation induced phase transformation and twinning on the mechanical properties of austenitic fe–mn–al alloys. *ISIJ international*, 29(10):868–877, 1989.

[31] Peter Hedström. *Deformation and martensitic phase transformation in stainless steels*. PhD thesis, Luleå tekniska universitet, 2007.

[32] GB Olson and Morris Cohen. A mechanism for the strain-induced nucleation of martensitic transformations. *Journal of the Less Common Metals*, 28(1):107–118, 1972.

[33] JW Brooks, MH Loretto, and RE Smallman. Direct observations of martensite nuclei in stainless steel. *Acta Metallurgica*, 27(12):1839–1847, 1979.

[34] KP Staudhammer, LE Murr, and SS Hecker. Nucleation and evolution of strain-induced martensitic (bcc) embryos and substructure in stainless steel: a transmission electron microscope study. *Acta Metallurgica*, 31(2):267–274, 1983.

[35] Juho Talonen et al. Effect of strain-induced α'-martensite transformation on mechanical properties of metastable austenitic stainless steels. 2007.

[36] JR Patel and Morris Cohen. Criterion for the action of applied stress in the martensitic transformation. *Acta metallurgica*, 1(5):531–538, 1953.

[37] JA Venables. The martensite transformation in stainless steel. *The Philosophical Magazine: A Journal of Theoretical Experimental and Applied Physics*, 7(73):35–44, 1962.

[38] Pat L Mangonon and Gareth Thomas. The martensite phases in 304 stainless steel. *Metallurgical transactions*, 1(6):1577–1586, 1970.

[39] R LAGNEBORGJ. The martensite transformation in 18 *Acta Metallurgica*, 12:823–843, 07 1964.

[40] D Goodchild, WT Roberts, and DV Wilson. Plastic deformation and phase transformation in textured austenitic stainless steel. *Acta Metallurgica*, 18(11):1137–1145, 1970.

[41] JF Breedis and Larry Kaufman. The formation of hcp and bcc phases in austenitic iron alloys. *Metallurgical Transactions*, 2(9):2359–2371, 1971.

[42] JP Bressanelli and A Moskowitz. Effects of strain rate, temperature, and composition on tensile properties of metastable austenitic stainless steels. *ASM Trans Quart*, 59(2):223–239, 1966.

[43] Tryggve Angel. Formation of martensite in austenitic stainless steels. *J. Iron Steel Inst.*, 177:165–174, 1954.

[44] Louis Colombier and Joseph Hochmann. Aciers inoxydables, aciers refractaires. 1965.

[45] FB Pickering. Physical metallurgical development of stainless steels. In *Proc. Conf. on Stainless Steels 84, Goteborg, 3-4 Sept.*, 1984.

[46] DR Harries. Physical metallurgy of iron–chromium–nickel austenitic steels. In *Mechanical Behaviour and Nuclear Applications of Stainless Steel at Elevated Temperatures[Conf. Preprints], Varese, Italy*, 1981.

[47] MW Bowkett. *Martensite formation and reversion in austenitic stainless steels*. PhD thesis, University of Wales. Cardiff, 1980.

[48] JF Breedis. Martensite reversion in stainless steel(martensite transformation in stainless steel after reversion with quenching). *AIME, TRANSACTIONS*, 236:218, 1966.

[49] H Smith and DRF West. Annealing of austenite formed by reversion from martensite in an fe–16cr–12ni alloy. *Metals Technology*, 1(1):37–40, 1974.

[50] J Talonen, P Aspegren, and H Hänninen. Comparison of different methods for measuring strain induced α-martensite content in austenitic steels. *Materials Science and Technology*, 2004.

[51] Chungseok Kim. Nondestructive evaluation of strain-induced phase transformation and damage accumulation in austenitic stainless steel subjected to cyclic loading. *Metals*, 8(1):14, 2018.

[52] Chung-Seok Kim and Kyung-Young Jhang. Fatigue-induced micro-damage characterization of austenitic stainless steel 316 using innovative nonlinear acoustics. *Chinese Physics Letters*, 29:060702, 2012.

[53] Wenkai Li, Haitao Cui, Weidong Wen, Xuming Su, and CC Engler-Pinto Jr. In situ nonlinear ultrasonic for very high cycle fatigue damage characterization of a cast aluminum alloy. *Materials Science and Engineering: A*, 645:248–254, 2015.

[54] S Palit Sagar, Avijit Kumar Metya, M Ghosh, and S Sivaprasad. Effect of microstructure on non-linear behavior of ultrasound during low cycle fatigue of pearlitic steels. *Materials Science and Engineering: A*, 528(6):2895–2898, 2011.

[55] Simon V Walker, Jin-Yeon Kim, Jianmin Qu, and Laurence J Jacobs. Fatigue damage evaluation in a36 steel using nonlinear rayleigh surface waves. *Ndt & E International*, 48:10–15, 2012.

[56] Melody A Drewry and Paul D Wilcox. One-dimensional time-domain finite-element modelling of nonlinear wave propagation for non-destructive evaluation. *NDT & E International*, 61:45–52, 2014.

[57] Gian Piero Malfense Fierro, Dmitri Ginzburg, Francesco Ciampa, Michele Meo, et al. Nonlinear ultrasonic stimulated thermography for damage assessment in isotropic fatigued structures. *Journal of Sound and Vibration*, 404:102–115, 2017.

[58] Yo Tomota. Crystallographic characterization of steel microstructure using neutron diffraction. *Science and technology of advanced materials*, 20(1):1189–1206, 2019.

[59] J Man, K Obrtlík, M Petrenec, P Beran, M Smaga, A Weidner, J Dluhoš, T Kruml, H Biermann, D Eifler, et al. Stability of austenitic 316l steel against martensite formation during cyclic straining. *Procedia Engineering*, 10:1279–1284, 2011.

[60] Douglas B Murphy. *Fundamentals of light microscopy and electronic imaging*. John Wiley & Sons, 2002.

[61] Peter J Goodhew and John Humphreys. *Electron microscopy and analysis*. CRC Press, 2000.

[62] BJ Inkson. Scanning electron microscopy (sem) and transmission electron microscopy (tem) for materials characterization. pages 17–43, 2016.

[63] Kay Geels, Daniel B Fowler, Wolf-Ulrich Kopp, and Michael R {udiaer} ckert. *Metallographic and materialographic specimen preparation, light microscopy, image analysis, and hardness testing*, volume 46. ASTM international West Conshohocken, 2007.

[64] Jan Ketil Solberg and Vidar Hansen. "introduction to transmission electron microscopy", compendium produced at university of stavanger, norway. 2018.

[65] My scope. Introduction - aims and learning outcomes. `https://myscope.training/legacy/tem/introduction/`.

[66] Bertram Eugene Warren. *X-ray Diffraction*. Courier Corporation, 1990.

[67] Scott A Speakman. Introduction to x-ray powder diffraction data analysis. `http://prism.mit.edu/xray/introduction%20to%20xrpd%20data%20analysis.pdf`.

[68] William D Callister Jr and David G Rethwisch. *Callister's materials science and engineering*. John Wiley & Sons, 2020.

[69] J Malzbender. Comment on hardness definitions. *Journal of the European Ceramic Society*, 23(9):1355–1359, 2003.

[70] Vickers hardness test. `https://www.gordonengland.co.uk/hardness/vickers.htm`.

[71] Breno Mendes Rabelo Avila, André Itman Filho, João Alberto Fioresi Altoé, Jaqueline Polezi Mazini, and Pedro Gabriel Bonella de Oliveira. Cold deformation and hardness on superaustenitic stainless steel: Evaluation methods. *Materials Research*, 23(4), 2020.

A Appendix

Below figure shows the ferritescope reading of tensile failed specimen at -80°C.

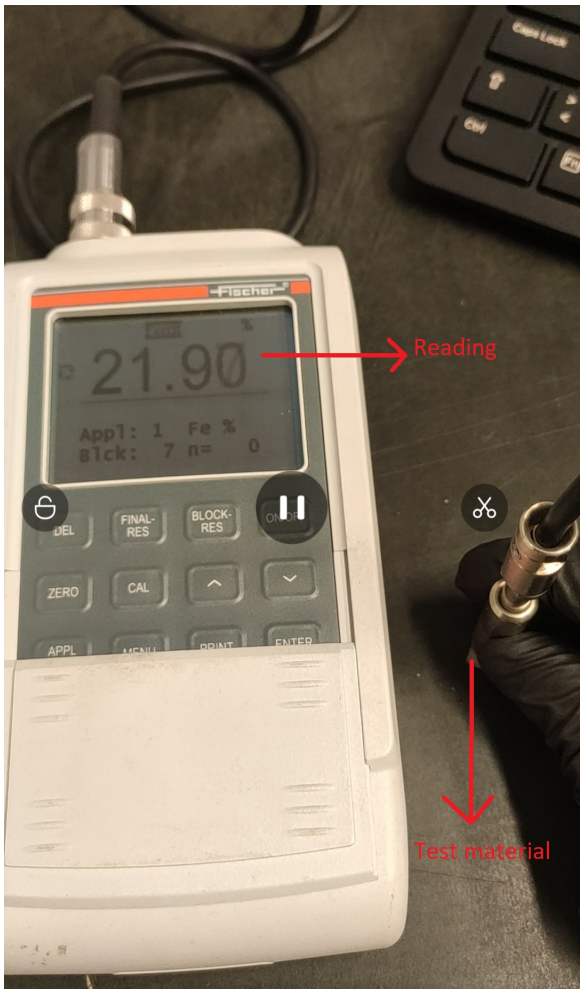

Figure A.1: *Ferrite scope reading for tensile failed specimen at -80°C*